Interfacial water dynamics

Ines Margret Hauner

To cite this version:

Ines Margret Hauner. Interfacial water dynamics. Chemical Physics [physics.chem-ph]. Université Pierre et Marie Curie - Paris VI; Universiteit van Amsterdam. Faculteit der Natuurwetenschappen, Wikunde en Informatica, 2017. English. NNT : 2017PA066145 . tel-01635390

HAL Id: tel-01635390
https://theses.hal.science/tel-01635390

Submitted on 15 Nov 2017

Interfacial water dynamics

Ines M. Hauner

Printed by Gildeprint
Cover designed by Ines M. Hauner

The author can be reached at: ines.hauner@googlemail.com

Interfacial water dynamics

ACADEMISCH PROEFSCHRIFT

ter verkrijging van de graad van doctor
aan de Universiteit van Amsterdam
op gezag van de Rector Magnificus
prof. dr. ir. K.I.J. Maex
ten overstaan van een door het College voor Promoties ingestelde commissie,
in het openbaar te verdedigen in de Agnietenkapel
op woensdag 7 juni 2017, te 14 uur

door

Ines Margret Hauner

geboren te Ulm, Duitsland

Promotiecommissie

Promotores:

Prof. dr. D. Bonn	Universiteit van Amsterdam
Prof. dr. M. Tatoulian	Université Pierre et Marie Curie/ENSCP

Overige leden:

dr. G. Smits	Universiteit van Amsterdam
Prof. dr. S. Woutersen	Universiteit van Amsterdam
dr. M.-C. Jullien	ESPCI Paris
Prof. dr. H. Kellay	Université de Bordeaux
Prof. dr. E.H.G. Backus	Universiteit van Amsterdam

Faculteit der Natuurwetenschappen, Wiskunde en Informatica

Dit proefschrift is tot stand gekomen in het kader van het wetenschappelijke programma van de Franse Nationale Onderzoek Agentschap (ANR) met als doel het behalen van een gezamenlijk doctoraat. Het proefschrift is voorbereid aan de Faculteit der Natuurwetenschappen, Wiskunde en Informatica van de Universiteit van Amsterdam en op de École Nationale Supérieure de Chimie de Paris (ENSCP) gekoppeld aan de Université Pierre et Marie Curie.

This thesis has been written within the framework of the scientific program of the French National Research Agency (ANR), with the purpose of obtaining a joint doctorate degree. The thesis was prepared at the Faculty of Science at the University of Amsterdam and at the École Nationale Supérieure de Chimie de Paris (ENSCP) attached to the University Pierre et Marie Curie.

Cette thèse a été réalisée en cotutelle avec la faculté des sciences de l'université d'Amsterdam et l'École Nationale Supérieure de Chimie de Paris (ENSCP) rattachée à l'université Pierre et Marie Curie. Elle s'inscrit dans le cadre du programme scientifique de l'agence nationale de la recherche (ANR).

“The oldest, shortest words - ’yes’ and ’no’ - are those which require the most thought.”

Pythagoras

Summary

Water - despite its ubiquity and importance - is yet incompletely understood. Its behaviour remains the subject of vivid scientific debate and new theoretical frameworks keep emerging as well as new experimental and numerical methodologies. Interfaces are likewise omnipresent in both science and technology and associated interfacial dynamics involving a water phase are therefore very interesting to study, with ample potential applications. This thesis focusses on three of the most important interfacial water phenomena: proton diffusion in a complex environment, drop formation and relative oil-water displacement within a porous material.

We start our experimental investigations by studying a liquid-liquid 'quasi-interface' made up of two complex, cell-like aqueous solutions with different pH values (chapter 3). Such 'interfaces' are frequently encountered within the cytoplasm where - according to recent evidence - subdomains with (fairly) different pH values may coexist even in the absence of a physical barrier such as a lipid membrane. We use a combined approach of microfluidics and ultrafast femtosecond IR spectroscopy to probe both the proton diffusion behaviour and the water reorientation dynamics. Our experiments reveal that the proton diffusion coefficient in these cell mimicking solutions is significantly reduced, while the water dynamics remain almost unchanged. These results strongly suggest that in such complex solutions a buffer mediated proton diffusion mechanism dominates over the classical 'Grotthus' diffusion encountered in bulk water.

The second part of this thesis focuses on droplet formation at the water-air interface: inviscid droplet breakup is a universal, extremely rich phenomenon and its theoretical description constitutes one of the simplest instances of a naturally occurring finite-time singularity. In Chapter 4 we follow the rupture dynamics of water and inviscid fluids by the help of an ultrarapid camera setup. The observed pinch-off behaviour of water and aqueous solutions substantially deviates from other simple liquids, which is reflected by the unexpectedly high

derived surface tension values of newly created water-air interfaces. While the origin of this striking result remains incompletely understood, the existence of such a dynamic surface tension has crucial consequences for a wide variety of processes that occur at very short submillisecond time scales. In Chapter 5 we further assess the validity of a promising electrical method that presumably allows to experimentally approach the instant of drop breakup on a nanosecond time scale. We follow the rupture dynamics of highly conductive liquids - mercury and gallium - and compare the results with simulations of the mercury pinch-off. Our findings demonstrate that even the application of small voltages is detrimental to the pinch-off dynamics due to undesirable side effects that obscure the process of interest.

In the last part (chapter 6) we study a three phase system consisting of water and oil in different 'rough' microdevices in order to address a problem that is particularly encountered in enhanced oil recovery: oil displacement behaviour as a function of surface topology. We therefore perform water flooding experiments in a microfluidic fluorescent microscopy setup and, indeed, find a direct relationship between the size of the channel roughness and the oil recovery rate. Based on our results we are able to formulate a generic scaling law for the amount of the retained oil that accounts for the joint effects of roughness, viscosity, surface tension and fluid velocity. We likewise provide a qualitative account on characteristic displacement patterns observable for oils with different viscosities and different microchannel surface topologies.

.

Résumé

L'eau est une ressource abondante sur terre et omniprésente dans notre vie quotidienne. Elle est essentielle, voire indispensable, pour tous les organismes vivants, mais aussi primordiale dans un grand nombre d'applications scientifiques et technologiques. Pour toutes ces raisons, l'eau a fait l'objet de nombreuses études antérieures, mais demeure sous bien des aspects que partiellement comprise. Un exemple pertinent suscitant actuellement de nombreux débats au sein de la communauté scientifique, concerne les propriétés interfaciales de l'eau intervenant dans de multiples processus physiques.

Cette thèse porte sur l'étude de trois phénomènes interfaciaux reliés à l'eau : (i) la diffusion de protons dans un environnement complexe, (ii) la formation de gouttes et (iii) le déplacement d'huile sous l'effet du déplacement d'une phase aqueuse dans un circuit microfluidique poreux.

Dans un premier temps, nous étudions expérimentalement une «quasi - interface», constituée de deux solutions complexes aqueuses de différents pH, telles qu'on les trouve dans les milieux cellulaires. En effet, des études récentes suggèrent que des sous-domaines de différents pH peuvent coexister dans le cytoplasme en l'absence même d'une barrière physique telle qu'une membrane lipidique. On se sert d'une approche combinant un circuit microfluidique et une technique de spectroscopie IR femtoseconde, pour examiner la diffusion des protons et les dynamiques de réorientation des molécules d'eau. Nos expériences révèlent que le coefficient de diffusion des protons dans ces solutions modèles, analogues au cytoplasme, est considérablement diminué alors que la dynamique des molécules d'eau est, elle, à peine altérée. Ces résultats suggèrent que le transport des protons serait médié par des molécules tampons, contrairement à la description classique de Grotthus faisant intervenir un processus de transport volumique.

La deuxième partie de cette thèse porte sur la rupture de gouttes et focalise alors sur l'interface liquide/air. La rupture de gouttes de fluides non-visqueux est un phénomène extrêmement riche et sa description théorique constitue un des cas les plus simples des singularités à temps fini. Le chapitre 4 se focalise sur l'étude de la dynamique de rupture d'une goutte d'eau et d'autres fluides «simples», non-visqueux, à l'aide d'une caméra ultra-rapide. On montre qu'aux temps courts (<ms) le comportement de l'eau dévie de celui des fluides «simples», révélant une tension interfaciale dynamique pour l'eau bien supérieure à celle connue à l'équilibre ($72 \mathrm{mNm}^{-1}$). L'existence d'une tension de surface dynamique a des conséquences cruciales pour un grand nombre de procédés ayant lieu à l'échelle de la milliseconde. Dans le chapitre 5, on s'intéresse à la dynamique de rupture de métaux via des mesures électriques permettant de se rapprocher temporellement (et spatialement) au plus près de la rupture (ns). Les dynamiques de rupture de liquides hautement conducteurs – mercure et gallium – sont étudiées et les résultats obtenus sont comparés aux simulations. Nos résultats démontrent que la mesure impacte la dynamique : même l'application de tensions très faibles nuit aux mesures de dynamiques de rupture, dû à des effets secondaires indésirables, entachant la mesure.

Enfin, dans la dernière partie (chapitre 6), on revisite un problème classique : le déplacement d'huile avec de l'eau, rencontré dans les techniques de récupération assistée du pétrole (RAP). Plus spécifiquement, on s'intéresse à l'effet de la topologie de surface de la roche poreuse sur le piégeage de gouttes d'huile. Cette étude est effectuée en faisant varier la rugosité de surface de canaux microfluidiques et en suivant l'écoulement par microscopie de fluorescence. On réalise le même type d'expériences dans des micro-réseaux poreux dont la rugosité est contrôlée et préparée à partir de différents agencements de billes de verre. Nos expériences montrent la contribution importante de la rugosité des canaux dans le déplacement et le piégeage de l'huile en plus de celles de la viscosité et du nombre capillaire. On dégage alors une loi d'échelle générale liant les effets de la rugosité au déplacement du fluide au sein du canal.

.

Samenvatting

Water is belangrijk en komt overal voor, maar het gedrag van water is nog steeds onvolledig begrepen. De fysische eigenschappen van water blijven het onderwerp van levendige wetenschappelijke debatten; nieuwe theoretische kaders en nieuwe experimentele en numerieke technieken worden continu ontwikkeld. Grensvlakken waarin water een rol speelt komen eveneens veel voor in verschillende toepassingen, en zijn derhalve interessant om te bestuderen. Dit proefschrift gaat over drie van de meest belangrijke fenomenen waarin het oppervlak van water een belangrijke rol speelt: Protonendiffusie in een complexe omgeving, druppelformatie en olie verplaatsing binnen een poreus materiaal door middel van een water stroming.

Wij starten onze experimenten met het bestuderen van een vloeistof-vloeistof 'quasi-grensvlak' bestaande uit twee complexe (celachtige) waterige oplossingen met verschillende pH-waarden (hoofdstuk 3). Dergelijke grensvlakken worden vaak binnen het cytoplasma aangetroffen en recente onderzoeken sugge-reren dat sub-domeinen met significant verschillende pH-waarden naast elkaar kunnen bestaan, zelfs bij afwezigheid van een barrière, zoals een celmembraan. Wij gebruiken een gecombineerde benadering van microfluïdica en ultrasnelle femtoseconde IR spectroscopie om zowel het protonen diffusiegedrag als de water heroriëntatie dynamica te onderzoeken. Uit onze experimenten blijkt dat de protonen diffusie coëfficiënt in deze cel-achtige oplossingen significant is gereduceerd terwijl de waterdynamica bijna onveranderd blijft. Deze resultaten laten zien dat in zulke complexe oplossingen buffer gemedieerde protonen diffusie prevaleert boven de klassieke 'Grotthus' diffusie, een mechanisme dat in bulk water domineert.

Het tweede onderdeel van dit proefschrift is gericht op druppel formatie, en dus op het grensvlak tussen water en lucht. Het vormen van druppels van niet-viskeuze vloeistoffen is een universeel fenomeen waarvan de theo-retische beschrijving een van de meest eenvoudige natuurlijk voorkomende eindige-tijd singulariteiten is. In hoofdstuk 4 bestuderen wij het druppelen van water en andere niet-viskeuze vloeistoffen met behulp van een hogesnelheidscamera. De oppervlaktespanning van water en waterhoudende oplossingen, afgeleid uit theoretische modellen, blijkt onverwacht hoog te zijn in vergelijking tot eenvoudige vloeistoffen. De fysieke oorsprong van dit interessante resultaat is niet bekend, maar het bestaan van een dynamische oppervlaktespanning heeft cruciale gevolgen voor een breed assortiment van processen die op tijdschalen korter dan een milliseconde plaatsvinden. In hoofdstuk 5 beoordelen we de validiteit van een veelbelovende techniek die het bestuderen van druppelformatie op nanoseconde tijdschaal en nanometer lengteschaal mogelijk maakt. Wij observeren de druppeldynamiek van sterk geleidende vloeistoffen – kwik en gallium – en vergelijken de resultaten met kwik druppelsimulaties. Onze bevindingen tonen aan dat zelfs kleine elektrische spanningen de druppelvorming beïnvloeden en dat daardoor ongewenste bijverschijnselen de experimenten domineren.

In het laatste gedeelte bestuderen wij een drie-fasen systeem bestaande uit water en olie in verschillende 'ruwe' microkanalen om een voor verbeterde oliewinning ('Enhanced oil recovery' of EOR) belangrijk vraagstuk te beantwoorden: Het verplaatsingsgedrag van olie als functie van oppervlaktetopologie van het poreuze medium waarin de olie zich bevindt. Net als in EOR pompen wij water door een met olie gevuld kanaal, en kijken hoeveel olie er aan de uitgang 'gewonnen' kan worden. Met behulp van een microfluïdische microscopie opstelling constateren we dat er een direct verband bestaat tussen de oppervlakteruwheid en de efficiëntie van oliewinning. Gebaseerd op onze resultaten zijn wij in staat om een algemene schalingswet voor de oliewinning te formuleren die de gezamenlijke effecten van ruwheid, viscositeit, oppervlaktespanning en stromingssnelheid incorporeert. Daarnaast vinden wij kwalitatieve verbanden tussen de karakteristieke patronen die ontstaan en de verschillende viscositeiten en oppervlakte topologieën.

.

Contents

Dedicated to my family.

Chapter 1

Introduction

1.1 Preface: water

Das bekannte ist überhaupt darum, weil es bekannt ist, nicht erkannt. (engl.: What is familiar is not understood precisely because it is familiar.)
Hegel, German philosopher (1770-1831)

Nature and the way it organizes things might sometimes appear simple at a first superficial glance, however, a closer look often reveals an unanticipated degree of complexity. Water is one of these examples: everyone knows it, but nobody really understands it and the further our investigations go, the more this exact awareness becomes apparent.

Water is ubiquitous: composed of just oxygen and hydrogen, this three-atomic molecule makes up two thirds of our planet and likewise, our own bodies are composed of an average of 60 % water. And therefore water is indispensable: a myriad of important chemical reactions only work in aqueous solutions and the functioning of most biological organisms crucially depends on the presence of a suitable aqueous environment.

How can it thus be that we still do not really know what we are surrounded by, what we consist of and what we depend on? As a matter of fact, the water molecule possesses an incredibly rich chemistry due to numerous yet incompletely understood anomalous properties [1, 2, 3, 4, 5]: water has a very particular phase diagram with a liquid state that is more dense than the solid state and unexpectedly high melting and boiling points (with respect to its constituent atoms). The latent heat associated with these phase transitions is striking, as is the particularly high heat capacity. The surface tension of water is extremely

K. HOKUSAI (1760–1849)/BRIDGEMAN

FIGURE 1.1: **Water dynamics as central theme in visual arts.** Katsushika Hokusai's 'Amida Waterfall on the Kisokaido Road' allegorizes a rousing, personified version of a waterfall and thereby exemplifies the fascination that water dynamics have always held for men throughout all disciplines.

strong while its viscosity is fairly low given the presence of strong intermolecular hydrogen bonds. Due to an equally extraordinary high dielectric constant, water constitutes an almost universal solvent which, in turn, contributes to its ample direct and indirect chemical reactivity with other species. Water is therefore pivotal and indispensable for the functioning of nature as we perceive it day to day. As a matter of fact, our world would probably look quite differently if water behaved just like a 'normal' molecule as expected from its chemical configuration.

1.1.1 Hydrogen bonding, collectivity and provocative thoughts

The anomalous behaviour of water is primarily attributed to its ability to form hydrogen bonds with surrounding molecules - both as a donor and as an acceptor molecule - giving rise to a three-dimensional network with presumably (see below) tetrahedral subunits. What is more, water is a highly collective liquid: a local change in the hydrogen bond network does not only affect the structure and dynamics of the nearest neighbouring molecule(s). Rather, any change can be expected to propagate through the hydrogen bond network and thereby induce long-range changes in the local energy structure through reorientation of other water molecules and the associated breakup/formation of new hydrogen bonds. The ability of water to accommodate such multiple-body interactions is unique and elucidating the detailed underlying mechanisms crucial to a complete comprehension of the outstanding behaviour of water.

While it is a general consensus that the anomalous behaviour of water originates to a large extent from the embedment of individual H_2O molecules into a hydrogen bonded network, it is still not sufficiently understood how exactly this translates into the observed bulk-scale properties [5]. Rather, with the advent of new experimental techniques new mysteries have emerged during the past decades, as a consequence of which the standard picture of water as presented in 1975 [6] has been challenged in multiple ways. In this sense a literal plethora of thought provoking hypotheses addressing some of the most essential, fundamental bearings have nurtured vehement discussions [7, 8, 9].

A very prominent example are the highly agitative conjectures of Lars Petterson and co-workers, that developed a so-called 'string theory of water' [4, 10]. According to them, water molecules in the liquid state form hydrogen bonds with merely two neighbouring molecules which gives rise to chains and rings instead of the conventional tetrahedral structure. The consecutive ’two-state’ model presented a few years later took this further by proposing that liquid water consists of a ’string’ structured bulk interspersed with tiny ’clusters’ conform to tetrahedral coordination. Albeit highly controversial and despite heavy criticism, Petterson’s ideas prevail subject of intensive debate, the more so as, if only partially valid, they would entail a cardinal change of our picture on how dissolved entities behave.

On this note, water truly exemplifies a general caveat that latently threatens any scientific field: seemingly (well) established scientific knowledge is not a sacrosanct, but merely a momentary snapshot of the most plausible explanation to a given phenomenon at a given point in time.

1.1.2 Surfaces and interfaces

In the present thesis our main attention will be focussed on phenomena that occur at or in close proximity to interfaces. Interfaces in general are interesting to study as they define the boundaries between different compartments that only exchange matter and energy under particular conditions. A universal property of any interface are the energy costs associated with its expansion which is reflected as a surface tension that counteracts any other physical or chemical forces fostering further enlargement.

Water surfaces and interfaces deserve special attention as they are omnipresent in both nature (e.g. cellular membranes, oceans, rain drops) and technology (e.g. heterogeneous catalysis, electrochemistry). The surface tension of water is known to be extremely high indicating a high energy cost for the creation of new interfacial area, which is generally ascribed to the strong intermolecular bonds acting between individual water molecules (Fig. 1.3): in the bulk, a water molecule is isotropically stabilized by the formation of hydrogen bonds with its nearest neighbours. The resulting energetically favoured hydrogen bond network is abruptly interrupted at a water surface bestowing particular properties to the water molecules located in the $\sim$ nm thick surficial region. Interfacial water is known to have a remarkably different phase diagram from bulk water, a ten times lower dielectric constant and a reduced density [11, 12, 13]. The latter is further propelled in the presence of surface active solutes that accumulate in the interfacial region and thereby replace additional water molecules. Interestingly,

FIGURE 1.2: **Water interfaces.** Water interfaces are omnipresent

the adsorption of these species to the water surface can have different impacts on the surface tension of water: while surfactants are well-known to (tremendously) lower the surface tension, a strong surface propensity of halide anions causes the opposite effect [14].

In this context one might wonder if and to what extent interfacial water structurally deviates from bulk water and various surface specific vibrational spectroscopic techniques have therefore been employed in the past to address this precise question [15, 16, 17, 18]. In the case of the rather ’simple’ water-air interface, the difference was found to be actually fairly moderate with a few less strongly hydrogen bonded interfacial water molecules pointing their free OH-groups out into the gas phase [19].

Last but not least, its is worth mentioning that theoretical simulations of water (interfaces) are extremely challenging with large numbers of molecules required and need therefore be interpreted with utmost care. Important parameters such as the high surface tension can as of yet not unambiguously be simulated [20, 21] leaving aside its potential dynamic properties that we will address on detailed experimental grounds in the scope of this thesis.

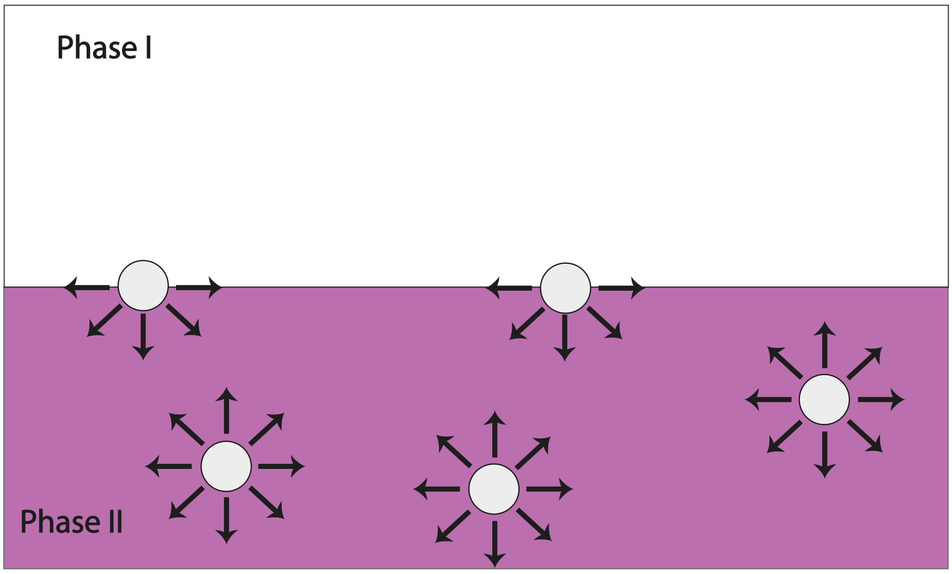

FIGURE 1.3: **Surface tension.** Bulk water molecules are isotropically stabilized by cohesive interactions (hydrogen bonds in Phase II). At an interface this hydrogen bonding network is abruptly terminated giving rise to a very high surface tension.

1.2 Scope of this thesis

The present thesis seeks to provide a significant experimental contribution towards a better understanding of several dynamic processes occurring at the interface of water and another fluid or solid material. We will look at drop formation, proton diffusion and water flooding of an oil reservoir, each of which constitutes a central issue for both fundamental research and industrial process design. .

- **Chapter 2: Theory.** In this chapter the most important theoretical frameworks will be laid out in order to provide a solid foundation for the topics addressed in the subsequent chapters. After a short introduction to the notion of surface tension, a more profound account on droplet breakup dynamics is provided with a focus on inviscid fluids. This is followed by the basic concepts of diffusion and proton displacement in bulk water and eventually closes with a short account on the principles of microfluidics.

- **Chapter 3: Proton mobility in cellular environments.** This chapter looks at a liquid-liquid 'quasi-interface' made up of two complex cell-like aqueous solutions with different pH values. Using a combined approach of microfluidics and ultrafast femtosecond IR spectroscopy the diffusion behaviour of protons across this 'interface' is examined considering the relative influences of solution buffers, macromolecular effects and medium viscosity.

- **Chapter 4: The dynamic surface tension of water.** In this chapter, a more 'classical' water-air interface is studied with respect to its potential dynamic behaviour on a millisecond time scale. By the help of ultrarapid imaging, drop breakup experiments are performed on various inviscid pure liquids, which reveals a remarkable deviation from the known equilibrium value for the surface tension of water. After obtaining similar results for other aqueous liquids, the origins of these findings are discussed with respect to adsorption theory and water dynamics.

- **Chapter 5: Droplet breakup on nanometric length scales.** In this chapter we remain with drop rupture phenomena at the water-air interface, but consider shorter time and length scales than in chapter 4. We follow the rupture dynamics of both mercury and gallium by the help of a previously presented electrical method and discuss the validity of this conductivity-based approach taking into account the results from simulations on the mercury pinch-off.

- **Chapter 6: Roughness and oil recovery.** Motivated by enhanced oil recovery research questions, we finally consider a more complex three phase boundary in order to study the relative displacement behaviour of water and oil in different 'rough' microdevices. The impact of both roughness size and oil viscosity on the oil recovery rate is quantified by the help of fluorescent microscopy and subsequent image analysis. We likewise provide a qualitative account on characteristic displacement patterns observable for oils with different viscosities and different channel geometries.

.

Bibliography

[1] D. Eisenberg and W. Kauzmann. *The Structure and Properties of Water*, volume 166 of *Science*. Oxford University Press, New York, 1969.

[2] O. Mishima and H. E. Stanley. The relationship between liquid, supercooled and glassy water. *Nature*, 396(6709):329–335, 1998.

[3] J. R. Bruijn, T. H. van der Loop, and S. Woutersen. Changing Hydrogen-Bond Structure during an Aqueous Liquid-Liquid Transition Investigated with Time-Resolved and Two-Dimensional Vibrational Spectroscopy. *The Journal of Physical Chemistry Letters*, 7(5):795–799, 2016.

[4] P. Ball. Water: Water-an enduring mystery. *Nature*, 452(7185):291–292, 2008.

[5] J. Russo and H. Tanaka. Understanding water's anomalies with locally favoured structures. *Nature Communications*, 5:3556, 2014.

[6] F. Franks. *Water: A Comprehensive Treatise*, volume 1. Plenum Press, New York, 1975.

[7] P. Poole, F. Sciortino, U. Essmann, and E. Stanley. Phase behaviour of metastable water. *Nature*, 360(6402):324–328, 1992.

[8] C. Austen Angell. Supercooled water: Two phases? *Nat Mater*, 13(7):673–675, 2014.

[9] A. Nilsson and L. G. M. Pettersson. The structural origin of anomalous properties of liquid water. *Nature Communications*, 6:8998, 2015.

[10] P. Wernet, D. Nordlund, U. Bergmann, M. Cavalleri, M. Odelius, H. Ogasawara, L. A Näslund, T. K. Hirsch, L. Ojamäe, P. Glatzel, L. G. M. Pettersson, and A. Nilsson. The Structure of the First Coordination Shell in Liquid Water. *Science*, 304(5673):995, 2004.

[11] P. L. Geissler. Water Interfaces, Solvation, and Spectroscopy. *Annual Review of Physical Chemistry*, 64(1):317–337, 2013.

[12] J. G. Dash, A. W. Rempel, and J. S. Wettlaufer. The physics of premelted ice and its geophysical consequences. *Reviews of Modern Physics*, 78(3):695–741, 2006.

[13] G. E. Brown, V. E. Henrich, W. H. Casey, D. L. Clark, C. Eggleston, A. Felmy, D. W. Goodman, M. Grätzel, G. Maciel, M. I. McCarthy, K. H. Nealson, Dimitri A. Sverjensky, M. F. Toney, and J. M. Zachara. Metal Oxide Surfaces and Their Interactions with Aqueous Solutions and Microbial Organisms. *Chemical Reviews*, 99(1):77–174, 1999.

[14] A. J. Prosser and E. I. Franses. Adsorption and surface tension of ionic surfactants at the air-water interface: review and evaluation of equilibrium models. *Colloids and Surfaces A: Physicochemical and Engineering Aspects*, 178(1-3):1–40, 2001.

[15] Z. Zhang, P. Fenter, L. Cheng, N. C. Sturchio, M. J. Bedzyk, M. Predota, A. Bandura, J. D. Kubicki, S. N. Lvov, P. T. Cummings, A. A. Chialvo, M. K. Ridley, P. Bénézeth, L. Anovitz, D. A. Palmer, M. L. Machesky, and D. J. Wesolowski. Ion Adsorption at the Rutile-Water Interface: Linking Molecular and Macroscopic Properties. *Langmuir*, 20(12):4954–4969, 2004.

[16] E. Mamontov, D. J. Wesolowski, L. Vlcek, P. T. Cummings, J. Rosenqvist, W. Wang, and D. R. Cole. Dynamics of Hydration Water on Rutile Studied by Backscattering Neutron Spectroscopy and Molecular Dynamics Simulation. *The Journal of Physical Chemistry C*, 112(32):12334–12341, 2008.

[17] P. B. Petersen, R. J. Saykally, M. Mucha, and P. Jungwirth. Enhanced Concentration of Polarizable Anions at the Liquid Water Surface: SHG Spectroscopy and MD Simulations of Sodium Thiocyanide. *The Journal of Physical Chemistry B*, 109(21):10915–10921, 2005.

[18] C.-S. Hsieh, M. Okuno, J. Hunger, E. H. G. Backus, Y. Nagata, and M. Bonn. Aqueous Heterogeneity at the Air/Water Interface Revealed by 2D-HD-SFG Spectroscopy. *Angewandte Chemie International Edition*, 53(31):8146–8149, 2014.

[19] M. Bonn, Y. Nagata, and E. H. G. Backus. Molecular Structure and Dynamics of Water at the Water-Air Interface Studied with Surface-Specific Vibrational Spectroscopy. *Angewandte Chemie International Edition*, 54(19):5560–5576, 2015.

[20] M. Tariq, M. G. Freire, B. Saramago, J. A. P. Coutinho, J. N. C. Lopes, and Luis P. N. Rebelo. Surface tension of ionic liquids and ionic liquid solutions. *Chemical Society Reviews*, 41(2):829–868, 2012.

[21] Y. Nagata, T. Ohto, M. Bonn, and T. D. Kühne. Surface tension of ab initio liquid water at the water-air interface. *The Journal of Chemical Physics*, 144(20):204705, 2016.

Chapter 2

Theory

2.1 Surface tension and capillarity

In chapter 1 we have already briefly presented the notion of surface tension as an important, if not *the* key entity when studying interfacial phenomena. From a macroscopic point of view, surface tension, usually denoted by γ (chapter 6) or alternatively σ (chapter 4,5), is defined as half the reversible work W per unit area that is required to separate two planar surfaces or 'half-spaces' that are in contact with each other ($D = D_0$) to infinity ($D = \infty$) (Fig. 2.1) [1]:

$$\gamma = \frac{W}{2} = \frac{A}{24\pi D_0^2} \tag{2.1}$$

D_0 hereby denotes a value on the molecular scale representative of the approximate intermolecular or - atomic distances at equilibrium.[1] A is the Hamaker constant that depends on the nature of the interacting particles as well as the separating medium and is a measure for the van der Waals forces acting between two given surfaces (*or more general:* between two given particles).[2] As already outlined in chapter 1, molecules located in close proximity to a surface only experience half of the stabilizing cohesive interactions compared to molecules in the bulk and therefore forcing a bulk molecule to a surface location entails a loss in cohesive energy of $\sim$ 50 % [2, 3]. From equ. 2.1 it therefore becomes apparent that the creation of a new or the expansion of an existing surface comes with an

---

[1] For many solids and liquids a universal value of D_0 = 0.165 nm has shown to be in good agreement with experimental data. Merely the surface energies of highly polar H-bonding liquids substantially deviate from such predictions [1].

[2] n.b.: in this model only van der Waals interactions are taken into account for simplification.

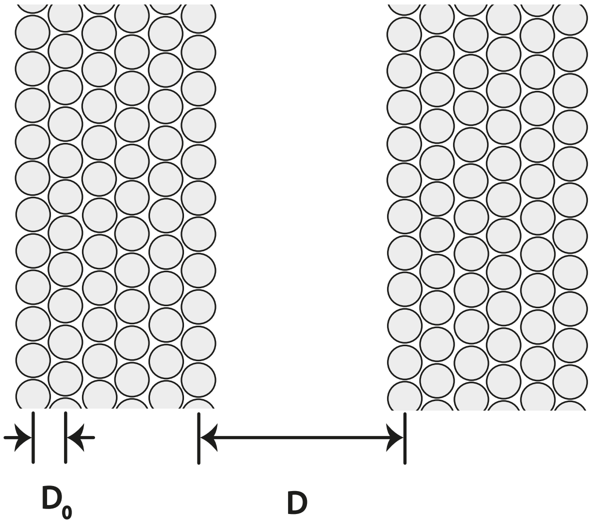

FIGURE 2.1: **Separation of two half-spaces.** The surface tension γ is half the work required to separate two half spaces from $D = D_0$ to infinity ($D = \infty$) [1].

additional energy cost, as a consequence of which nature tends to minimize surface areas.

This results into a force balance at thermodynamic equilibrium, where the relative surface areas of different phases are reflected in the contact angle Θ (Fig. 2.2) [4]:

$$cos\Theta = \frac{\gamma_{sg} - \gamma_{sl}}{\gamma_{lg}} \tag{2.2}$$

where γ denotes the interfacial tension between two phases that can be either solid (s), liquid (l) or gaseous (g). The contact angle is a crucial property for characterizing relative wetting behaviour of different fluids on a solid material and will play an important role in chapter 6.

That being said, a surface location does not necessarily entail an energetically unfavourable state. Certain molecular species (surfactants, halide anions) actually experience an overall stabilization when located close to the surface due to adsorption [5, 6]. Whether or not a given molecule prefers a surface location depends therefore on the relative dominance of cohesive over adhesive forces.

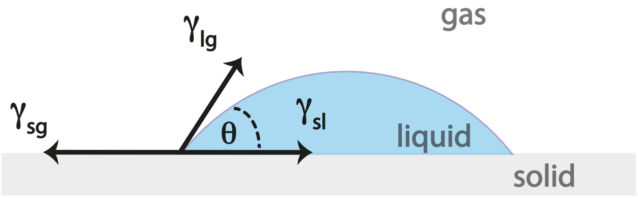

FIGURE 2.2: **Contact angle.** Local force balance at thermodynamic equilibrium.

The resulting surface tension γ of a fluid that contains adsorbing, surface active molecules is given by [7]:

$$\gamma = \gamma_0 + \frac{k_B T}{a^2} \log(1 - \sigma) \tag{2.3}$$

where γ_0 is the surface tension of the bare fluid, T denotes the temperature, k_B is the Boltzmann constant and a^2 corresponds to the surface area that is occupied per adsorbed molecule. $\sigma = N_S/A$ denotes the surface coverage., i.e. the number of molecules N_S adsorbed to a given area A of the surface.

2.2 Drop breakup

Drop breakup is an omnipresent phenomenon that we encounter on a daily basis - be it in the form of splashing water, dropping motor oil or emerging soda bubbles. The prevalence of drop breakup in many applications and the underlying physical richness have motivated considerable research efforts in the past decades. Obtaining a comprehensive theoretical grasp of this phenomenon constitutes, however, a challenging scientific endeavour: suitable theoretical models need to account for the appearance of finite time singularities, i.e. the occurrence of quantities that either diverge or vanish in space or time within a given system. Since the formation of a new drop from a liquid filament is a discontinuous process, a singularity of the associated equations of motions inevitably ensues.

2.2.1 Fundamentals of drop breakup

The flow of an incompressible fluid (i.e. $\vec{\nabla} \cdot \vec{v} = 0$) is governed by the Navier-Stokes equation, that includes a time-dependent domain in the case of drop breakup:

$$\rho \frac{\delta \vec{v}}{\delta t} + \rho(\vec{v} \cdot \vec{\nabla})\vec{v} = -\vec{\nabla} P + \eta \vec{\nabla}^2 \vec{v} + \vec{F} \tag{2.4}$$

where ρ is the density, $\vec{v}$ the vector field of the fluid velocity, P the pressure and η the dynamic fluid viscosity. $\vec{F}$ resumes all present body forces [8].

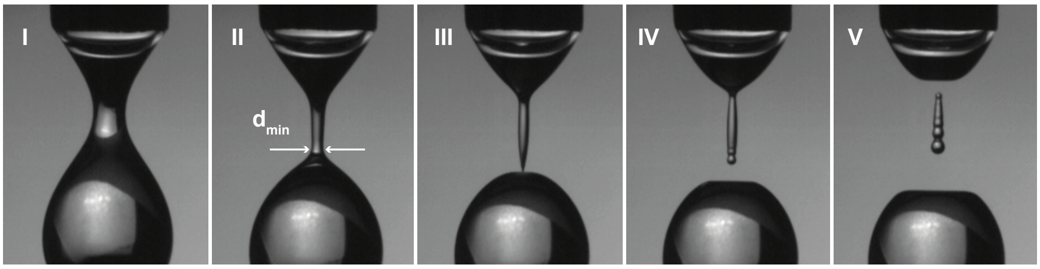

FIGURE 2.3: **Vanishing of physical length scales during drop breakup (ultrarapid images, 50.000 fps).** A drop of an inviscid fluid emanates from an orifice (I) and upon thinning of the fluid filament (II) an asymmetric 'apple-stem' geometry is adopted with an 'overturned' drop profile (III) just before the actual breakup occurs: first the lower end detaches from the falling drop (IV), which gives rise to capillary waves and the formation of one or several satellite drops (V).

The assignment of a Navier-Stokes dynamics inherently entails a large divergence between space and time dimensions. As a consequence, the characteristic length scale of the solution deviates by orders of magnitude from the length scale of the physical system it is supposed to describe. This is illustrated in Fig. 2.3 and 2.4: the finite time singularity that occurs during drop fission is assumed to be characterizable by a single local length scale, the minimum fluid neck diameter d_{min}, that will go to zero as the fluid filament becomes thinner and the instant of breakup is approximated. At the same time, other physical quantities such as the newly created surface A blow up in space illustrating that the whole pinch-off process is driven by capillary forces: formation of a (spherical) drop from a cylindrical fluid filament minimizes potential energy and the rate at which this

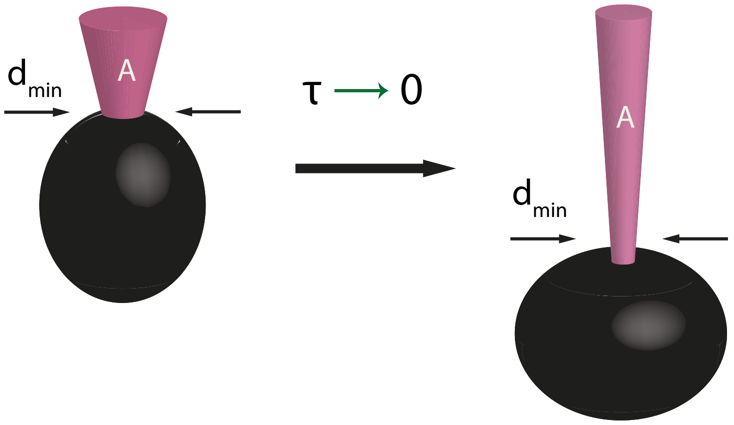

FIGURE 2.4: **Vanishing of physical length scales during drop breakup (schematic sketch).** As the instant of break up ($\tau = 0$) is approached the fluid neck diameter d_{min} goes zero, while the amount of newly created fluid/air surface A goes to infinity.

occurs is primarily dependent on the physical parameters of the fluid, i.e. surface tension, viscosity and density [9].

The fluid motion gives rise to a Laplace pressure Δp that is proportional to the mean curvature κ of the interface (Fig. 2.5) [8]:

$$\Delta p = P_{ext} - P_{int} = \kappa\gamma \tag{2.5}$$

where P_{ext} refers to the pressure in the outer fluid (*here:* air) and P_{int} refers to the pressure inside the thinning fluid filament (cf. Fig. 2.5).

The mean curvature can be derived from the curvatures of the interface, κ_r and κ_z, that arise from the corresponding radii R_r and R_z as illustrated in Fig. 2.5:

$$\kappa = \frac{1}{2}(\kappa_r + \kappa_z) = \frac{1}{2}\left(\frac{1}{R_r} + \frac{1}{R_z}\right) \tag{2.6}$$

The complexity of this non-linear problem can be reduced to a set of one-dimensional equations if one considers only the axial coordinate z of fluid movement [10]. Conservation of mass (volume) is then given by:

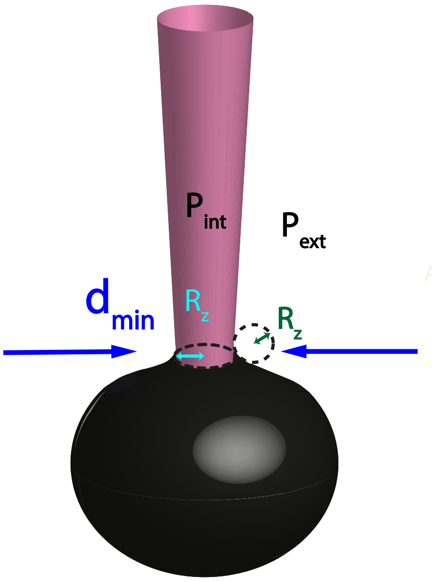

FIGURE 2.5: **Laplace pressure and curvature.** A Laplace pressure proportional to the curvature of the interface emanates from the fluid motion.

$$\partial_t h^2 + \partial_z (v h^2) = 0 \tag{2.7}$$

where $h(z,t) = \frac{1}{2} d(z,t)$ corresponds to the local radius of the fluid neck and $v(z,t)$ to the corresponding fluid velocity. The arising local force balance reads:

$$\underbrace{\partial_t v + v \partial_z v}_{\text{inertia}} = \underbrace{-\frac{\gamma}{\rho} \partial_z \left(\frac{1}{R_1} - \frac{1}{R_2} \right)}_{\text{surface tension}} + \underbrace{3\nu \frac{\partial_z (\partial_z v h^2)}{h^2}}_{\text{viscosity}} + \underbrace{g}_{\text{gravity}} \tag{2.8}$$

where $\nu = \frac{\eta}{\rho}$ corresponds to the kinematic viscosity of the thinning fluid and g is the gravitational constant with a value of $6.67 \times 10^{-11} \mathrm{m}^3 \mathrm{kg}^{-1} \mathrm{s}^{-2}$.

The one-dimensional description given by (2.7) and (2.8) works very well for describing an entire ′real′ breakup event. In immediate proximity to the breakup point, a dimensional analysis perspective usually takes over: since singularities are deprived of a particular length scale, they are typically characterized by power laws that are not affected by the drastic changes in length scales. The associated scaling exponents are found by dimensional analysis [11].

Thereby the local neck diameter d is expressed as a function of the relevant intrinsic and extrinsic parameters [12]:

$$d = f(\Delta z, \tau, \rho, \nu, \gamma, g, d_0) \tag{2.9}$$

where $\Delta z = z - z_0$ denotes the axial coordinate and $\tau = t - t_0$ is the time to pinch-off occurring at (t_0,z_0). d_0 corresponds to the nozzle diameter and thus the diameter of the initial drop.

Nondimensionalization of this yields:

$$d = l_t \bar{f}\left(\frac{\Delta z}{l_t}, \frac{l_\nu}{l_t}, \frac{l_c}{l_t}, \frac{d_0}{l_t}\right) \tag{2.10}$$

where $l_t = \sqrt{\nu \Delta t}$ is a typical length scale that is expected to be relevant close to the instant of breakup and $l_v = (\nu^2 \rho)/\gamma$ corresponds to the viscous length scale [13]. The latter is characteristic to the fluid motion and denotes the moment from which viscous forces become relevant for the breakup. $l_c = \sqrt{\gamma/(\rho g)}$ is the capillary length scale and denotes the relative dominance of capillary over gravitational forces (typically $\sim$ 1 mm).

Due to the universality of the singularity at the breakup point, d$_{min}$ cannot depend on macroscopic scales in the limit $l_t \to 0$, so $\bar{f}$ should remain finite for $l_c/l_t \to \infty$ and $d_0/l_t \to \infty$, which reduces (2.10) to [10]:

$$d_{min} = l_t \bar{f}\left(\frac{\Delta z}{l_t}, \frac{l_\nu}{l_t}\right) \tag{2.11}$$

Equation (2.11) cannot be further simplified by dimensional analysis so further approximations need to be made that take into account the local force balance. The latter gives rise to three different self-similar regimes each of which is governed by a different scaling law (cf. Tab.2.1) [14]:

i. **Generic:** surface tension - viscosity - inertia balance

ii. **Viscous:** viscosity - inertia balance

iii. **Inviscid:** surface tension - inertia balance

While (i) characterizes merely the very last stages of the pinch-off, (ii) and (iii) constitute transient regimes that are dependent on the fluid parameters and

TABLE 2.1: Drop breakup regimes.

	Flow regime	Force balance	Scaling	Solution	Ref.
(i)	generic	γ, η and ρ	$d_{min} \propto \tau$	Navier-Stokes	[15]
(ii)	viscous	γ and η	$d_{min} \propto \tau$	Stokes	[16]
(iii)	inviscid	γ and ρ	$d_{min} \propto \tau^{2/3}$	Euler	[17, 18]

indicate the transient realization of different force balances. A useful parameter to anticipate the (transient) pinch-off behaviour of a Newtonian fluid is the Ohnesorge number Oh [19]:

$$Oh = \eta / \sqrt{\rho d_0 \gamma} \tag{2.12}$$

Oh compares the size of the initial drop diameter d_0 to the viscous length scale. For $Oh << 1$ viscosity is (initially) negligible, and the drop breakup is solely antagonized by inertia. The observed minimum neck diameters d_{min} are larger than l_v. For $Oh >> 1$, viscous forces dominate and inertia is (initially) irrelevant. The corresponding observed minimum neck diameters are analogously smaller than l_v.

The viscosity of the thinning fluid directly impacts the rate at which the breakup occurs, which is reflected in the viscous time scale t_v [13]:

$$t_v = (\nu^3 \rho^2)/\gamma^2 \tag{2.13}$$

Hence if viscosity is doubled, the breakup is slowed down by a factor of eight, which explains the differences between the characteristic free surface shapes observed near the pinch-off region: in both cases a self-similar geometry is adopted, irrespective of the initial conditions [20]. Yet viscous breakup is characterised by long threads, whereas a double cone is observed in the inviscid case [17, 18].

Ultimately, for sufficiently small times to pinch-off, both the viscous (ii) and the inviscid regime (iii) will cross-over to the generic scaling solution (i) accommodating thereby the universality of the singularity at the pinch-off point [21, 22].

2.2.2 Inviscid pinch-off

In this thesis we will exclusively focus on non-viscous fluids and therefore only consider the pinch-off dynamics of the inviscid regime. The thinning of the fluid filament is solely driven by surface tension while viscous effects remain negligibly small. As already indicated in Tab. 2.1, the corresponding fluid dynamics can be accounted for by the Euler solution [14, 21] and the minimum neck diameter scales with the time to pinch-off through a $2/3-$power law:

$$d_{min} = A \left(\frac{\gamma}{\rho}\right)^{1/3} \tau^{2/3} \tag{2.14}$$

where A is a dimensionless proportionality constant ('prefactor') and τ denotes the time to pinch-off.

In close proximity to the rupture point the shape of the thinning fluid filament adopts a self-similar conical shape with entrance angles of 18.1° and 112° respectively [17]. The self-similarity of this 'double cone' implies that initial conditions do not affect the local structure in the pinch-off region. Despite of this, the trajectory towards this geometry might indeed vary with initial conditions such as the nozzle diameter or the speed of dripping [23].

Fig. 2.6 depicts this characteristic conical shape observed for inviscid fluids for various times to pinch-off. At the very last instants of the breakup, the drop profile overturns (Fig. 2.6C right) and adopts an 'apple-stem' geometry that obscures the area of interest [23, 24]. The actual rupture therefore occurs in a region that is optically not accessible, which limits the possibilities of experimentally approaching these last moments with conventional ultrafast imaging techniques. In chapter 5, we will discuss an alternative method based on conductivity, that is presumed to allow an experimental access to the nanometre scale.

The crossover to the generic regime is expected to occur at times $\tau \sim t_v$ and length scales $l_t \sim l_v$. Since inviscid fluids have extremely short viscous length scales of $\sim$ nm (e.g. $l_v(H_2O)$ = 10 nm) and correspondingly short viscous time scales, viscosity usually does not play a role in experimental investigations [21].

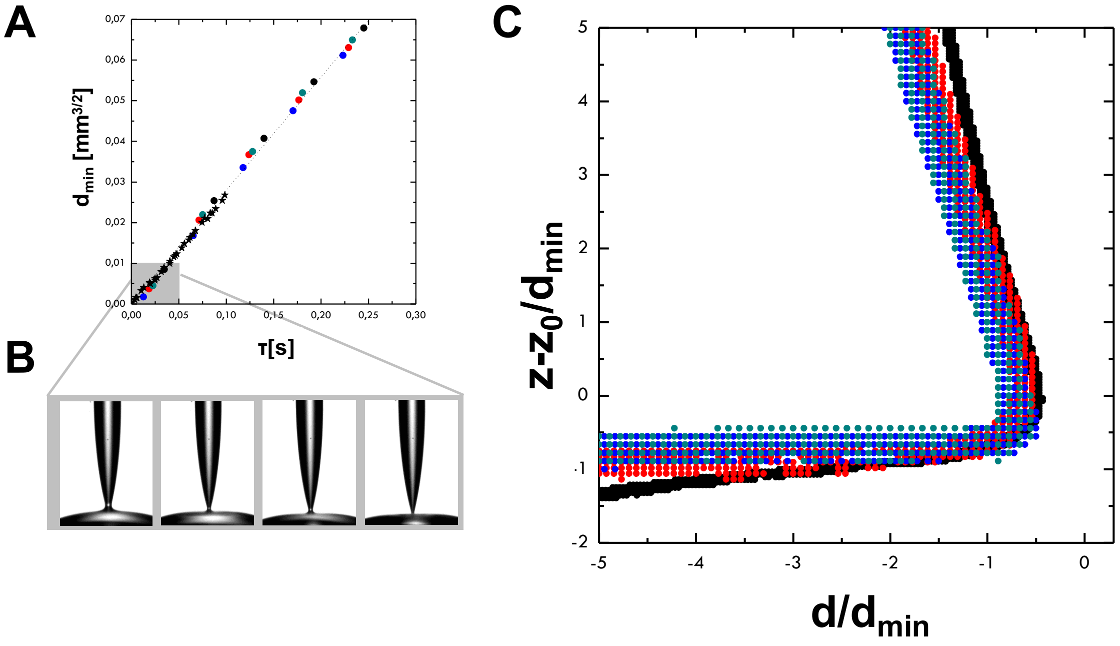

FIGURE 2.6: **Self-similarity.** A: Pooled experimental data from a single inviscid fluid. B: Ultrarapid images from the last visually accessible instants before breakup. C: Rescaled drop shapes for different times to pinch-off τ.

2.3 Diffusion

Diffusion processes are the driving forces of many biological and industrial processes and therefore a thorough understanding of the associated dynamics constitute a worthwhile endeavour for both scientists and engineers. In chapter 3 we will focus on the diffusion of protons in a complex environment which is mechanistically not trivial and therefore requires a solid foundation of the key principles of diffusion theory.

2.3.1 Principles of diffusion

Classical diffusion theory relies on the Brownian motion of suspended particles in a fluid, where the random diffusive path is determined by the collision with other particles. The number of Brownian particles diffusing from a high to a low concentration region can be estimated as particular solution to Fick's diffusion equation:

$$\frac{\delta N}{\delta t} = D\frac{\delta^2 N}{\delta x^2} \tag{2.15}$$

where t refers to the elapsed diffusion time since $t = 0$, N is the number of diffusing particles, D the diffusion coefficient and x the length of the diffusive path.

Any suitable solution to this differential equation (first order with respect to time, second order with respect to space) needs to satisfy one initial (i) and two boundary (ii,iii) conditions. Fig. 2.7 shows a schematic sketch of the diffusion problem that we will encounter in chapter 3: (i) at time $t = 0$ all N_0 particles are assumed to be concentrated on one plane (*here*: the $yz-$plane) which leads to a diffusive flux J along the $x-$axis. The particles correspondingly move a certain distance Δx along their concentration gradient towards the low concentration region. Assuming further that (ii) the absolute number of particles N_0 remains constant and (iii) that particle concentrations must be finite over the entire diffusion space, allows to solve equ. 2.15 for this particular case [25]:

$$N = \frac{N_0}{A(\pi D t)^{1/2}} e^{-x^2/4Dt} \tag{2.16}$$

Based on (2.16) particle concentrations for any given space and time coordinates can be derived (Fig. 2.8). For each time t, a characteristic particle concentration curve is obtained from which the mean square displacement of the particle can be calculated:

$$\langle x \rangle = \int_a^\infty xNAdx/N_0 = (1/\pi D t)^{1/2} \int_a^\infty x e^{-x^2/4Dt} dx = 2(Dt/\pi)^{1/2} \tag{2.17}$$

The diffusion coefficient itself is a particle specific entity and depends further on both the temperature T and the dynamic viscosity η of the medium, which is described by:

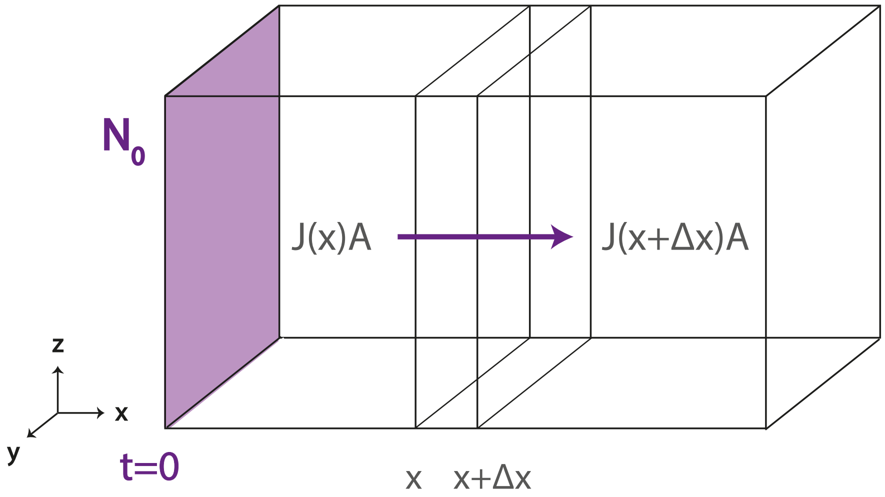

FIGURE 2.7: **Schematic of the investigated diffusion problem.** Initial condition: at $t = 0$ all N_0 particles are concentrated on one side ($yz-$plane). Boundary conditions: (i) the number of particles is finite everywhere and (ii) the total number of particles N_0 is constant throughout the entire experiment.

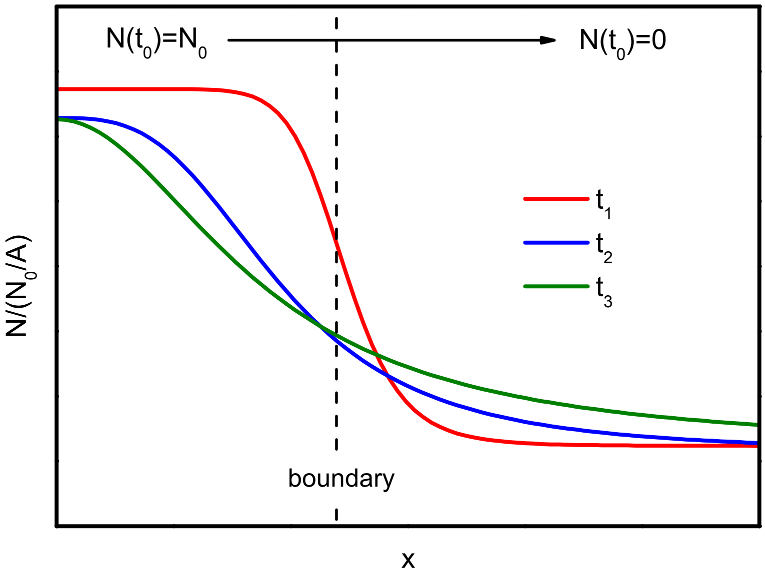

FIGURE 2.8: **Diffusion profiles.** Change in particle concentration profiles over time (c.f. eq. 2.15).

$$D = \frac{RT}{6\pi\eta r} \tag{2.18}$$

where R is the universal gas constant and r the radius of the particle [26, 27].

2.3.2 Proton diffusion in bulk water

Protons (and hydroxides) were found to exhibit anomalously high diffusion coefficients ($D_{H^+} \sim 10^{-9} m^2 s^{-1}$) in bulk aqueous solutions, which seems rather surprising when considering their radius/charge ratios that are very similar to alkali or alkaline earth metal ions ($D \sim 10^{-10} m^2 s^{-1}$).

What causes the proton to stand out to such a noticeable extent with respect to other chemically very similar ions such as Li^+, Na^+ or Mg^{2+}? First of all, unlike metal cations, free protons *per se* do not exist in water, rather they immediately form hydronium ions (H_3O^+) with surrounding water molecules. This outstanding property was further investigated by Eigen [28] and Zundel [29] who proposed the existence of two hydration complexes, referred to as 'Eigen' ($H_9O_4{}^+$) and 'Zundel' ($H_5O_2{}^+$) ion respectively. Ultrafast proton diffusion is enabled through continuous interconversion between these two limiting structures, which is driven by fluctuations in the solvation shell of the hydrated ions. The resulting 'proton hopping' therefore does not involve a net transport of mass, but merely of positive charge (Fig. 2.9). This so-called 'structural diffusion' mechanism is highly dependent on the unhindered rotation of the water molecules in close proximity to the diffusing proton. Recent experimental evidence suggests that $\sim$ 10 water molecules need to reorientate/ are involved in the transfer of a single proton charge [30]. More recent literature suggests the existence of even higher-order structures such as unique $H_{13}O_6{}^+$ entities [31]. After all, the full dynamics of a diffusing proton in a hydrogen bond network are yet to be completely understood and lie beyond the scope of this thesis.

2.4 Microfluidics

Since the phenomena studied in this thesis occur at very short time and length scales, microfluidic devices were used at various stages to generate a suitable experimental environment. Generally speaking, the term 'microfluidics' subsumes the dynamic study of very small fluid sample volumes ($\sim$ µl) in microconfined

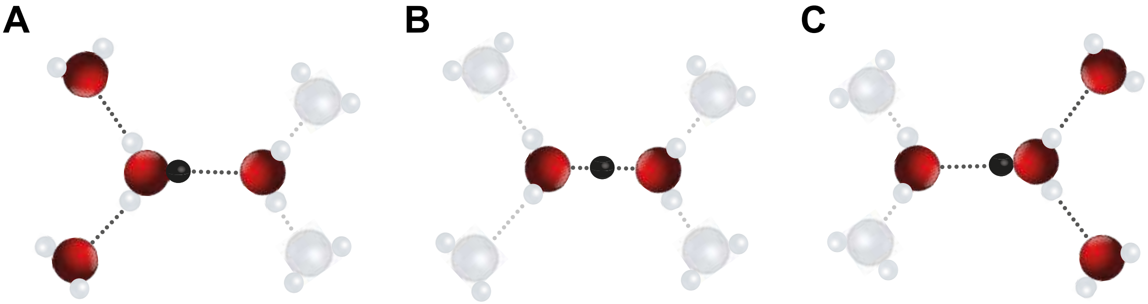

FIGURE 2.9: **Grotthus mechanism and Eigen-Zundel-interconversion.** A: Eigen ion ($H_9O_4^+$) B: Formation of a Zundel ion ($H_5O_2^+$) C: Formation of a new Eigen ion

channel environments (~ 100 nm $-$ 500 µm). The use of such microscale devices is interesting for many fundamental and applied interdisciplinary research questions that range from high-throughput screening and single-cell studies to chemical process optimization and molecular synthesis [32, 33].

The remarkable advantages brought about by these microfabricated tools become apparent when looking at the associated Reynolds numbers given by [34, 32]:

$$Re = \frac{\rho v D_H}{\eta} \tag{2.19}$$

where v corresponds to the average fluid velocity inside the channel and η is the dynamic viscosity of the fluid. D_H denotes the hydraulic diameter and can be approximated with $D_H = 4A/P_{wet}$. A is the cross-sectional area of the channel and P_{wet} the wetted perimeter of A.

At the reduced dimensions of a microchannel the Reynolds number is usually very low ($Re << 100$), which results in a purely laminar flow regime. Under such conditions, inertia is negligible and the Navier-Stokes equation that usually governs fluid flow behaviour can be simplified to the so-called Stokes equation:

$$0 = -\vec{\nabla} P + \eta \vec{\nabla}^2 \vec{v} \tag{2.20}$$

where $\vec{v}$ denotes the vector field of the fluid velocity and P the pressure inside the fluid [35, 32].

The solution to this equation depends on the shape of the microchannel itself. In the case of cylindrical channels, a parabolic flow profile develops, which is described by the Hagen-Poiseuille equation [36]:

$$\Delta P = \frac{32\eta L v}{D^2} \tag{2.21}$$

whereby L denotes the total length of the channel, D the channel diameter and v the average velocity of a cross-sectional slice of the channel. As depicted in Fig. 2.10 the fluid flow speed reaches its maximum value in the centre of the channel and is equal to zero at the channel walls ('no slip boundary condition').

The absence of convective flows allows for very precise control of experimental conditions (temperature, concentration, pH etc.) and facilitates minute manipulations. This is particularly interesting for our experiments, that focus on isolated physical parameters such as surface tensions and diffusion coefficients.

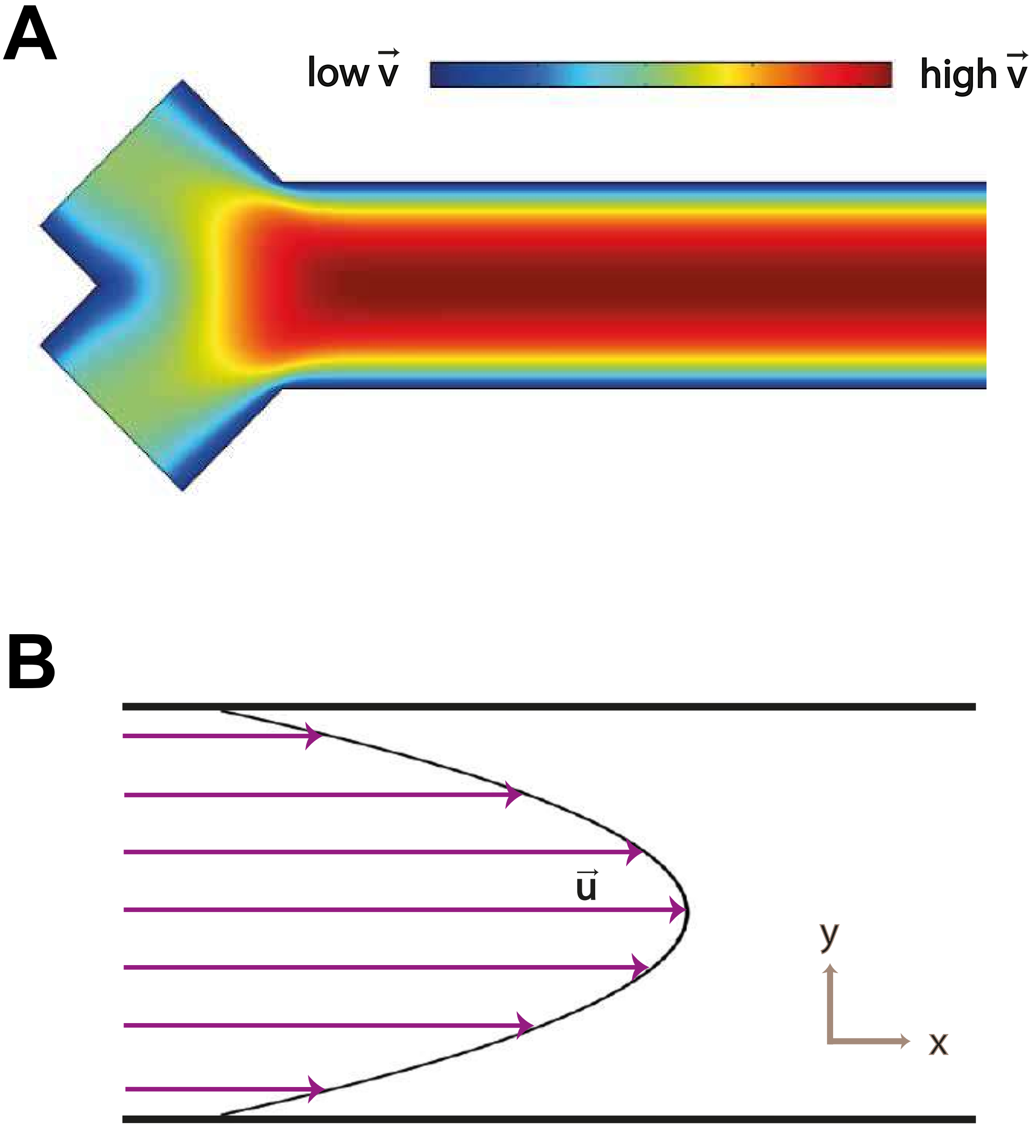

FIGURE 2.10: **Fluid dynamics in microfluidic channels** A: Velocity distribution in microfluidic Y-shaped channel. B: Parabolic flow profile.

Bibliography

[1] J. N. Israelachvili. *Intermolecular and Surface Forces (Third Edition)*. Academic Press, San Diego, 2011.

[2] P. G. de Gennes, F. Brochard-Wyart, and D. Quere. *Capillarity and Wetting Phenomena: Drops, Bubbles, Pearls, Waves*. Springer, New York, 2003.

[3] J. Lyklema. *Fundamentals of Interface and Colloid Science*, volume III: Liquid-Fluid Interfaces. Academic Press, London, 2000.

[4] T. Young. An Essay on the Cohesion of Fluids. *Philosophical Transactions of the Royal Society of London*, 95:65–87, 1805.

[5] C.-H. Chang and E. I. Franses. Adsorption dynamics of surfactants at the air/water interface: a critical review of mathematical models, data, and mechanisms. *Colloids and Surfaces A: Physicochemical and Engineering Aspects*, 100:1–45, 1995.

[6] A. J. Prosser and E. I. Franses. Adsorption and surface tension of ionic surfactants at the air-water interface: review and evaluation of equilibrium models. *Colloids and Surfaces A: Physicochemical and Engineering Aspects*, 178(1-3):1–40, 2001.

[7] S. A. Safran. *Statistical Thermodynamics of Surfaces, Interfaces, and Membranes (Frontiers in Physics)*. Westview Press, 2009.

[8] L. D. Landau and E.M. Lifshitz. *Fluid Mechanics*. Pergamon Press Verlag, 1984.

[9] J. Eggers. Nonlinear dynamics and breakup of free-surface flows. *Reviews of Modern Physics*, 69(3):865–930, 1997.

[10] J. Eggers and T.F. Dupont. Drop formation in a one-dimensional approximation of the Navier Stokes equation. *Journal of Fluid Mechanics*, 262:205–221, 1994.

[11] G. I. Barenblatt. *Scaling, Self-similarity, and Intermediate Asymptotics*. Cambrdige University Press, Cambridge, 1996.

[12] J. Eggers and M. A. Fontelos. *Singularities: Formation, Structure, and Propagation*. Cambridge Texts in Applied Mathematics, Cambridge, 2016.

[13] A. Haenlein. *Forsch. auf dem Gebiete des Ingenieurwesens/Reihe A*. Thesis, 1931.

[14] J. Eggers and E. Villermaux. Physics of liquid jets. *Reports on Progress in Physics*, 71(3):036601, 2008.

[15] J. Eggers. Universal pinching of 3D axisymmetric free-surface flow. *Phys. Rev. Lett.*, 71:3458–3460, Nov 1993.

[16] D. T. Papageorgiou. On the breakup of viscous liquid threads. *Physics of Fluids*, 7(7):1529–1544, 1995.

[17] R. F. Day, E. J. Hinch, and J. R. Lister. Self-Similar Capillary Pinchoff of an Inviscid Fluid. *Physical Review Letters*, 80(4):704–707, 1998.

[18] Y.-J. Chen and P. H. Steen. Dynamics of inviscid capillary breakup: collapse and pinchoff of a film bridge. *Journal of Fluid Mechanics*, 341:245–267, 006 1997.

[19] W. V. Ohnesorge. Die Bildung von Tropfen an Düsen und die Auflösung flüssiger Strahlen. *Zeitschrift für Angewandte Mathematik und Mechanik*, 16(6):355–358, 1936.

[20] D. H. Peregrine, G. Shoker, and A. Symon. The bifurcation of liquid bridges. *Journal of Fluid Mechanics*, 212:25–39, 003 1990.

[21] J. Eggers. Drop formation – an overview. *ZAMM - Journal of Applied Mathematics and Mechanics*, 85(6):400–410, 2005.

[22] A. Rothert, R. Richter, and I. Rehberg. Formation of a drop: viscosity dependence of three flow regimes. *New Journal of Physics*, 5(1):59, 2003.

[23] J. R. Castrejón-Pita, A. A. Castrejón-Pita, E. J. Hinch, J. R. Lister, and I. M. Hutchings. Self-similar breakup of near-inviscid liquids. *Physical Review E*, 86(1):015301, 2012.

[24] J. C. Burton, J. E. Rutledge, and P. Taborek. Fluid Pinch-Off Dynamics at Nanometer Length Scales. *Physical Review Letters*, 92(24):244505, 2004.

[25] P. Atkins. *Atkins' Physical Chemistry*. Oxford University Press, 2009.

[26] M. von Smoluchowski. Zur kinetischen Theorie der Brownschen Molekularbewegung und der Suspensionen. *Annalen der Physik*, 326(14):756–780, 1906.

[27] A. Einstein. Über die von der molekularkinetischen Theorie der Wärme geforderte Bewegung von in ruhenden Flüssigkeiten suspendierten Teilchen. *Annalen der Physik*, 322(8):549–560, 1905.

[28] M. Eigen. Proton Transfer, Acid-Base Catalysis, and Enzymatic Hydrolysis. Part I: ELEMENTARY PROCESSES. *Angewandte Chemie International Edition in English*, 3(1):1–19, 1964.

[29] P. Schuster, G. Zundel, and C. Sandorfy.

[30] K. J. Tielrooij, R. L. A. Timmer, H. J. Bakker, and M. Bonn. Structure Dynamics of the Proton in Liquid Water Probed with Terahertz Time-Domain Spectroscopy. *Physical Review Letters*, 102(19):198303, 2009.

[31] E. S. Stoyanov, I. V. Stoyanova, and C. A. Reed. The unique nature of H^+ in water. *Chemical Science*, 2(3):462–472, 2011.

[32] P. Tabeling. *Introduction to Microfluidics*. Oxford University Press, New York, 2010.

[33] A. J. deMello. Control and detection of chemical reactions in microfluidic systems. *Nature*, 442(7101):394–402, 2006.

[34] A. Sommerfeld. Ein Beitrag zur hydrodynamischen Erklärung der turbulenten Flüssigkeitsbewegungen. *Proceedings of the Fourth International Congress of Mathematics*, III:116–124, 1908.

[35] B. J. Kirby. *Micro- and Nanoscale Fluid Mechanics: Transport in Microfluidic Devices*. 2010.

[36] H. Bruus. *Theoretical Microfluidics*. Oxford University Press, 2007.

Chapter 3

Proton mobility in cellular environments

3.1 Introduction

The properties of water are fundamental to life and its ability to form dynamic hydrogen bonds with almost all the molecules in living cells is an important determinant of protein folding and activity. The same holds for DNA, RNA and the phospholipids making up cellular functions and biological membranes. The same hydrogen-bonding properties form the basis of the so-called 'Grotthus effect' that is responsible for the unexpectedly high free diffusion rates observed for proton movement in bulk water [1]. Unlike classical particle diffusion, proton displacement is believed to occur via a hopping mechanism, where net charge rather than mass is transferred (Fig. 3.1). The key factor in this mechanism are the local water dynamics, as for every transported proton a large number (~ 10) of water molecules need to reorientate [2]. Water reorientation dynamics are very sensitive to changes in the chemical environment which renders predicting proton diffusion behaviour in more complex solutions quite challenging. At the same time, protons are just as water considered crucial determinants for the properties of the molecules of life and affect cellular metabolism in many ways: the energy household of cells is primarily regulated by transmembrane proton gradients that drive ATP synthesis. Similarly, key enzyme activities of the central carbon metabolism are primarily modulated through the interference with protons. There is also growing evidence that protonation events control metabolic signal transduction pathways at the level of signalling protein activities [3]. Additionally, protein interactions with phosphorylated ligands and other binding partners are determined by cytoplasmic pH ('pH_i') contributing to the control of transcriptional responses [4]. The intracellular pH_i also modulates the electrostatic properties of signalling molecules [5, 6] as a consequence of which protons can effectively have a significant influence on the control of growth and differentiation in a wide variety of cell types and organisms. A considerable impact has been revealed recently for growth [7], development [8], directional migration [9], embryogenesis [10], ageing [11] and tumorigenesis [12].

Other recent studies have shown the emerging signalling role of protons and the natural occurrence of cytoplasmic proton gradients in yeast and vertebrate systems [11, 9]. They were proposed to be relevant to the generation of young undamaged daughter cells from ageing yeast mothers and for directional migration in germ cells. Thus, in this context, the intracellular proton concentration has even been suggested to function as a novel second messenger [13]. The important role of second messengers such as Ca^{2+} and cAMP was already recognized in the 1950s [14]. These small molecules can interact with the cellular network at multiple sites, thereby integrate signals and relay them in order to generate the required outputs. The intracellular concentrations of these second messengers often vary rapidly in the cell and their controlled generation normally occurs locally, which results in their diffusion limited spatial distribution within the cell.

The hypothesis of existing intracellular gradients contrasts with the classical assumption of intracellular pH levels being kept around or slightly above neutrality within the scope of physiological homoeostasis. Moreover, it is seemingly at odds with fundamental aspects of physical diffusion theory: due to the Grotthus effect and the resulting anomalously high diffusion coefficient, proton diffusion is generally considered to occur so much faster than regular particle Brownian motion [15, 16], that, as a consequence, proton gradients within a cell could not be maintained at relevant signalling time scales. A number of biophysical and theoretical biology studies were published a few decades ago predicting that proton diffusion in living cells is in fact not so fast [17]. More recent authors have shown that water structure is specifically disrupted to prevent rapid proton diffusion, for instance in trans-membrane transport through channels [18], and yet others have demonstrated that intracellular pH gradients can be induced artificially [19].

In the present work we explored the hypothesis of intracellular pH gradients on biophysical grounds by simultaneously probing proton mobility and water reorientation dynamics in cell mimicking environments. The putative existence of such gradients has raised the question as to how proton diffusion and water

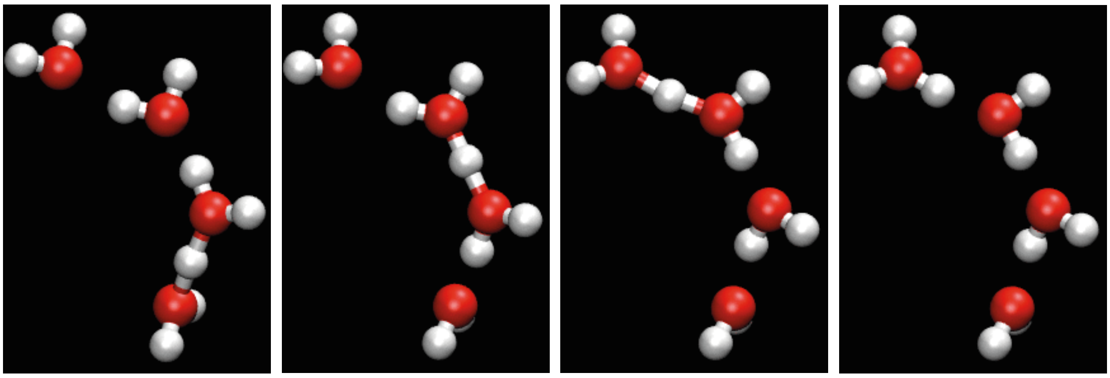

FIGURE 3.1: **Grotthus mechanism.** Proton diffuses via an ultrafast 'hopping' mechanism (*Fig. adapted from* `https://en.wikipedia.org/wiki/Grotthuss_mechanism`)

dynamics together could control the mobility of protons in living cells. We use a combined approach of microfluidic fluorescence microscopy and time-resolved femtosecond IR spectroscopy to dissect the contributions of various cytoplasmic components on the one hand and water dynamics on the other hand which together act on the proton diffusion kinetics in cell-like systems.

3.2 Materials and Methods

3.2.1 Cellular mimic

Cytosol mimicking solutions (CMS) as are used in enzyme kinetics studies for systems biology approaches [20] were prepared at pH values of 5 and 7. These CMS contain physiological concentrations of representative salts, buffers, model metabolites and proteins as shown in Table 3.2. In order to assess the isolated effect of cytosolic macromolecules, we compared CMS with and without proteins, where the proteins used was bovine serum albumin (BSA). Buffers were prepared from freshly weighed glutamic acid, to which 10 %V/V 500 mM KH_2PO_4, 1 %V/V 50 mM $CaSO_4$, 1 %V/V 200 mM $MgSO_4$ and 1 %V/V 2 M NaOH were added. The pH was set using KOH (leading to different final concentrations of K^+ in the pH 5 and pH 7 solutions). The volume was adjusted to 100 % (10 ml) for CMS without protein, and to 70 % (7 ml) for CMS with protein respectively. The latter was added to 3 g BSA giving the same final volume of 10 ml. The pH

TABLE 3.1: Composition of cell mimicking solutions (^{1,2} different concentrations at pH $5^1/7^2$ after pH adjustment with KOH)

	CMS	**CMS + protein**
Na^+	50 mM	50 mM
K^+	$272^1/339$ mM^2	$272^1/339$ mM^2
Mg^{2+}	2 mM	2 mM
Ca^{2+}	0.5 mM	0.5 mM
${SO_4}^{2-}$	2.5 mM	2.5 mM
Phosphate	50 mM	50 mM
Glutamate	250 mM	250 mM
Phosphate	50 mM	50 mM
BSA	-	30 %w/V

was re-verified and when necessary adjusted. This procedure ensured that the final concentrations (with the exception of [K^+]) were the same for all CMS with and without protein addition. All CMS solutions were filter-sterilized and stored at 4°C until use. Prior to the experiments the viscosity of each CMS solutions was determined using a modular compact rheometer (MCR 302, Anton Paar) with a plate-plate geometry.[1]

3.2.2 Determination of proton diffusion coefficients using a microfluidic setup

Proton diffusion is known to be extremely fast and quantitative derivation of accurate diffusion coefficients is challenging. Known methods for determining proton diffusion coefficients such as conductivity measurements [21] proved to be unsuitable for our purpose due to the abundance of salts and buffers in the CMS with respect to the low physiological proton concentrations.

We used the well-controlled reaction environment of a micrometric Y-shaped glass channel (45 µm width and 20 µm height, Micronit) that allows for purely diffusive mixing of two inlet streams (Fig. 3.2B and C). We dyed all solutions with pH-sensitive fluorophore (Fluorescein, 25 µM) the fluorescence of which rapidly decreases below its first pKa of 6.4. For each experiment two different pH values of the same solution were injected into the two channel inlets by the

---

[1] The cell mimicking solutions were prepared by Gertien Smits (University of Amsterdam).

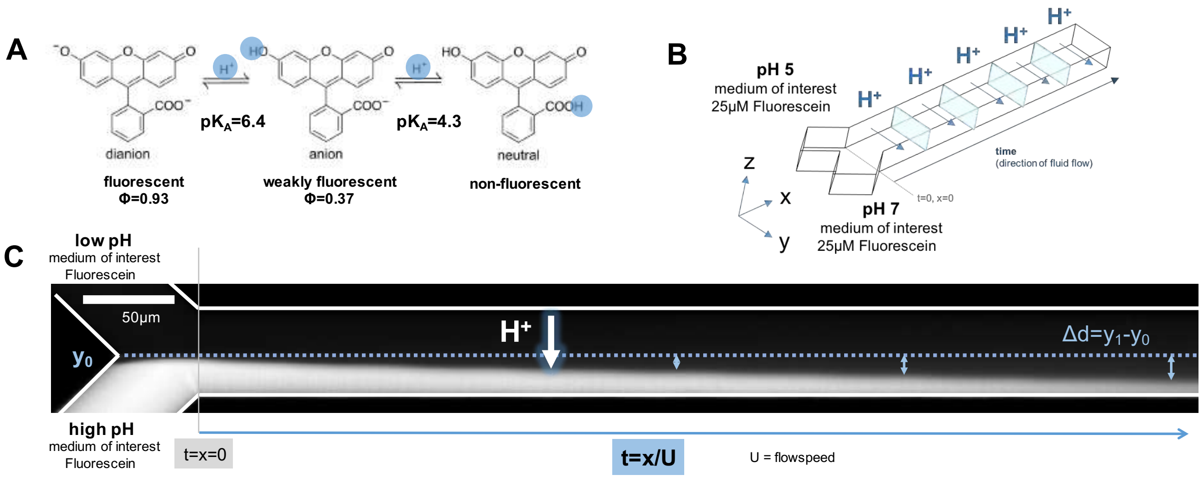

FIGURE 3.2: **Determination of proton diffusion coefficients.** A: pH sensitivity of Fluorescein: the fluorescence quantum yield sharply decreases as soon as $pH < pKA = 6.4$ B: Microfluidics experimental setup: two fluids that differ only in their respective proton concentrations are injected in a Y-shaped microfluidic glass channel at different constant flowrates ($0.1-5\,\mu l\,min^{-1}$) and the resulting interdiffusion process is followed by fluorescence microscopy. Protons diffuse along their concentration gradient in $y-$direction, whereas the $x-$coordinate is correlated to the interdiffusion time. (c) Principles of fluorescence microscopy image analysis: the diffusion coefficient D can be directly derived from Δd in the fluorescent image. D corresponds to the slope of the curve as $\Delta d = \sqrt{Dt}$.)

help of a syringe pump (PhD 2000, Havard Apparatus). The resulting proton gradient induces a diffusive proton flux from the low pH stream (non-fluorescent) to the high pH stream (fluorescent). As the pH of the high pH stream decreases, an increasing fraction of the Fluorescein molecules is quenched which allows to directly follow the progression of the protons by confocal microscopy. At the same time, the microfluidic setup decomposes this movement into a time (t) and a space component (y) and thus the whole proton diffusion process can be grasped within a single image.

From these binary fluorescence microscopy recordings the mean proton diffusion length Δd can be determined as the distance between the center of the channel y_0 and the fluorescent front y_1 (Fig. 3.2C). This switching point corresponds to the position where the local pH has reached the value of the second pKa of Fluorescein, which is equal to pH = 6.4.

As the two inlet fluids mix by diffusion only, the square of this mean travelled distance Δd^2 is linearly dependent on the lapsed contact time t of the two fluids and the medium-specific diffusion coefficient D:

$$\Delta d^2 \approx Dt \tag{3.1}$$

The contact time t can be calculated from the intrachannel flow speed U and the distance x from the Y-junction of the channel:

$$t = \frac{x}{U} \tag{3.2}$$

Correspondingly, the proton diffusion coefficient can be directly derived from the slope of the fitted lines (c.f. 3.3).

3.2.3 Assessment of water dynamics using ultrafast IR spectroscopy

In our experiments we sought to assess the effect of biological components on water dynamics that occur on a picosecond time scale. For such extremely short times, so-called femtosecond time resolved infrared spectroscopy (fsTRIR) has been succesfully employed in the past [22, 23, 24]. The corresponding pump-probe setup is depicted in Fig. 3.3. For each measurement, the sample is first excited by a so-called 'pump' pulse and the resulting excited state is then probed by a second laser. The impact of this 'probe' pulse on the excited sample is a function of both the wavelength ω and the time t after excitation which results in a transient absorption signal $\Delta A(\omega, t)$:

$$\Delta A(\omega, t) = Absorbance_{probe} - Absorbance_{pump} \tag{3.3}$$

Since the dipole moment of water has a very strong IR absorption, exciting the OH stretch vibration would result in spectral saturation, unless an extremely thin sample is used. For this reason, fsTRIR usually probes the equivalent stretch vibration of partially deuterated water instead (6 % HDO in H_2O or CMS respectively in our experiments) which occurs at 2500 cm^{-1}. The deuteration does not affect the properties of the other water molecules and consequently leaves the hydrogen bonding network of the sample unchanged. At the same time, the

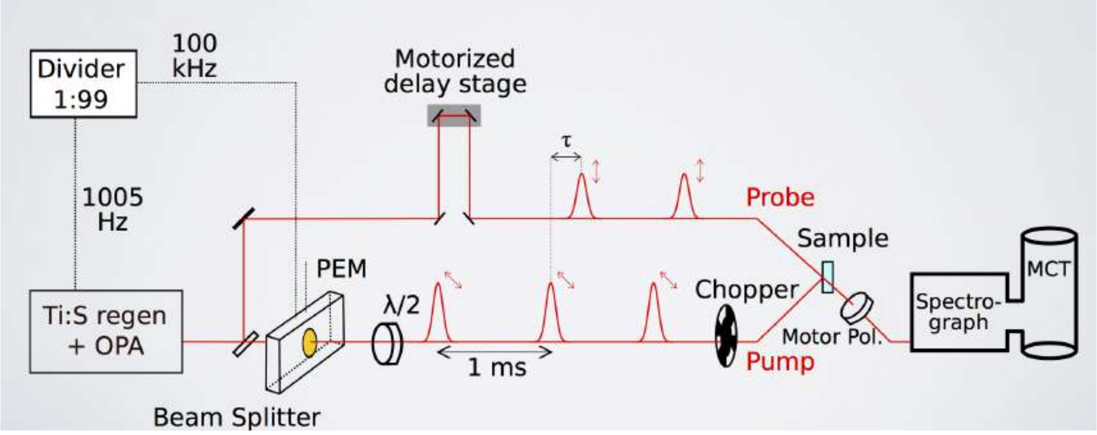

FIGURE 3.3: Experimental setup for fsTRIR measurements (*experiment performed by Martijn Tros and Sander Woutersen, University of Amsterdam*)

OD stretch vibration frequency is like the OH vibration directly related to the strength of the surrounding hydrogen bonds.

For the OD stretch vibration of the HDO molecule, a two-step decay mechanism has been found: a first relaxation to an intermediate energy level with a time constant of 1.8 ps and a second relaxation to a non-zero ground state with a time constant of 0.9 ps [25, 26] (Fig. 3.4). The non-zero end level is the consequence of ongoing sample heating during the measurements. The obtained transient absorption signal is therefore a linear combination of the pure pulse probe signal and an ingrowing heating signal:

$$\Delta A(\omega,t) = \Delta A_{end}(\omega)\left\{\frac{k_1}{(k_* - k_1)}e^{-k_* t} - \frac{k_*}{(k_* - k_1)}e^{-k_1 t} + 1\right\} \\ + N_1(0)[\sigma_{12}(\omega) - 2\sigma_{01}(\omega,0)]e^{-k_1 t} \tag{3.4}$$

where k_1, k_* are rate constants, N_1 corresponds to the number of molecules in the excited state and σ_{01}, σ_{12} denote the spectra of the different transitions.

The same pulse-probe setup can be used for assessing the anisotropy of the sample, which provides insights on the water reorientation dynamics. In these measurements (c.f. Fig. 3.5) the initially randomly oriented dipole moments of

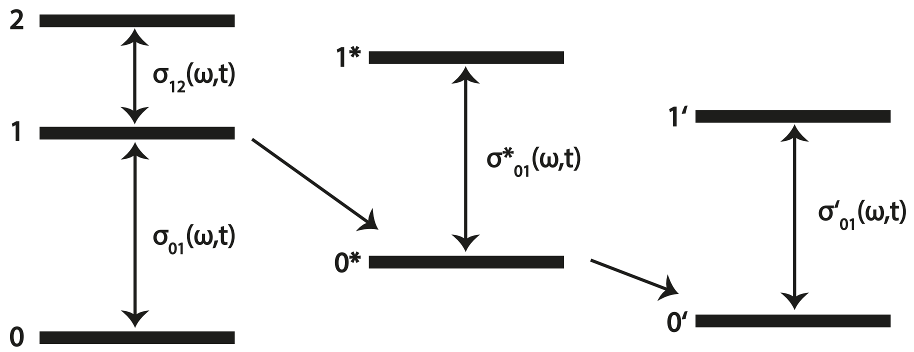

FIGURE 3.4: TRIR absorption and emission scheme for HDO in H_2O [25]

the probed chemical bond (here again the OD stretch vibration at 2500 cm^{-1}) is polarized by a 'pump' pulse. The resulting anisotropy R depends on the water reorientation dynamics and decays within a characteristic time. The measured anisotropy signal results from the transient IR absorption with the probe pulse either aligned ($\Delta A_{||}$) or perpendicular ($\Delta A_{\perp}$) to the pump pulse:

$$R(\omega, t) = \frac{\Delta A_{||}(\omega, t) - \Delta A_{\perp}(\omega, t)}{\Delta A_{||}(\omega, t) + 2\Delta A_{\perp}(\omega, t)} \tag{3.5}$$

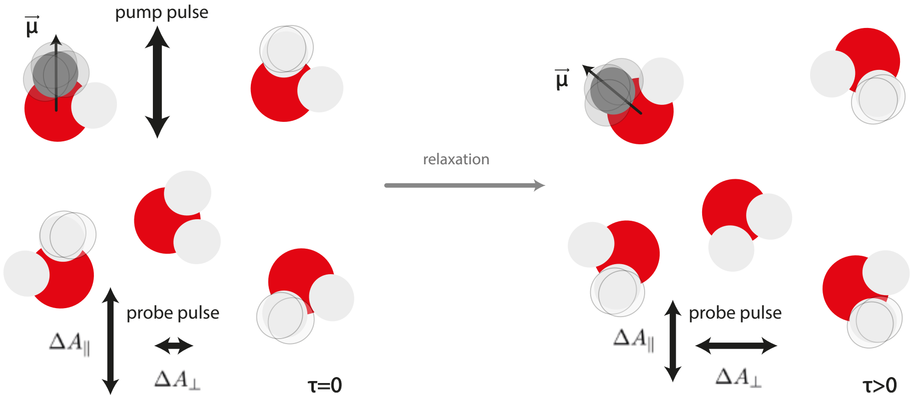

FIGURE 3.5: Principle of pulse-probe anisotropy measurements

In analogy to the simple fsTRIR measurements described above the (isotropic) sample heating needs to be accounted for by subtracting the corresponding spectral components from the measured ($\Delta A_{||}$) and ($\Delta A_{\perp}$) values. For bulk water molecules the relaxation time lies in the order of a few picoseconds ($\sim$ 2.5 ps) and becomes longer, if the free rotation is impaired. The maximum value of the anisotropy is 0.4 at $\tau = 0$ and ultimately relaxes to 0. The anisotropic decay itself is universal by nature and does therefore not depend on the probe wavelength.

3.3 Results

In the present study we sought to obtain an ameliorated mechanistic insight into proton diffusion dynamics in cellular environments by using a combined approach of microfluidic fluorescence microscopy and femtosecond time resolved infrared spectroscopy (fsTRIR). The determination of the diffusional properties of protons in true cytosol is not readily feasible. Up to date no satisfactory preparation method is known that dispenses with major perturbations such as dilution or buffer addition and the resulting fairly speculative assumptions on actual dilution factors. In addition, studying real cytosol does not allow for the assessment of the contributions of individual cellular macromolecules. We therefore generated so-called cytosol mimicking solutions (CMS) with and without protein (c.f. experimental section) and used them for studying both proton diffusion and water dynamics in comparison to bulk water.

3.3.1 Proton diffusion coefficients in bulk water and cytosolic mimic solutions

For the determination of proton diffusion coefficients in our cytosolic mimic solution we used a microfluidic confocal microscopy setup (Fig. 3.2). We first performed a control experiment where we derived diffusion coefficients for D^+ in deuterated bulk water and for H^+ in (normal) bulk water in order to check whether our method was capable of resolving the expected isotope effect. For the proton diffusion coefficient in bulk water we found a value in the order of $\sim 10^{-9}$ m^2 s^{-1}, which is consistent with previous findings [27, 28]. In contrast, D^+ diffusion in D_2O was observed to be retarded by a factor of $\sqrt{2}$ with respect to H^+ diffusion in H_2O (Fig. 3.6), which is in line with theoretical predictions assuming a Grotthus-type transport mechanism [29].

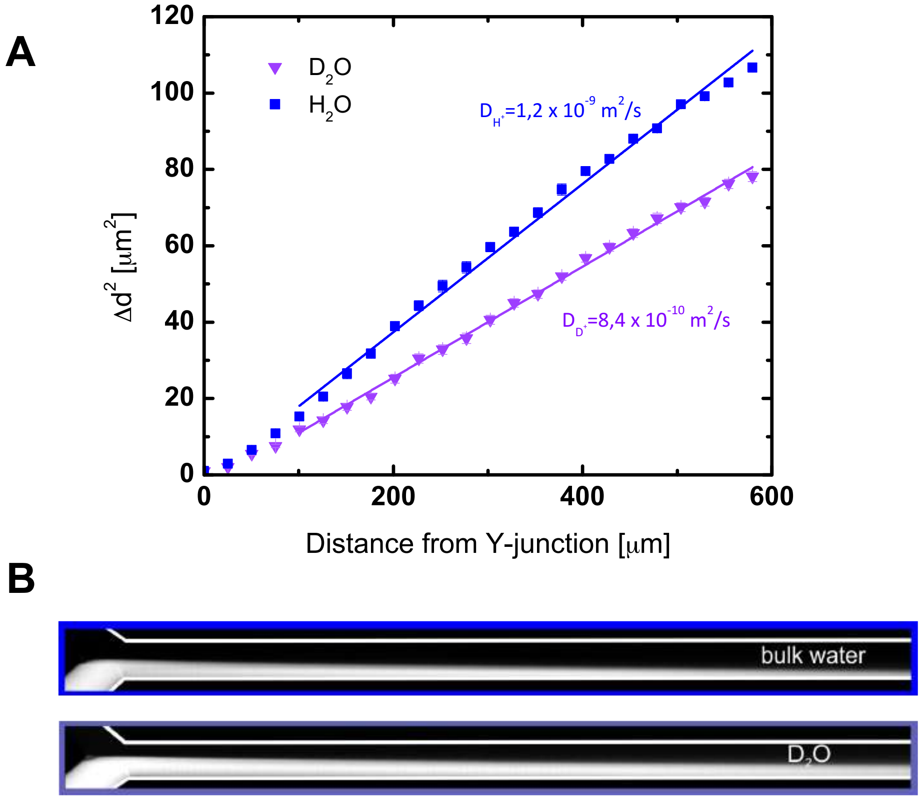

FIGURE 3.6: **Isotope effects of proton diffusion.** A: Proton diffusion in bulk water is $\sqrt{2}$ times faster than deuterium diffusion in deuterated water B: Qualitative differences in fluorescence microscopy images (flowrate = 5 µlmin^{-1}).

Since our method proved suitable for deriving fairly accurate values for the diffusion coefficients of H^+ and D^+ respectively, we concluded that it would likewise provide good quantitative estimates for proton diffusion coefficients in more complex media such as our cytosolic mimic solutions. In all of these solutions, proton mobility was found to be dramatically decreased (Fig. 3.7). In the absence of any macromolecules (CMS w/o protein) the derived proton diffusion coefficient was an order of magnitude lower than in bulk water. When physiological amounts of the model protein BSA were added (CMS + protein), we observed a further retardation of proton diffusion by $\sim$ a factor of 3 (Tab. 3.2).

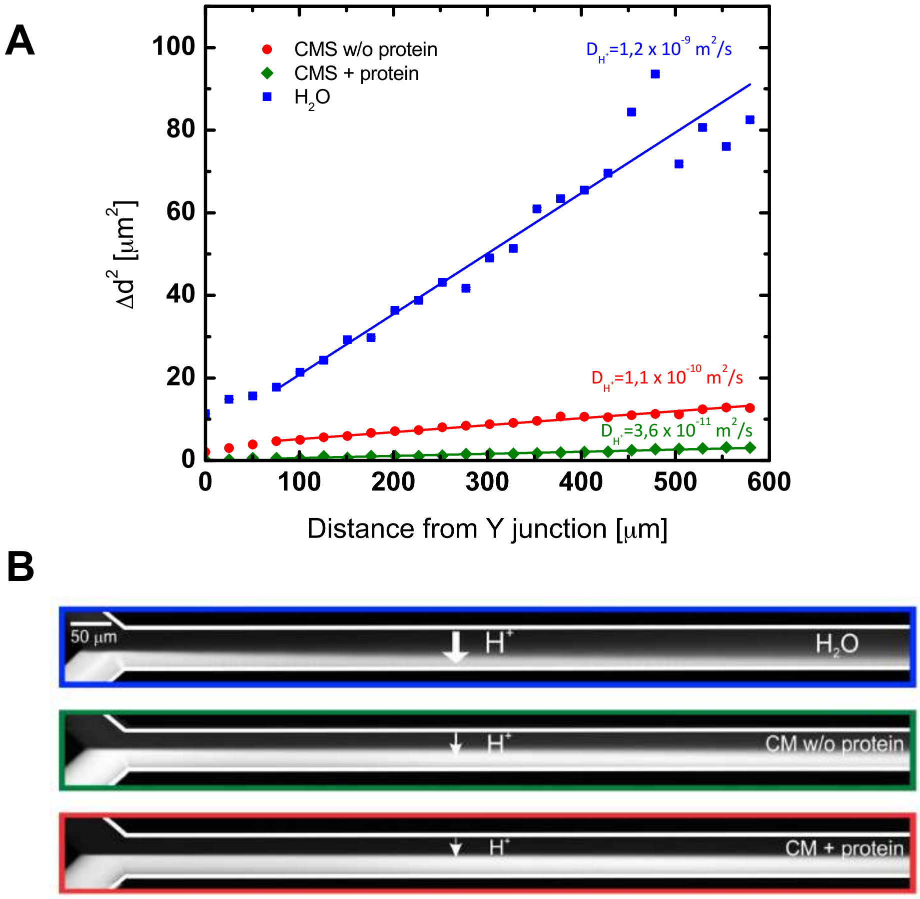

FIGURE 3.7: **Qualitative and quantitative determination of H^+ diffusion coefficients.** Top: diffusion coefficient fits for bulk water vs. CMS (flowrates = 5 μlmin^{-1} and 250 nlmin^{-1} respectively). The proton diffusion coefficient in the CMS was found to be retarded by a factor of 10 (without proteins) and 30 (in the presence of proteins). Bottom: fluorescence microscopy pictures obtained from microfluidics experiments for bulk water (upper channel), CMS without protein (middle channel) and CMS with protein (lower channel) (flowrate = 0.5 μlmin^{-1})

TABLE 3.2: Proton diffusion coefficients found in different aqueous milieus

	Diffusion coefficient $\times 10^{-9}$ [m^{2}s^{-1}]	**Viscosity** [mPas]
Bulk water	1.2 ± 0.10	1
CMS	0.11 ± 0.03	1
CMS + protein	0.036 ± 0.001	10
D_2O	0.84 ± 0.02	1
Glycerol	0.19 ± 0.04	10

3.3.2 Origin of proton diffusion retardation in cytosolic mimic solutions

There are several possible explanations for this large discrepancy between bulk water proton mobility and proton diffusion in a cell-like chemical environment: a change in water reorientation dynamics slowing down the Grotthus mechanism, a decrease in the amount of 'free' protons through buffer binding or an increase in the viscosity of the transport medium. Our additional experiments therefore served to further investigate and quantify the effect of these individual contributions.

Role of water reorientation dynamics

We first investigated whether a change in water dynamics could account for the observed reduction of the proton diffusion coefficients in our cell-like solutions.[2] After all, the water dynamics of such heavily charged aqueous milieus are very likely to be affected by the presence of the dissolved molecules. The Grotthus effect essentially depends on the reorientation dynamics of the water molecules in close proximity to the diffusing proton. As a result, impaired water dynamics are expected to directly translate into a retardation of Grotthus-like proton diffusion [30, 28, 18]. Since water dynamics - noticeably the reorientation of water molecules - occur on a picosecond time-scale, we used so-called femtosecond

---

[2] Experiments on water reorientation dynamics were conceived and carried out by Martijn Tros and Sander Woutersen (University of Amsterdam).

time resolved infrared spectroscopy (fsTRIR) to be able to observe potential alterations in the hydrogen bonding network (Fig. 3.8).

The static FTIR spectra of the OD stretch vibration band at 2500 cm^{-1} were found to be almost identical for the cytosolic mimic solutions and bulk water indicating a similar strength and spread of the respective hydrogen bonding networks (Fig. 3.8A). It is remarkable that even the presence of very high protein concentrations is not reflected in the spectra.

The actual water reorientation dynamics were probed by femtosecond time-resolved anisotropy measurements and are displayed in Fig. 3.8B. As a control we used 5 M TMU, which is known to strongly impair the rotational mobility of water molecules by methyl group mediated hydrophobic hydration which, in turn, reduces proton mobility [28]. We found that the water reorientation dynamics in CMS without protein are barely changed with respect to bulk water. Considering the high amounts of contained salts and buffers, this is a rather unexpected finding. In the presence of proteins a slight offset of the relaxation time can be observed indicating the existence of a small slow water fraction ($\sim$ 20 %). Proteins have previously been found to have a substantial water-structuring effect [31] and on these grounds, we were again surprised not to find a more pronounced slow water fraction. Given the high protein concentrations in these samples, this would only have been reasonable.

Clearly, a change in water dynamics cannot sufficiently account for the observed decrease in proton mobility by several orders of magnitude in cell-like solutions. The Grotthus mechanism, however, is primarily dependent on the water dynamics and is unlikely to be slowed down by an order of magnitude by anything else. This strongly suggests that proton diffusion in cells is different from bulk water diffusion and occurs according to a more complex mechanism.

Role of cytosolic buffers

Since a change in water reorientation dynamics cannot (satisfyingly) account for the observed 10-30× reduction of the proton diffusion coefficients in our cell mimicking solutions, other effects originating from the cytosolic components must be in place. In all CMS the relative abundance of protons is actually very

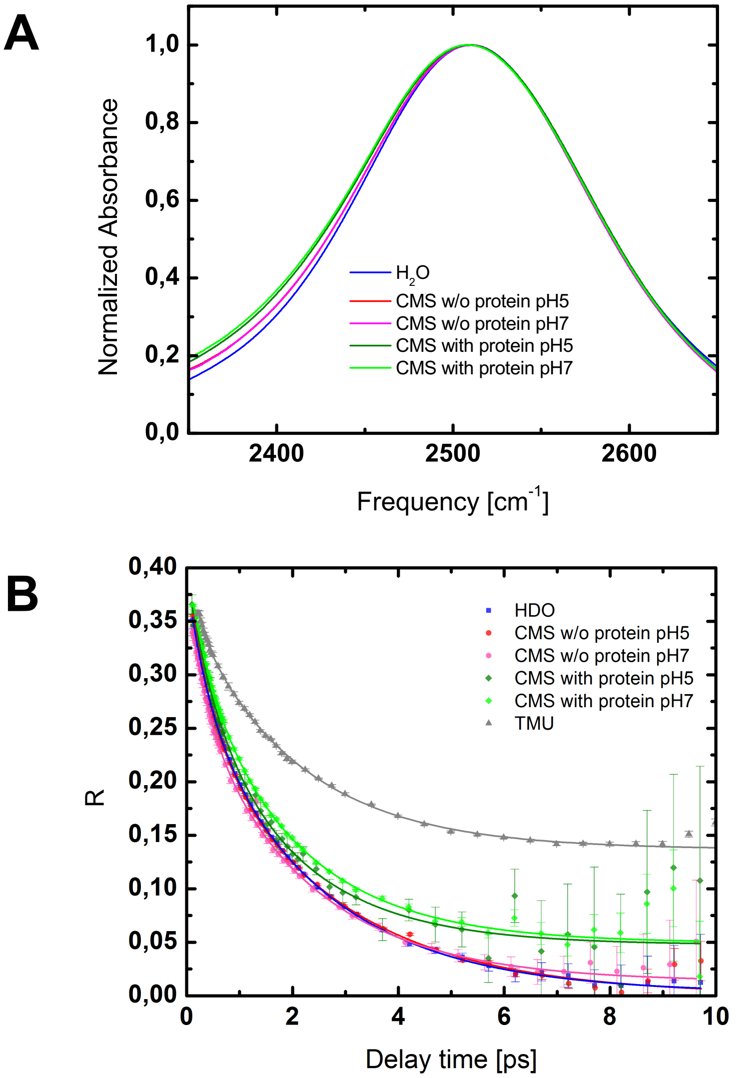

FIGURE 3.8: **IR spectroscopy of water dynamics.** A: Static FTIR: Background corrected OD stretch vibration at 2500 cm^{-1} of cytosolic mimic solutions and bulk water (6% HDO). The high degree of spectral overlap with an almost identical full with half maximum (FWHM) of 160 cm^{-1} indicates a similar degree of hydrogen bonding in all examined solutions. B: Time-resolved femtosecond anisotropy measurements: water reorientation dynamics in cytosolic mimic solutions without proteins are unchanged with respect to bulk water. In the presence of proteins a small slow water fraction (~ 20 %) can be observed (*experiments performed by Martijn Tros and Sander Woutersen, University of Amsterdam*).

low ($\sim 10^{-5}$M $- 10^{-7}$M) with respect to the (physiological) buffer concentrations ($\sim 10^{-1}$M - 10^{-2}M). At pH 5 the predominant phosphate species is $H_2PO_4{}^-$ ($\sim$ 50 mM) from which ca. 50 % ($\sim$ 25 mM) dissociate at pH 7 (pK_{a2} = 6.2). Likewise, ca. 20 % ($\sim$ 50 mM) of the contained glutamate ($pK_{\gamma-COOH}$ = 4.3) is protonated at pH 5 and fully dissociated at pH 7. Consequently, a minimum of 25 mM (pH 7) and a maximum of 100 mM (pH 5) of protons are carried on buffer molecules, which is 3-4 orders of magnitude more than the 'free' (or water carried) protons. Therefore, regardless whether proton hopping takes place or not, we are presumably not observing this, as the majority of protons diffuse bound to cytosolic buffers. The diffusion coefficient of most cytosolic buffers is $\sim 10^{-10}$m^2 s^{-1} [32] which would explain the measured tenfold reduction of the proton diffusion coefficient in the CMS without protein.

However, in the presence of macromolecules such as proteins, this relatively simple reasoning does not hold any more. The observed reduction of proton diffusion in the cytosolic solutions containing 30 %w/w of proteins is 30-fold, so additional effects must play a role. Most remarkably, the two different CMS differ in their respective macroscopic viscosities by a factor of 10 (Tab. 3.2). Medium viscosity and particle diffusion are generally believed to be closely related: for example, classical particle diffusion theory according to Stokes-Einstein predicts that the diffusion coefficient for a given species decreases linearly with increasing medium viscosity [33].

Role of viscosity

In order to closer examine the pure effect of viscosity on proton mobility we performed an additional control experiment in a highly viscous glycerol-water mixture (ca. 60 %w/w Glycerol, γ = 10 mPas). We used the same microfluidic setup as before, but did not add any further compounds such as buffers or salts this time. If protons diffused as simple particles, the Stokes-Einstein equation would predict a tenfold decrease in the diffusion efficient in a solution with a ten times higher viscosity. However, the observed reduction is only 6 to 6.5-fold. Together with the fact that the CMS with proteins only causes a 3-fold reduction of the proton diffusion coefficient, these observations demonstrate that proton diffusion, indeed, does not occur according to a classical particle diffusion mechanism (Fig. 3.9).

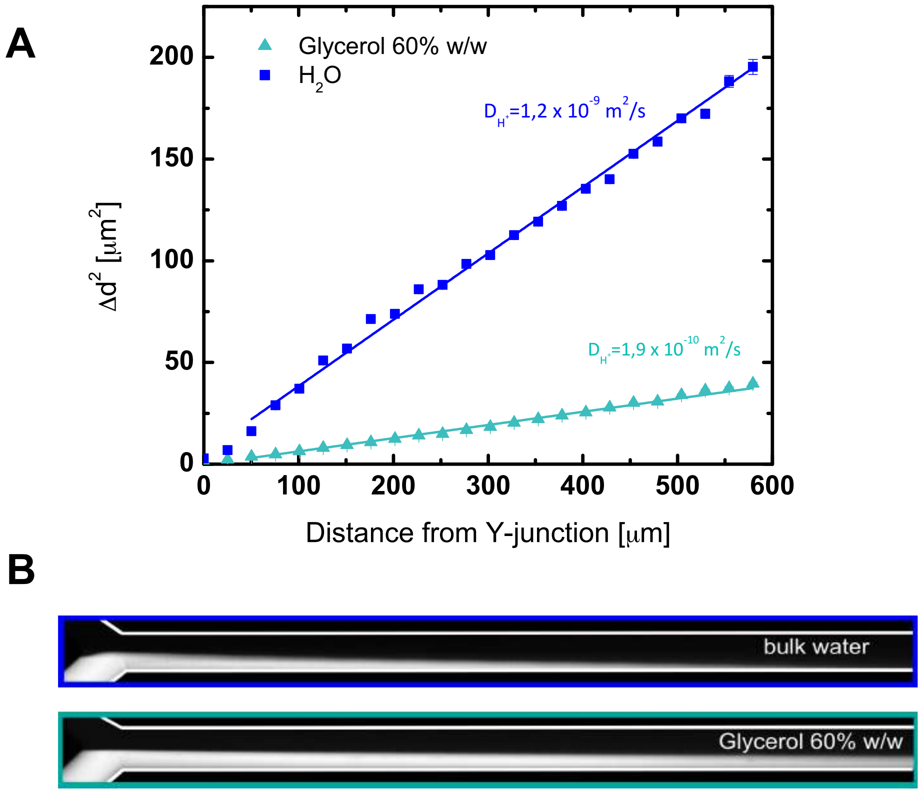

FIGURE 3.9: **Influence of macroscopic viscosity on proton mobility.** Proton diffusion in a viscous (10 mPas) 60 % w/w Glycerol solution was found to be 6-6.5× smaller than in bulk water.

3.4 Discussion

Combining a microfluidic fluorescence microscopy setup with time-resolved femtosecond IR spectroscopy we show that the physical proton transport properties are fundamentally changed in the presence of physiological concentrations of representative cytosolic components. To the best of our knowledge, no systematic investigation has yet been presented where proton mobility was assessed on the grounds of both cytosolic composition and the associated water reorientation dynamics. While the presented microfluidic setup allowed us to derive reasonable proton diffusion coefficients consistent with an ultrafast hopping mechanism in both bulk water and D_2O, we observed a 10 to 30-fold reduction in our cell mimicking solutions. At the same time, IR anisotropy measurements indicated only a small change in the water reorientation dynamics with a maximal slow water fraction of $\sim 20\%$ in the presence of high protein concentrations.

The discrepancy between fast proton movement in bulk water and slowed-down diffusion in cellular environments has been subject to extensive discussions on the underlying biophysical mechanism. In principle, there are two major explanation frameworks that keep recurring in these discussions: on the one hand, cytosolic buffers have been suggested to act on the local free proton concentrations. On the other hand, hindered water reorientation dynamics in the cell were likewise shown to slow down proton diffusion.

Role of cytosolic buffers

Buffers, which are essential for all living organisms and thus omnipresent in all types of cellular systems, have been known to act on cytoplasmic proton concentrations for a long time. Depending on their respective pK_a values they are key contributors to pH homoeostasis in cells. Generally, literature differentiates between mobile and immobile buffers, i.e. small molecules such as phosphate ($D \sim 10^{-10} m^2 s^{-1}$) versus macromolecules such as proteins ($D \sim 10^{-11} m^2 s^{-1}$). The majority of experimental data on proton movement kinetics in living systems are based on Junge and McLaughlin's theory [17]. According to them the effective proton diffusion coefficient is determined by Fick's second law and the relative concentration of mobile versus immobile buffers. This theory was continuously evolved by including respective buffer capacities [34] and absolute intracellular pH values [35]. Cytosolic buffers have on these grounds previously been shown capable of modulating intracellular H^+ mobility [19]. However, in all of the aforementioned theoretical and experimental studies on living cells water dynamics and the role of the Grotthus mechanism on proton diffusion are entirely omitted.

Role of water reorientation dynamics

In a similarly isolated fashion, water reorientation dynamics have repeatedly been shown to have a noticeable impact on proton mobility. The Grotthus mechanism depends to a considerable extent on the rearrangement of a large number (i.e. > 10) of water molecules in the surroundings of the diffusing proton [2]. In general, proton transport is enhanced, if water molecules can freely rotate in solution. This unhindered rotation can be impaired among others by the presence of hydrophobic moieties [28] or water cluster domains [21].

Generally speaking, any water (de-)structuring effect is expected to reflect back on the Grotthus mechanism. A higher order structure can result in a more concerted and thus faster proton hopping such as found in 'water wires' [36], but it can likewise also significantly impair water reorientation kinetics and with it proton mobility. Recent literature often discusses the notion of 'biowater' and its altered biophysical properties with respect to bulk water [27, 37, 38]. Experimental evidence for both proton diffusion enhancing and suppressing effects resulting from a change in the local water structure has been provided in the past years. For example, Pohl and co-workers observed proton diffusion coefficients higher than in bulk water in the hydration layer of certain water-ordering membranes [39]. In contrast, Mojumar et al. reported a 10 to 100-fold reduction of proton mobility in the cytoplasmic region close to a macromolecular host, which they ascribe to slower ion solvation dynamics, decreased numbers of free water molecules and perturbations of Grotthus-like chains [40].

Role of viscosity

An additional very interesting, but so far fairly omitted aspect is the role of viscosity on the proton diffusion coefficient. According to the classical Stokes-Einstein equation the diffusion coefficient of any particle is inversely proportional to the viscosity of the medium where it diffuses. We probed the effect of an increased viscosity (i.e. $10 \times \eta_{H_2O}$) on the proton diffusion coefficient in two different solutions: on the one hand, a pure 60 %w/w glycerol-water solution, on the other hand a cytosolic mimic solution with 30 %w/w of added proteins. Interestingly, the observed reduction of proton mobility in the glycerol-water solution is a factor of 2 higher than in the more complex CMS, even though their macroscopically measured viscosities are the same. Furthermore, in both cases the decrease of the proton mobility is not in line with particle diffusion: we observed a 6 to 6.5-fold reduction in the glycerol solution and a 3-fold reduction in the CMS + protein with respect to the non-viscous equivalent solution for which $\eta = \eta_{H_2O} \approx 1$ mPas. This experiment demonstrates, as predicted by Grotthus, that proton displacement does not obey a classical particle diffusion mechanism.

Another striking observation becomes apparent, if one includes the results from the cytosolic mimic solution without protein: we showed that the presence of buffers causes a tenfold reduction in proton mobility and explained this by a buffer-mediated proton diffusion mechanism, where the protons diffuse bound to buffers with a correspondingly 10× lower diffusion coefficient:

$$D_{H^+cytosol} \approx D_{buffer} \approx 0.1\,(D_{H^+Grotthus}) \tag{3.6}$$

On these grounds, the addition of proteins and the resulting 10× higher solution viscosity should lead to a 10-fold reduction of the buffer diffusion coefficient and hence an overall 100-fold reduction of the proton diffusion coefficient. However, the measured reduction is only 30-fold, which can be due to two different reasons: either the buffer molecules do just as protons not follow classical particle diffusion. Or, our notion of viscosity needs to be refined: the macroscopic viscosity value that we measured by rheometry does not reflect non-hydrodynamic friction and is thus only to a limited extent capable of accurately describing all forces acting on the molecular scale. 'Molecular' viscosity, in turn, largely depends on local water reorientation dynamics, electrostatic friction forces as well as relative solvent/solute ratios and therefore does not always correlate to predictions based on the classical continuum Stokes-Einstein diffusion equation [41]. As the water reorientation dynamics in the CMS + protein are barely slowed down, molecular viscosity in these samples is likely to be considerably lower than the macroscopically measured value. This would provide a more probable explanation for why the decrease in proton mobility is less drastic than expected from the macroscopic viscosity of this sample.

Other macromolecular effects

So far we have only discussed the presence of macromolecules with respect to the measurable increase in macromolecular viscosity and the potential change of the water dynamics of the solution. However, additional effects arising from the added proteins are possible: (i) proteins are macromolecules with titratable groups and can therefore be thought of as immobile buffers that compete with the smaller mobile buffers for proton binding [35]. Since protein diffusion coefficients are at least 2 orders of magnitude lower than the diffusion coefficient of free protons ($D_{protein} \sim 10^{-11} m^2 s^{-1}$), protein-bound protons can be regarded as quasi-immobilized. (ii) Moreover, macromolecules often provide binding sites for smaller molecules. For example, BSA has been found capable of binding $H_2PO_4{}^-$ and $HPO_4{}^{2-}$ [42] and may thereby entirely immobilize a fraction of the phosphate-bound protons, which would cause a further reduction in the proton diffusion coefficient. Alternatively, this might equally just reduce the effective concentration of active proton binding phosphate buffer molecules and lead to an increase of the fraction of free protons with a Grotthus-like fast diffusion coefficient.

.

Interplay of different factors

Interestingly, despite providing entirely different theoretical explanations, experimental studies on proton mobility suppression in biological systems reveal a similar decrease of the apparent cytoplasmic proton diffusion coefficient by 1-2 orders of magnitude [35, 40]. This is also consistent with our experiments in cell mimicking solutions. Our results primarily suggest a mobile buffer mediated proton transport mechanism that dominates over Grotthus-like proton hopping. However, a fully realistic description would include a multitude of factors such as the role of molecular viscosity and the buffer-binding capacity of the present macromolecules as described in the previous subsection. Last but not least, it is to be noted that water dynamics might play a more significant role in more complex, real cellular fluids that also contain lipids, mRNA etc., which would be interesting to investigate in future studies.

3.5 Conclusion

Taken together, we found that proton diffusion in cytosolic mimic solutions is at least an order of magnitude slower than in bulk water. At the same time, our results allow us to conclude that the Grotthus mechanism is unsuitable for satisfyingly describing proton diffusion dynamics in cell-like environments. Rather, our experiments point at the crucial role of buffers for the modulation of intracellular proton diffusion rates. Simultaneously, we observe a certain contribution from water dynamics as soon as macromolecules, e.g. proteins, come into play. Furthermore, macromolecules do not only act on the dynamical water structure and the solution viscosity, but may also provide binding sites for small mobile buffers whilst acting as immobile buffers themselves. The recently proposed existence of intracellular pH gradients constitutes thus not a contradiction to physical diffusion theory *per se*, but can reasonably be understood in terms of this multitude of additional effects that act on the proton mobility in both cellular and cell-like environments.

Bibliography

[1] C.J.T. Grotthuss. Sur la décomposition de l’eau et des corps qu’elle tient en dissolution à l’aide de l’électricité galvanique. *Ann. Chim.*, 58:54–73, 1806.

[2] K. J. Tielrooij, R. L. A. Timmer, H. J. Bakker, and M. Bonn. Structure Dynamics of the Proton in Liquid Water Probed with Terahertz Time-Domain Spectroscopy. *Physical Review Letters*, 102(19):198303, 2009.

[3] D. G. Isom, V. Sridharan, R. Baker, S. T. Clement, D. M. Smalley, and H. G. Dohlman. Protons as second messenger regulators of G protein signaling. *Mol Cell*, 51(4):531–8, 2013.

[4] B. P. Young, J. J. H. Shin, R. Orij, J. T. Chao, S. C. Li, X. L. Guan, A. Khong, E. Jan, M. R. Wenk, W. A. Prinz, G. J. Smits, and C. J. R. Loewen. Phosphatidic Acid Is a pH Biosensor That Links Membrane Biogenesis to Metabolism. *Science*, 329(5995):1085, 2010.

[5] R. Orij, S. Brul, and G. J. Smits. Intracellular pH is a tightly controlled signal in yeast. *Biochim Biophys Acta*, 1810(10):933–44, 2011.

[6] A. Schönichen, B. A. Webb, M. P. Jacobson, and D. L. Barber. Considering protonation as a posttranslational modification regulating protein structure and function. *Annu Rev Biophys*, 42:289–314, 2013.

[7] R. Orij, M. L. Urbanus, F. J. Vizeacoumar, G. Giaever, C. Boone, C. Nislow, S. Brul, and G. J. Smits. Genome-wide analysis of intracellular pH reveals quantitative control of cell division rate by pH(c) in Saccharomyces cerevisiae. *Genome Biol*, 13(9):R80, 2012.

[8] A. C. Certal, R. B. Almeida, L. M. Carvalho, E. Wong, N. Moreno, E. Michard, J. Carneiro, J. Rodriguéz-Léon, H.-M. Wu, A. Y. Cheung, and J. A. Feijó. Exclusion of a Proton ATPase from the Apical Membrane Is Associated with Cell Polarity and Tip Growth in Nicotiana tabacum Pollen Tubes. *The Plant Cell*, 20(3):614–634, 2008.

[9] K. Tarbashevich, M. Reichman-Fried, C. Grimaldi, and E. Raz. Chemokine-Dependent pH Elevation at the Cell Front Sustains Polarity in Directionally Migrating Zebrafish Germ Cells. *Current Biology*, 25(8):1096–1103.

[10] D. S. Adams, K. R. Robinson, T. Fukumoto, S. Yuan, R. C. Albertson, P. Yelick, L. Kuo, M. McSweeney, and M. Levin. Early, H^+-V-ATPase-dependent proton flux is necessary for consistent left-right patterning of non-mammalian vertebrates. *Development (Cambridge, England)*, 133(9):1657–1671, 2006.

[11] K. A. Henderson, A. L. Hughes, and D. E. Gottschling. Mother-daughter asymmetry of pH underlies aging and rejuvenation in yeast. *eLife*, 3:e03504, 2014.

[12] B. A. Webb, M. Chimenti, M. P. Jacobson, and D. L. Barber. Dysregulated pH: a perfect storm for cancer progression. *Nat Rev Cancer*, 11(9):671–7, 2011.

[13] R. Dechant and M. Peter. Cytosolic pH: A conserved regulator of cell growth? *Mol Cell Oncol*, 1(4):e969643, 2014.

[14] E. W. Sutherland and T. W. Rall. Fractionation and characterization of a cyclic adenine ribonucleotide formed by tissue particles. *J Biol Chem*, 232(2):1077–91, 1958.

[15] J. D. Bernal and R. H. Fowler. A Theory of Water and Ionic Solution, with Particular Reference to Hydrogen and Hydroxyl Ions. *The Journal of Chemical Physics*, 1(8):515–548, 1933.

[16] J. M. Swanson, C. M. Maupin, H. Chen, M. K. Petersen, J. Xu, Y. Wu, and G. A. Voth. Proton solvation and transport in aqueous and biomolecular systems: insights from computer simulations. *J Phys Chem B*, 111(17):4300–14, 2007.

[17] W. Junge and S. McLaughlin. The role of fixed and mobile buffers in the kinetics of proton movement. *Biochimica et Biophysica Acta (BBA) - Bioenergetics*, 890(1):1–5, 1987.

[18] A. Burykin and A. Warshel. What really prevents proton transport through aquaporin? Charge self-energy versus proton wire proposals. *Biophys J*, 85(6):3696–706, 2003.

[19] P. Swietach and R. D. Vaughan-Jones. Relationship between intracellular pH and proton mobility in rat and guinea-pig ventricular myocytes. *J Physiol*, 566(Pt 3):793–806, 2005.

[20] K. van Eunen, J. Bouwman, P. Daran-Lapujade, J. Postmus, A. B. Canelas, F. I. Mensonides, R. Orij, I. Tuzun, J. van den Brink, G. J. Smits, W. M. van Gulik, S. Brul, J. J. Heijnen, J. H. de Winde, M. J. de Mattos, C. Kettner, J. Nielsen, H. V. Westerhoff, and B. M. Bakker. Measuring enzyme activities under standardized in vivo-like conditions for systems biology. *FEBS J*, 277(3):749–60, 2010.

[21] D. Bonn, D. Ross, S. Hachem, S. Gridel, and J. Meunier. Percolation transition in Coulombic near-critical binary liquids? *EPL (Europhysics Letters)*, 58(1):74, 2002.

[22] L. Piatkowski, J. de Heij, and Huib J. Bakker. Probing the Distribution of Water Molecules Hydrating Lipid Membranes with Ultrafast Förster Vibrational Energy Transfer. *The Journal of Physical Chemistry B*, 117(5):1367–1377, 2013.

[23] C. C. M. Groot and H. J. Bakker. A femtosecond mid-infrared study of the dynamics of water in aqueous sugar solutions. *Physical Chemistry Chemical Physics*, 17(13):8449–8458, 2015.

[24] L. Szyc, M. Yang, and T. Elsaesser. Ultrafast Energy Exchange via Water-Phosphate Interactions in Hydrated DNA. *The Journal of Physical Chemistry B*, 114(23):7951–7957, 2010.

[25] Y. L. A. Rezus and H. J. Bakker. On the orientational relaxation of hdo in liquid water. *The Journal of Chemical Physics*, 123(11):114502, 2005.

[26] Y. L. A. Rezus and H. J. Bakker. Strong slowing down of water reorientation in mixtures of water and tetramethylurea. *The Journal of Physical Chemistry A*, 112(11):2355–2361, 2008. PMID: 18275169.

[27] C. A. Wraight. Chance and design - Proton transfer in water, channels and bioenergetic proteins. *Biochimica et Biophysica Acta (BBA) - Bioenergetics*, 1757(8):886–912, 2006.

[28] M. Bonn, H. J. Bakker, G. Rago, F. Pouzy, J. R. Siekierzycka, A. M. Brouwer, and D. Bonn. Suppression of Proton Mobility by Hydrophobic Hydration. *Journal of the American Chemical Society*, 131(47):17070–17071, 2009.

[29] N. Agmon. The Grotthuss mechanism. *Chemical Physics Letters*, 244(5-6):456–462, 1995.

[30] D. B. Spry, A. Goun, K. Glusac, D. E. Moilanen, and M. D. Fayer. Proton Transport and the Water Environment in Nafion Fuel Cell Membranes and AOT Reverse Micelles. *Journal of the American Chemical Society*, 129(26):8122–8130, 2007.

[31] K. Meister, S. Strazdaite, A. L. DeVries, S. Lotze, L. L. C. Olijve, I. K. Voets, and H. J. Bakker. Observation of ice-like water layers at an aqueous protein surface. *Proceedings of the National Academy of Sciences of the United States of America*, 111(50):17732–17736, 2014.

[32] J. Buffle, Z. Zhang, and K. Startchev. Metal Flux and Dynamic Speciation at (Bio)interfaces. Part I: Critical Evaluation and Compilation of Physicochemical Parameters for Complexes with Simple Ligands and Fulvic/Humic Substances. *Environmental Science & Technology*, 41(22):7609–7620, 2007.

[33] P. W. Atkins and Julio De Paula. *Atkins' Physical chemistry*. 2014.

[34] M. Irving, J. Maylie, N. L. Sizto, and W. K. Chandler. Intracellular diffusion in the presence of mobile buffers. Application to proton movement in muscle. *Biophys J*, 57(4):717–21, 1990.

[35] P. Swietach, K. W. Spitzer, and R. D. Vaughan-Jones. pH-Dependence of extrinsic and intrinsic H^+-ion mobility in the rat ventricular myocyte, investigated using flash photolysis of a caged H^+ compound. *Biophys J*, 92(2):641–53, 2007.

[36] M. J. Cox, R. L. A. Timmer, H. J. Bakker, S. Park, and N. Agmon. Distance-Dependent Proton Transfer along Water Wires Connecting Acid-Base Pairs. *The Journal of Physical Chemistry A*, 113(24):6599–6606, 2009.

[37] P. Jungwirth. Biological Water or Rather Water in Biology? *The Journal of Physical Chemistry Letters*, 6(13):2449–2451, 2015.

[38] G. Hummer and A. Tokmakoff. Preface: Special Topic on Biological Water. *The Journal of Chemical Physics*, 141(22):22D101, 2014.

[39] A. Springer, V. Hagen, D. A. Cherepanov, Y. N. Antonenko, and P. Pohl. Protons migrate along interfacial water without significant contributions from

jumps between ionizable groups on the membrane surface. *Proc Natl Acad Sci U S A*, 108(35):14461–6, 2011.

[40] S. Sen Mojumdar, R. Chowdhury, A. K. Mandal, and K. Bhattacharyya. In what time scale proton transfer takes place in a live CHO cell? *J Chem Phys*, 138(21):215102, 2013.

[41] M. L. Horng, J. A. Gardecki, and M. Maroncelli. Rotational Dynamics of Coumarin 153: Time-Dependent Friction, Dielectric Friction, and Other Nonhydrodynamic Effects. *The Journal of Physical Chemistry A*, 101(6):1030–1047, 1997.

[42] S. Bakkialakshmi, B. Shanthi, and D. Chandrakala. Interaction of Potassium Mono and Di Phosphates with Bovine Serum Albumin Studied by Fluorescence Quenching Method. *Journal of Fluorescence*, 21(2):687–692, 2011.

Chapter 4

The dynamic surface tension of water

4.1 Introduction

The surface tension of any liquid is positive, which can be understood from the fact that on average a molecule on the surface has less neighbours and hence less attractive van der Waals interactions than a molecule in the bulk. It therefore costs energy to create new surfaces and indeed, reasonable estimates of the surface tensions of apolar liquids can be obtained in this way [1]. For water, however, an analogous approach leads to a calculated surface tension that is roughly a factor of three smaller than the experimental one [1]. One usually attributes the high surface tension to missing hydrogen bonds at the surface, but it has turned out to be very difficult to calculate or simulate their contribution to the surface tension in both theory and simulations [2]. One test of the hydrogen bond argument would be to make use of the fact that the relaxation (reorientation) time of hydrogen bonds in the bulk is on the order of a few ps [3]. Hence, if the reorientation time scale at the interface is similar, one would expect any relaxation of the surface tension to take place on this time scale. Here we study the surface relaxation of water and find that water exhibits a dynamic surface tension with a relaxation time that is on the order of 1 ms or larger indicating that an essential ingredient is missing for understanding the value of the water surface tension.

We study the formation and breakup of droplets of water emanating from an orifice (Fig. 4.1). Drop formation has received much attention recently and it was shown that the breakup mechanism is universal for different liquids, meaning that the form of the breakup and its time dependence are uniquely determined by the forces acting on the liquid neck that separates the main drop from the

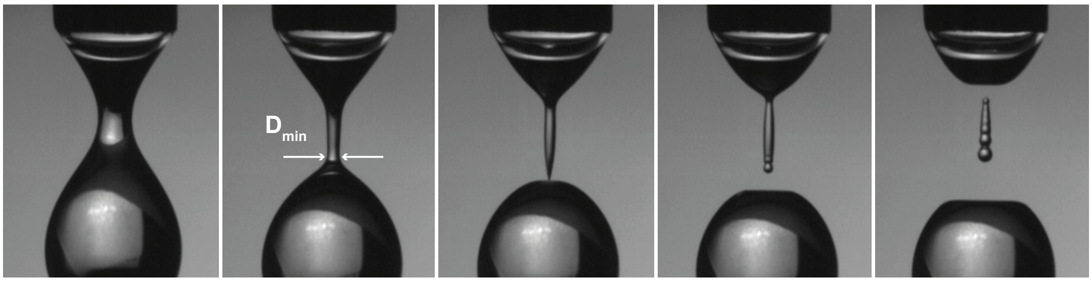

FIGURE 4.1: **Pinch-off images at subsequent stages of the droplet pinch-off process.** The minimum neck diameter is obtained from ultra-rapid camera movies (54.000 fps) and subsequent image analysis. Time to pinch-off is 5 ms, 1 ms, 0 ms, -0.5 ms and -1 ms (left to right). The experiments were performed with two different capillary sizes (240 µm and 2 mm). The drop size in the image is 2.25 mm.

orifice [4, 5]. For low-viscosity liquids such as water, only surface tension forces drive the breakup of the liquid neck while inertial forces slow it down. This leads to a dynamics characteristic of a singularity at finite time, in which the neck diameter goes to zero as:

$$D_{min} = A\left(\frac{\sigma}{\rho}\right)^{1/3}(t_0 - t)^{2/3} \tag{4.1}$$

where D_{min} is the width of the fluid neck at its minimum (Fig. 4.1), A is a numerical prefactor, σ is the surface tension, r the density and t$_0$ the breakup time. The $(t_0 - t)$ term, in the following referred to as τ, is characteristic of the finite time singularity that occurs at t_0, in which the deformation rate of the surface diverges. Consequently, if one knows the prefactor A, one can infer the surface tension from the drop formation dynamics in a situation where the breakup process creates freshly formed air-water interface at a diverging rate. The latter is easy to see from volume conservation: taking the liquid neck as a cylinder of height h, its constant volume is $\sim D_{min}^2 h$ so that $h \sim (t_0 - t)^{-4/3}$ and consequently the area $D_{min}h \sim (t_0 - t)^{-2/3}$ diverges at t_0.

4.2 Materials and Methods

4.2.1 Surface tension measurements

All examined simple liquids were purchased from Sigma Aldrich and their surface tension values verified using the pendant drop method (Krüss EasyDrop). Since the measured density and surface tension values showed a very good agreement with the literature values (± 0.5 %) they were used without further purification for the subsequent ultrarapid camera experiments.

4.2.2 Ultrarapid imaging of drop breakup

A 1 ml syringe with an internal diameter of 2 mm was used together with a syringe pump to create controlled drops at a constant flowrate of 0.5 mlh^{-1}. Using this setup we recorded movies of the fluid neck rupture using an ultrarapid camera with a frame rate of 54001 fps, an exposition time of 0.98 µs and a resolution of 224×180 pixels^2.

4.2.3 Derivation of breakup dynamics from movies

The recorded movies where binarized using the standard binarization tool in ImageJ. For each binarized movie frame at time to pinch-off τ the minimum neck diameter D_{min} was derived. The obtained $\tau - D_{min}$ data were linearized by plotting $D_{min}^{3/2}$ against τ. The universal prefactor A of the inviscid scaling law can be directly derived from the slope C of a linear fit to the data: $C = A^{3/2}(\sigma/\rho)^{1/2}$.

4.3 Results

4.3.1 Determination of the universal prefactor

Despite the fact that the prefactor A should be universal and therefore independent of any initial conditions or the nature of the inviscid fluid itself, there is considerable uncertainty in the literature [4, 5, 6, 7, 8, 9, 10, 11] as to what the value of A in eq. 4.1 should be. Most published experimental results were obtained from ultrarapid imaging and suggest prefactors of 0.9−1.1 [10], 1.1 [11] or 1.14−1.36 [12]. An alternative approach based on measuring the electrical conductance of the filament yielded a prefactor as low as 0.44 [8]. A similar disagreement appears in the associated numerical simulations, where values between 1.26 [11], 1.4 [10] and 1.46 [13] can be deduced from the presented drop breakup dynamics curves. In certain simulations the presented asymptotics even seem to display a time dependence that is wholly inconsistent with there being a universal asymptotic dynamics [10]. In addition, none of the existing experimental and numerical accounts explicitly give value for the prefactor. These remarkable discrepancies warrant an in-depth investigation of this fundamental hydrodynamics problem. This is, however, beyond the scope of the present paper and will be addressed in a separate study. In the present work we will first provide an unambiguous determination of the prefactor using different simple liquids and subsequently use the derived value for A as a reference for the determination of the water surface tension of a pristine water-air interface.

We follow the thinning dynamics using an ultra high-speed camera attached to a microscope to have both maximal temporal and spatial resolution. For liquids with different ratios σ/ρ, we arrive at good agreement with eq. 4.1 (Fig. 4.2A) with a value of the prefactor A of 0.9 ± 0.01 (Fig. 4.1B). For water, however, the identical experiment is not on the same line, and shows a systematic deviation. Previous experiments on the breakup of water, helium and mercury do not agree on the prefactor [7, 8, 9, 10]. The data of Chen et al., although noisier, appear to agree with our data at least close to the breakup point, but deviate for longer times and the helium and mercury experiments give very different prefactors. From numerics [10, 13], the prefactor was determined to be $A \sim 1.4$, which disagrees with most of the experiments. We therefore use the precise and universal prefactor obtained in our experiments on a series of other liquids of known surface tension. The surface tensions were verified independently on the liquids used in the snap-off experiments. Using this prefactor does not lead to the expected value of the surface tension of ~ 72 mNm^{-1}, but rather to a surprisingly high value of ~ 90 mNm^{-1}. This strongly suggests that the surface tension of a newly formed water surface on a time scale < 1 ms is different from the equilibrium surface tension, implying that some surface relaxation must take place.

This gives a bound on the characteristic time for the surface tension crossover ($\sim$ ms) that is very different from that of the relaxation of the bulk hydrogen bonds ($\sim$ ps). One possible mechanism that has been proposed and was suggested to lead to a similar time scale [1, 14] is the establishment of an equilibrium distribution of OH^- and H^+ ions close to the interface. The (uncontested) positive sign of the surface potential of water implies that its surface charge correspondingly carries a net negative sign in equilibrium and at neutral pH [15, 16, 17]. The usual interpretation of this is that, on average, the OH^- are closer to the surface than the H^+ ions, which implies the establishment of an OH^- 'adsorption' equilibrium at the surface [14]. However, at very low pH, the surface charge becomes positive due to the excess of H^+ present. [17, 18]. In principle, this could both account for the higher value of the dynamic surface tension at short times and the existence of the characteristic time: if the OH^- ions are depleted at early times, this would increase the surface tension, and the characteristic time is the time for establishing the adsorption equilibrium. In our case, the diffusion coefficient of OH^- ions is $\sim 10^{-9} m^2 s^{-1}$ [19], so that establishing the diffusion equilibrium over the typical diameter of the fluid neck of 1 µm takes $\sim$ 1 ms. In some molecular dynamics simulations [20], spectroscopic investigations [21], and studies on acid adsorption [22, 23, 24], it is suggested that H^+ adsorption may also occur at the water-air interface indicating that the underlying mechanism could be even more complex. We therefore now investigate the effect of pH.

4.3.2 Effect of pH

Such a dynamic surface tension is well known for surface-active agents and indeed, the same experiment as done here in the presence of surfactants shows that close to drop breakup, the surface tension is significantly higher than the equilibrium one, just as is observed here [25, 26]. If there is no adsorption barrier, the characteristic time follows from the adsorption dynamics as $\tau \sim \Gamma^2/Dc^2$, where Γ is the equilibrium adsorption, c the bulk concentration, and D the diffusion coefficient of the surface-active species. Characteristic times are also found to be on the order of $\sim$ 1 ms in surfactant adsorption experiments [27]. This suggests for our experiments that changing the bulk concentration c should have a strong influence on the relaxation time. In our experiment, we can easily change the bulk concentration of protons or hydronium ions by several orders of magnitude by adjusting the pH with either acid (HCl) or base (NaOH). However, the data show that neither of these additions changes the short-time value of the dynamic surface tension (Fig. 4.2A). From the simple argument given above one would have anticipated to retrieve the equilibrium surface tension upon addition of an excess of OH^-- ions (data at pH = 14, Fig. 4.2). A relaxation time independent of the bulk concentration can be obtained if there is an adsorption barrier at the surface that is the rate-limiting step for the arrival of molecules from the bulk onto the surface. This is for instance frequently encountered for charged surfactants [28], where the charged surfactants at the surface constitute an electrostatic barrier for

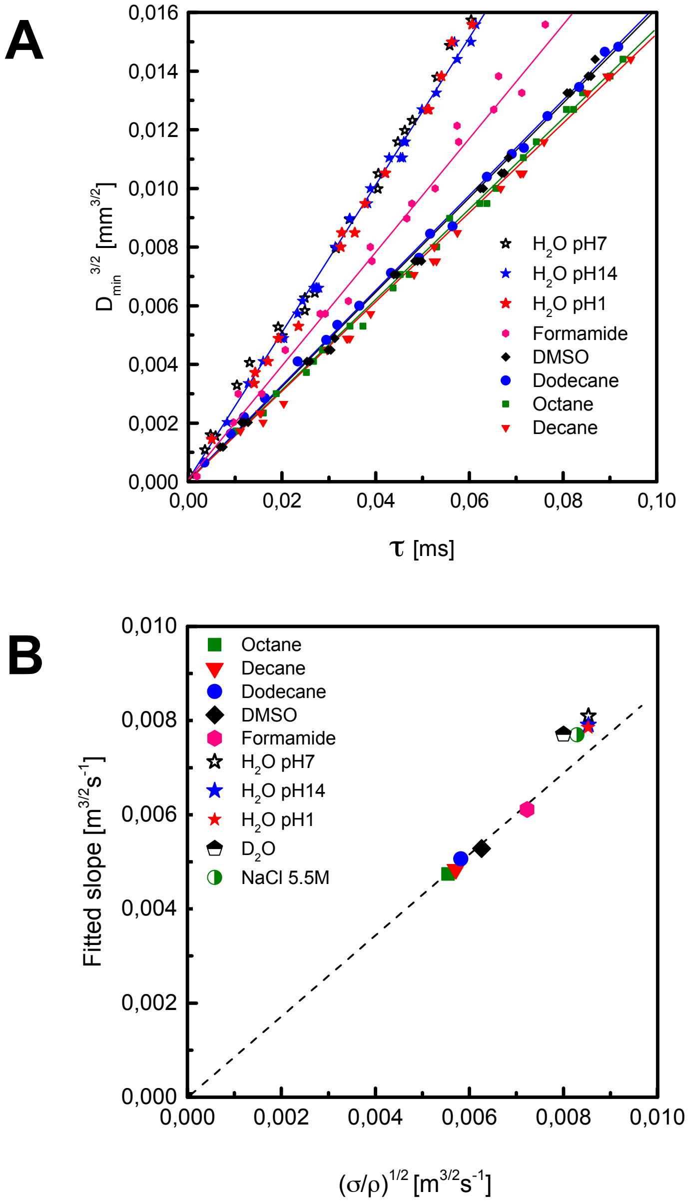

FIGURE 4.2: **Determination of the prefactor in eq. 4.1.** A: Linear fits of ultra-rapid camera imaging data to the capillary-inertial law for inviscid fluids ($D_{min} \propto A\tau^{2/3}$). By plotting the data in this way a stringent test is obtained for the applicability of the scaling. The slope C of the fitted lines can then be used to determine the prefactor A. B: By plotting the slopes obtained from (A) versus $(\sigma/\rho)^{1/2}$ we derive a prefactor A = 0.9 ± 0.01 (slope $C = A^{3/2}(\sigma/\rho)^{1/2}$). Water, D_2O and sodium chloride solution show a significant deviation from the theoretical prediction and are thus not taken into consideration for the calculation of the universal prefactor. The presented data were obtained using a capillary of 240 µm diameter.

the adsorption of further charged molecules. In our case though, if the barrier is electrostatic, one would again expect a large decrease of the characteristic time upon changing the pH, since the characteristic time in this case is $\tau \sim \kappa^2/D$ [28], with κ the Debye length that varies with the amount of electrolyte added. Thus, the data would only be consistent with the existence of an adsorption energy barrier that comes from a different origin. However, what the physical mechanism would be is unclear.

4.3.3 Effect of salt concentration

A related check of the ionic redistribution explanation is to see whether there is a characteristic time for the depletion of certain species from the interface. The obvious approach for studying dynamic depletion effects is to study salt solutions. Salts are strongly depleted from the aqueous interface which in equilibrium increases the surface tension close to the values that are found here for the dynamic tension. In addition, large amounts of salt strongly screen any electrostatic interaction between the surface and the bulk and should therefore prevent adsorption of any charged moieties. Surprisingly, we could not detect any effect of the salt concentration on the surface relaxation behaviour on short time scales (Fig. 4.3B). The various salt solutions (Fig. 4.3A) again behave very similarly to water with a similarly high prefactor compared to the simple liquids.

4.4 Discussion & Conclusion

Our ultra-rapid camera experiments on droplet formation and breakup of different pure liquids therefore provide strong evidence for the existence of a high dynamic surface tension for water and various aqueous solutions on a $\sim$ ms time scale. In the past, higher than equilibrium surface tension values for water have been reported on short time scales. However, they have all remained highly controversial due to methodological and analytical shortcomings. As early as 1926, Schmidt and Steyer reported elevated values of $80-100$ mNm^{-1} for the surface tension of freshly formed water/air interfaces, that would relax to the equilibrium value within roughly 1 ms [29]. Critics nevertheless stated that a viscosity effect in the constricted quartz capillary rather than the actual dynamic surface tension is measured by the falling meniscus method they employed [30]. A few years later, an improved technique, the 'bell method', yielded similar results, which, nevertheless, remained equally dubious due to the ambiguity related to

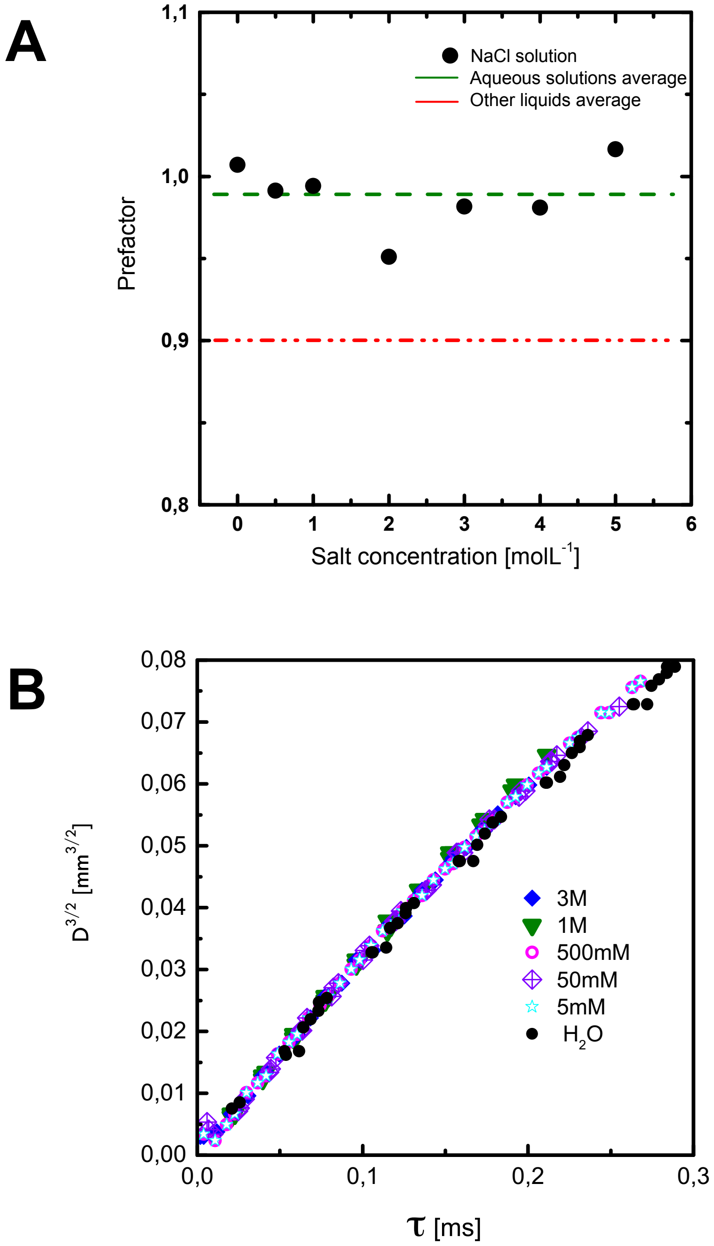

FIGURE 4.3: **Effect of salt.** A: Apparent prefactors obtained from pinch-off experiments. The derived prefactor appears to be independent of the salt concentration. B: Pinch-off dynamics of aqueous solutions at early times. Water and brine display an almost identical surface relaxation mechanism with surface tension values of 90 mNm^{-1} for the pristine interface. The data overlap since the increase in surface tension induced by the addition of salt is similar to the increase in density.

the exact determination of the surface age [14, 31]. Another very interesting account was presented by Eisenmenger and co-workers [32]. They excited Faraday waves on water surfaces and the frequency of these standing waves can be related to the surface tension. From the frequency dependence, they found that for large amplitudes of the Faraday waves the apparent surface tension of water was found to be elevated by $\sim$ 12 %, not dissimilar to the results presented here. It is unclear, though, how the non-linearity of the large-amplitude Faraday waves affects these values, and consequently whether it can really directly be understood as a surface tension. Interestingly, the authors interpreted their results as a strong indication for the presence of a surface viscosity, the existence of which, however, remains controversial to the present day [33, 34]. Finally, Kochura and Rusanov measured both the surface tension and the surface potential of water with the oscillating and the smooth jet method respectively [14]. These two independent techniques likewise suggested a dynamic water surface tension with initial values considerably above the equilibrium value and a similar relaxation time of $\sim$ 0.5 ms. However again, the suitability of the oscillating jet method for determining the surface tension of pristine surfaces on a sub-millisecond time scale has remained controversial: the associated hydrodynamics are incompletely understood which, in turn, entails considerable uncertainties in the complex analysis procedure [35]. In contrast to the above-mentioned methodologies, our method of studying droplet breakup dispenses with the experimental shortcomings and analytical ambiguity. The experimental procedure is very robust and the associated pinch-off dynamics is very well understood for inviscid fluids.

Taken together, we were able to unambiguously relate the drop breakup dynamics to the surface tension of a wide variety of pure liquids with the exception of pure, heavy and salty water. For aqueous systems, a considerable and systematic deviation was found. The origin of the slow surface relaxation process, which a dynamic surface tension implies, remains, however, incompletely understood. Various theories have been proposed in the past to account for this phenomenon. A much-discussed idea [18, 36, 37, 38] is that ion adsorption processes in the first fraction of a millisecond after surface creation are directly responsible for the observed high surface tension. We have shown here that for pure water this indeed gives the correct order of magnitude. Yet our detailed measurements also show that the high surface tension is observed irrespective of salt and OH^-/H^+ concentration levels. This is only possible if bulk diffusion or an electrostatic energy barrier at the surface are not the rate-limiting steps for

OH^- adsorption. An alternative and rather straightforward argument goes that the observed surface tension relaxation is merely due to traces of contaminant surfactants that are in practice very hard to avoid. However, it has been shown in both theory [39] and experiments [25, 26] that in drop breakup experiments the diverging rate of surface formation makes the adsorption or even presence of surfactants irrelevant, at least close to breakup. Further, these contaminants can only reduce the surface tension. In addition, the characteristic time for adsorption of surfactants at low concentrations lies in the range of several ms and should be even higher for very small contaminant concentrations [40] which again shows that impurities should be irrelevant on our sub-ms time scale.

Another possible explanation, perhaps related to the collective nature of the dipole fluctuations, would be a slow reorientation dynamics near the surface. In bulk, dielectric relaxation is known to occur on a much, much faster time scale ($\sim$ ps) [3]. Although it has been argued that close to surfaces the relaxation might be one or two orders of magnitude slower [41, 42] this is still a very a long way from the observed characteristic relaxation time of ~ 1 ms, even if one takes into account the possibility of a higher order water structure close to the surface [14]. On the other hand, it also seems unlikely that the observed deviations for water and the various aqueous solutions are due to hydrodynamic effects. For instance, flows have been shown to dampen out the capillary wave fluctuations of the surface and hence to increase the tension [43]. However, if such an effect is present here, it would happen at nanometer length and ps or ns time scales, and would hence not be observable in our experiment [43]. More importantly, it would also occur for the other liquids tested here, which have similar viscosities, surface tensions and densities.

In conclusion, we are at present unable to offer a complete explanation for our results. In spite of this, the implications are rather large: the observed high dynamic tension should for instance be relevant for spray formation, jet destabilization, drop impact and drop formation as all of these processes involve very short time scale surface dynamics.

Bibliography

[1] J. Lyklema. *Fundamentals of Interface and Colloid Science*, volume 3. Academic Press, London, 1995.

[2] Y. Nagata, T. Ohto, M. Bonn, and T. D. Kühne. Surface tension of ab initio liquid water at the water-air interface. *The Journal of Chemical Physics*, 144(20):204705, 2016.

[3] D. Laage and J. T. Hynes. On the Molecular Mechanism of Water Reorientation. *The Journal of Physical Chemistry B*, 112(45):14230–14242, 2008.

[4] J. Eggers. Nonlinear dynamics and breakup of free-surface flows. *Reviews of Modern Physics*, 69(3):865–930, 1997.

[5] J. Eggers and E. Villermaux. Physics of liquid jets. *Reports on Progress in Physics*, 71(3):036601, 2008.

[6] C. Wagner, Y. Amarouchene, D. Bonn, and J. Eggers. Droplet Detachment and Satellite Bead Formation in Viscoelastic Fluids. *Physical Review Letters*, 95(16):164504, 2005.

[7] J. C. Burton, J. E. Rutledge, and P. Taborek. Fluid pinch-off in superfluid and normal $^4\mathrm{He}$. *Physical Review E*, 75(3):036311, 2007.

[8] J. C. Burton, J. E. Rutledge, and P. Taborek. Fluid Pinch-Off Dynamics at Nanometer Length Scales. *Physical Review Letters*, 92(24):244505, 2004.

[9] J. C. Burton. *PhD Thesis*. Thesis, 2006.

[10] A. U. Chen, P. K. Notz, and O. A. Basaran. Computational and Experimental Analysis of Pinch-Off and Scaling. *Physical Review Letters*, 88(17):174501, 2002.

[11] M. P. Brenner, J. Eggers, K. Joseph, S. R. Nagel, and X. D. Shi. Breakdown of scaling in droplet fission at high Reynolds number. *Physics of Fluids*, 9(6):1573–1590, 1997.

[12] J. R. Castrejón-Pita, A. A. Castrejón-Pita, E. J. Hinch, J. R. Lister, and I. M. Hutchings. Self-similar breakup of near-inviscid liquids. *Physical Review E*, 86(1):015301, 2012.

[13] R. F. Day, E. J. Hinch, and J. R. Lister. Self-Similar Capillary Pinchoff of an Inviscid Fluid. *Physical Review Letters*, 80(4):704–707, 1998.

[14] M. Liu, J. K. Beattie, and A. Gray-Weale. The surface relaxation of water. *J Phys Chem B*, 116(30):8981–8, 2012.

[15] J. R. Farrell and P. McTigue. Precise compensating potential difference measurements with a voltaic cell. *Journal of Electroanalytical Chemistry and Interfacial Electrochemistry*, 139(1):37–56, 1982.

[16] N. N. Kochurova and A. I. Rusanov. Dynamic surface properties of water: Surface tension and surface potential. *Journal of Colloid and Interface Science*, 81(2):297–303, 1981.

[17] R. Zimmermann, U. Freudenberg, R. Schweiß, D. Küttner, and C. Werner. Hydroxide and hydronium ion adsorption - A survey. *Current Opinion in Colloid & Interface Science*, 15(3):196–202, 2010.

[18] J. K. Beattie, A. M. Djerdjev, and G. G. Warr. The surface of neat water is basic. *Faraday Discussions*, 141(0):31–39, 2009.

[19] J. Buffle, Z. Zhang, and K. Startchev. Metal Flux and Dynamic Speciation at (Bio)interfaces. Part I: Critical Evaluation and Compilation of Physicochemical Parameters for Complexes with Simple Ligands and Fulvic/Humic Substances. *Environmental Science & Technology*, 41(22):7609–7620, 2007.

[20] R. Vácha, D. Horinek, M. L. Berkowitz, and P. Jungwirth. Hydronium and hydroxide at the interface between water and hydrophobic media. *Physical Chemistry Chemical Physics*, 10(32):4975–4980, 2008.

[21] V. Buch, A. Milet, R. Vácha, P. Jungwirth, and J. P. Devlin. Water surface is acidic. *Proceedings of the National Academy of Sciences of the United States of America*, 104(18):7342–7347, 2007.

[22] A.P. dos Santos and Y. Levin. Surface tensions and surface potentials of acid solutions. *The Journal of Chemical Physics*, 133(15):154107, 2010.

[23] J. E. B. Randles and D. J. Schiffrin. Surface tension of dilute acid solutions. *Transactions of the Faraday Society*, 62(0):2403–2408, 1966.

[24] P. K. Weissenborn and R. J. Pugh. Surface Tension of Aqueous Solutions of Electrolytes: Relationship with Ion Hydration, Oxygen Solubility, and Bubble Coalescence. *Journal of Colloid and Interface Science*, 184(2):550–563, 1996.

[25] M. Roche, M. Aytouna, D. Bonn, and H. Kellay. Effect of Surface Tension Variations on the Pinch-Off Behavior of Small Fluid Drops in the Presence of Surfactants. *Physical Review Letters*, 103(26), 2009.

[26] M. R. D. Saint Vincent, J. Petit, M. Aytouna, J. P. Delville, D. Bonn, and H. Kelly. Dynamic interfacial tension effects in the rupture of liquid necks. *Journal of Fluid Mechanics*, 692:499–510, 2012.

[27] M. Aytouna, D. Bartolo, G. Wegdam, D. Bonn, and S. Rafajjï. Impact dynamics of surfactant laden drops: dynamic surface tension effects. *Experiments in Fluids*, 48(1):49–57, 2010.

[28] H. Diamant and D. Andelman. Kinetics of Surfactant Adsorption at Fluid-Fluid Interfaces. *The Journal of Physical Chemistry*, 100(32):13732–13742, 1996.

[29] F. Schmidt and H. Steyer. Neue Untersuchungen über die zeitliche Änderung der Spannung reiner Wasseroberflächen. *Annalen der Physik*, 384(5):442–464, 1926.

[30] R. Defay and J. R. Hommelen. I. Measurement of dynamic surface tensions of aqueous solutions by the oscillating jet method. *Journal of Colloid Science*, 13(6):553–564, 1958.

[31] P. P. Wegener and J.-Y. Parlange. Surface Tension of Liquids from Water Bell Experiments. *Zeitschrift für Physikalische Chemie*, 43:245, 1964.

[32] W. Eisenmenger. Dynamic properties of the surface tension of water and aqueous solutions of surface active agents with standing capillary waves in the frequency range from 10 kc/s to 1.5 Mc/s. *Acta Acustica united with Acustica*, 9(4):327–340, 1959.

[33] J. C. Earnshaw. Surface viscosity of water. *Nature*, 292(5819):138–139, 1981.

[34] M. A. Vila, V. A. Kuz, and A. E. Rodríguez. Surface viscosity of pure liquids. *Journal of Colloid and Interface Science*, 107(2):314–321, 1985.

[35] E. I. Franses, O. A. Basaran, and C.-H. Chang. Techniques to measure dynamic surface tension. *Current Opinion in Colloid & Interface Science*, 1(2):296–303, 1996.

[36] J. K. Beattie and A. M. Djerdjev. The pristine oil/water interface: surfactant-free hydroxide-charged emulsions. *Angew Chem Int Ed Engl*, 43(27):3568–71, 2004.

[37] B. Winter, M. Faubel, R. Vácha, and P. Jungwirth. Behavior of hydroxide at the water/vapor interface. *Chemical Physics Letters*, 474(4-6):241–247, 2009.

[38] P. B. Petersen and R. J. Saykally. Is the liquid water surface basic or acidic? Macroscopic vs. molecular-scale investigations. *Chemical Physics Letters*, 458(4-6):255–261, 2008.

[39] R. V. Craster, O. K. Matar, and D. T. Papageorgiou. Breakup of surfactant-laden jets above the critical micelle concentration. *Journal of Fluid Mechanics*, 629:195–219, 2009.

[40] N.N. Kochurova and A.I. Rusanov. Relaxation of the surface properties of aqueous solutions of surfactants and the mechanism of adsorption. *Russian Chemical Reviews*, 62(12):1083, 1993.

[41] A. Striolo. From Interfacial Water to Macroscopic Observables: A Review. *Adsorption Science & Technology*, 29(3):211–258, 2011.

[42] S. Balasubramanian, S. Pal, and B. Bagchi. Hydrogen-Bond Dynamics near a Micellar Surface: Origin of the Universal Slow Relaxation at Complex Aqueous Interfaces. *Physical Review Letters*, 89(11):115505, 2002.

[43] D. Derks, D. G. A. L. Aarts, D. Bonn, H. N. W. Lekkerkerker, and A. Imhof. Suppression of Thermally Excited Capillary Waves by Shear Flow. *Physical Review Letters*, 97(3):038301, 2006.

Chapter 5

Drop breakup dynamics on the nanosecond time scale

5.1 Introduction

In the previous chapter, we have studied the pinch-off dynamics of various inviscid liquids, where the minimum neck diameter d_{min} of the thinning filament is generally believed to be related to the time until the pinch-off point τ by a $2/3-$power law and a proportionality constant A:

$$d_{min} = A\left(\frac{\sigma}{\rho}\right)^{1/3}\tau^{2/3} \tag{5.1}$$

Our results strongly suggested that this prefactor A adopts a universal value of 0.9 for all inviscid liquids with the exception of water and aqueous solutions, which we attributed to the existence of a dynamic surface tension that presumably relaxes on a millisecond time scale. Nevertheless, these results are not consistent with numerical simulations that propose higher values of 1.26 [1], 1.4 [2] and 1.46 [3] respectively.

A possible reason for this considerable discrepancy is the fact that experimental data are usually acquired on a microsecond time scale using ultrarapid cameras, whereas most of the existing numerical simulations are situated around a region that is only a few nanoseconds away from the breakup point. A closer experimental approximation to the pinch-off point is not only constrained by the limits of optical instrumentation (e.g. the framerate), but also by the re-entrant profile that forms at times very close to the singularity (Fig. 5.1): the fluid filament remains attached to the droplet at a point below the horizon, which makes

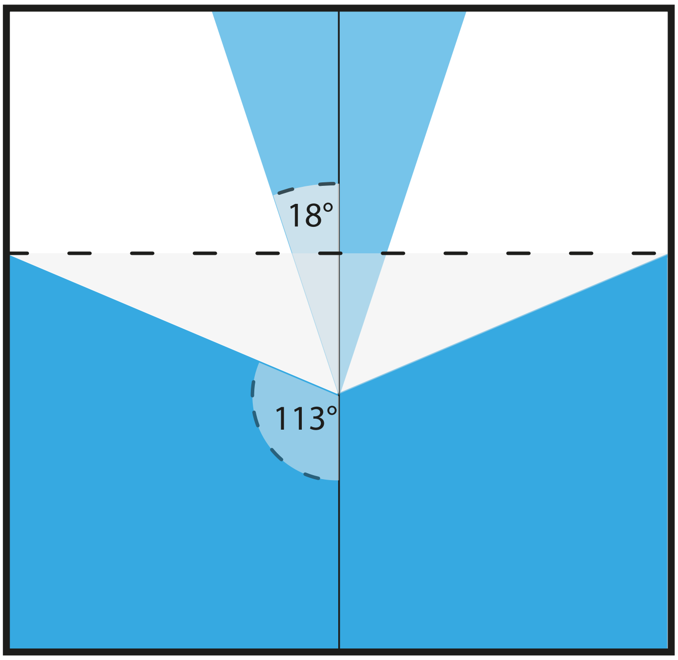

FIGURE 5.1: **Schematic sketch of a re-entrant drop profile (cross-sectional view)**. The view on the singularity is obscured by the optical horizon (dashed line). The corresponding angles are 18° and 112.8° respectively as indicated by both experiments and simulations [4, 3].

it impossible to derive a minimum neck diameter through optical image analysis. This limits the range of observable length and time scales to the order of µm and µs respectively and leaves a yet unexplored gap between numerical simulations and experiments for neck diameters above the viscous length scale $l_v < d_{min} <$ 1 µm.

This region is, however, particularly interesting from a theoretical point of view. Several authors have provided numerical evidence that the inviscid equations suffer from an intrinsic failure to asymptotically approach the pinch-off point. According to them, viscous stresses become important for $d_{min} >> l_v$, i.e. long before the viscous length scale is reached, which they explain by the formation of singularities before the neck diameter reaches zero [2, 5]. Eggers and Dupont, for example, suggested an alternative set of self-consistent equations, where they incorporated a finite amount of viscosity, which prevented the formation of other singularities before the pinch-off point. Yet their simulation implied that there is no overturning of the drop profile, which is clearly at odds with existing experimental evidence [4, 2]. Moreover, the addition of even a small amount of viscosity drastically changes the shape of the interface near the pinch-off region, since the value of the maximal drop curvature is primarily determined by viscous stresses.

Burton et al. have recently presented a promising alternative method that circumvents these optical limitations by recurring on electrical resistance measurements instead [6]. The authors claim that the instant of neck rupture can thereby be approached on the time scale of a few nanoseconds, which corresponds to nanometric fluid neck diameters. The latter are derived from the output voltage of a simple voltage divider circuit using a straightforward truncated cone resistor model [7] (c.f. 5.2). They prove the feasibility of their approach by providing experimental data on the pinch-off of mercury, one of the few inviscid liquids that possesses a sufficiently high conductivity to suit this method. Their results suggest - in contrast to abovementioned theoretical predictions - that the inviscid scaling equations remain valid for neck diameters as small as 5 nm. The associated prefactor for the minimum neck diameter is A $\sim$ 0.2, which is, in turn, neither consistent with our experimental results nor with any of the existing simulations (Fig. 5.2A).

Burton's data hint at a methodological flaw as the recorded output signal shows a significant ringing in the region around the pinch-off point, which - according to his argumentation - should coincide with the instant, where the recorded voltage signal abruptly goes to zero ($\tau = 0$ in Fig. 5.2B). This put us into doubt about the validity of this electrical method. We therefore repeated his electrical measurements and coupled them to a rapid camera in order to simultaneously observe the break-up of mercury on longer ($\sim$ µs) and shorter ($\sim$ ns) time scales. We repeated these experiments with supercooled liquid gallium, which has a sufficiently high conductivity to suit the electrical measurements and which, in principle, should fall under the inviscid pinch-off regime.

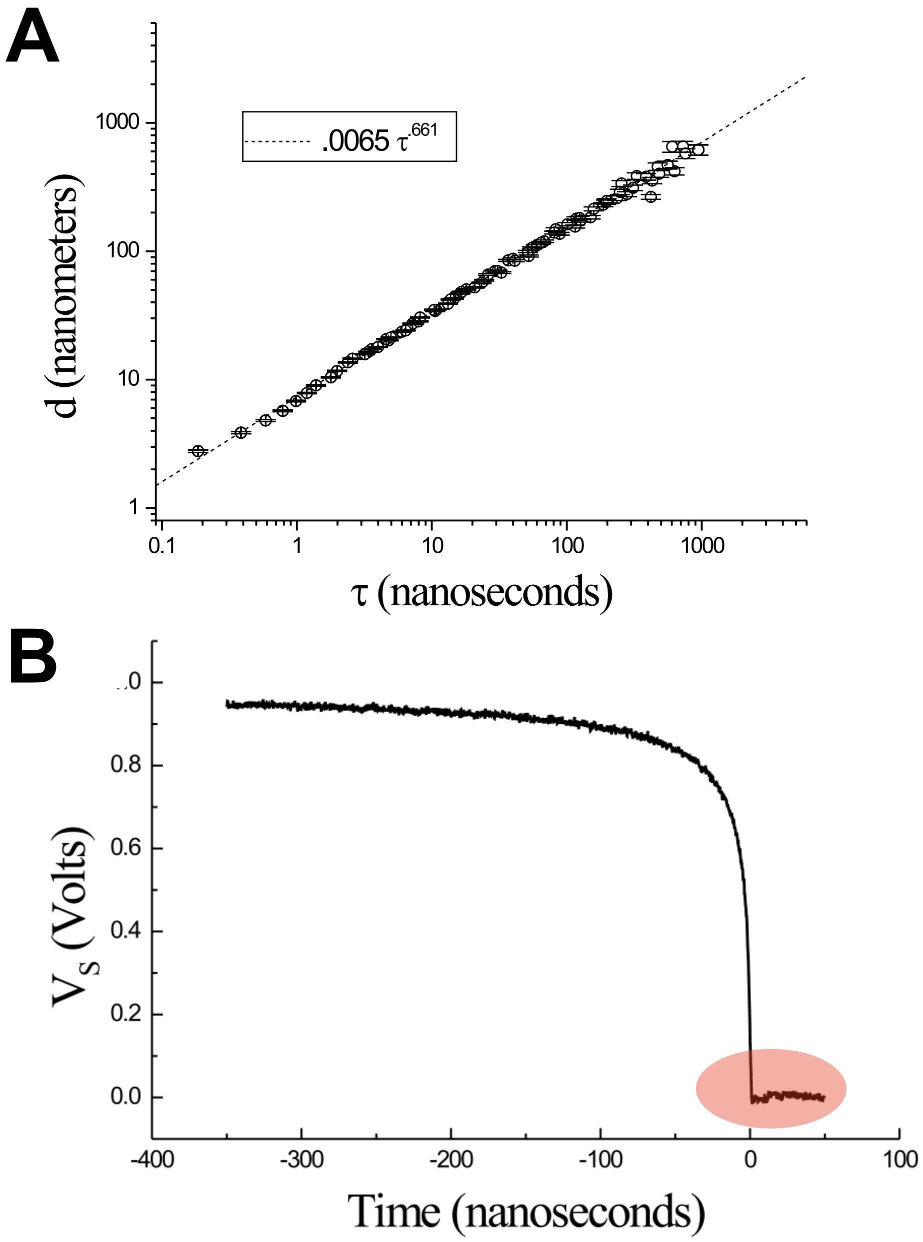

FIGURE 5.2: **Experimental data presented by Burton and coworkers**. A: The presented fit for the prefactor suggests $A \sim 0.2$. B: The $V - t$ data show a prominent ringing of the electrical signal in close proximity to the breakup point where $\tau = 0$. Analysis of these data yields a prefactor of $A \sim 0.45$ (cf. 5.3.1) [6].

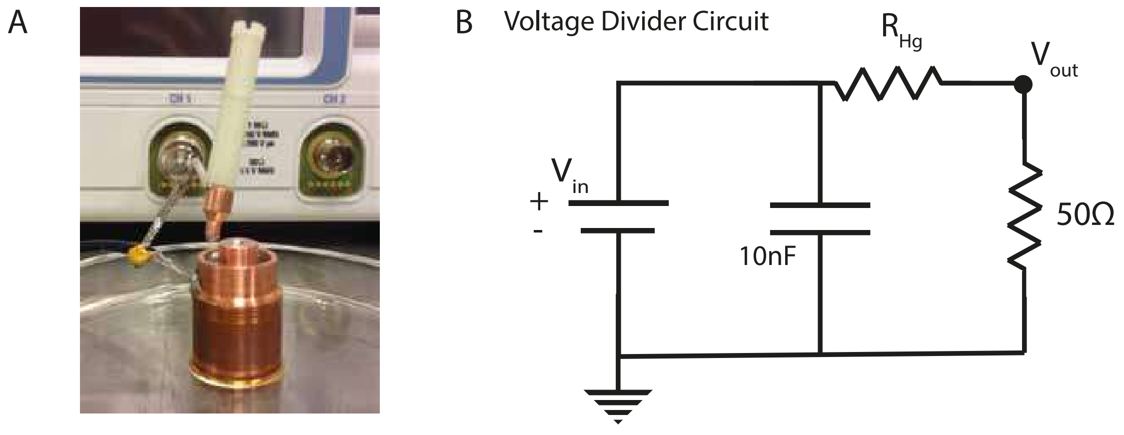

FIGURE 5.3: **Electrical setup *('Setup B')*.** A: Conductive copper electrode + reservoir B: Voltage divider circuit

5.2 Materials and Methods

5.2.1 Electrical measurements

We measured the resistance of the thinning mercury neck with an electrical circuit analogous to the voltage biased voltage divider presented by Burton and co-workers [6] (Fig. 5.3). The input resistance of our oscilloscope (RTO 1024, Rohde and Schwarz) served as 50 Ω resistor in our divider circuit.

Comparability with Burton's measurements was ensured by limiting the maximum bandwidth of our 2 GHz oscilloscope to 1 GHz with a sampling rate of 10 $\times$ 10^9 samples s^{-1}. The corresponding high frequency response was evaluated by approaching the two copper electrodes in the absence of mercury, which gave a step function with a rise time of 300 ps for 1 GHz. In order to obtain high quality data on the very short examined time and length scales, the high frequency response had to be simplified as much as possible. Therefore, the effective cable length was minimized to 10 cm by integrating the copper electrodes into a BNC connector with direct contact to the input of the scope. Since it is crucial for this experiment to keep the voltage bias V_{in} constant as the resistance of mercury R_{Hg} rises, a large capacitor of 10 nF was added to the upper copper electrode.

Prior to the measurements, the mercury surface was cleaned with concentrated sulphuric acid (H_2SO_4) which dissolves the superficial layer of mercury oxide that forms rather rapidly upon exposure to air. A contaminated surface appears grey-opaque, while a cleaned, unoxidized surface is silver and shiny. An ultra-clean tissue that does not bind pure mercury was used to carefully remove the residuals of the acid. In addition, the lower copper electrode was engineered as 'reservoir': after each pinch-off measurement a new mercury-air interface was formed by capillarity, which further minimized the extent of surface oxidation.

For the actual experiments mercury with a purity of 99.99 % was used and placed between the two conducting copper electrodes. For each measurement, we started from a closed circuit sustained by an intact mercury bridge and initiated the pinch-off by axial retraction of the upper rod-shaped copper electrode. The resistance of the mercury filament increases as its diameter shrinks and as soon as the recorded output voltage had fallen to zero, the oscilloscope triggered a time-synchronized ultra-rapid camera (Phantom Miro M310, Vision Research). The alignment of the trigger input of the camera with the zeroth frame of the electrical recording had been verified by the help of an LED prior to the actual measurements. All experiments were conducted at 20°C and different input voltages of 1 V, 3 V and 5 V were tested in independent runs.

5.2.2 Data analysis

The recorded oscilloscope data represent the output voltage V_s of the voltage divider circuit (Fig. 5.3) that decreases as the fluid neck becomes smaller. The corresponding resistance R_{Hg} of the thinning mercury filament can be derived from the ratio of the applied input voltage V_{in} over this output voltage and the resistance of the oscilloscope (R_s = 50 Ω):

$$R_{Hg} = R_S \left(\frac{V_{in}}{V_s} - 1 \right) \tag{5.2}$$

It has been shown in both experiments and simulations that an inviscid fluid filament adopts a conical shape close to the singularity of the breakup process (Fig. 5.1). The electrical resistance R of the filament is primarily determined by this cone region and can be calculated via the relation: $\vec{J} = \vec{E}\rho$ where $\vec{J}$ is the current density, $\vec{E}$ the electrical field and ρ the electrical resistivity. For a 'truncated cone' geometry with spherical caps of radius a and b the resistance can be approximated as a stack of slabs with thickness dx. The electrical potential is constant for each of these slabs perpendicular to the cone axis (Fig. 5.4):

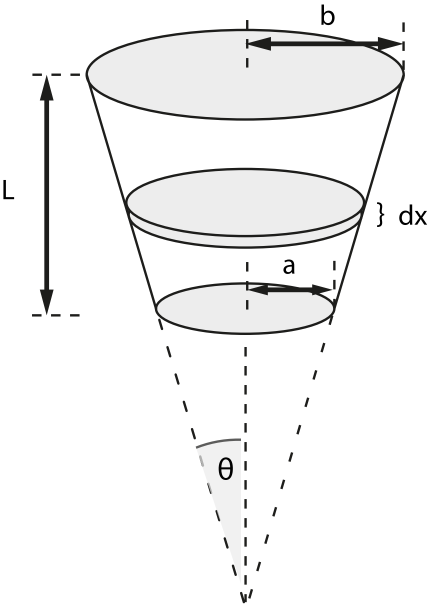

FIGURE 5.4: **Truncated cone resistor model used for data analysis.**

$$R = \int dR = \rho \frac{L}{b-a} \int_a^b \frac{dr}{\pi r^2} = \frac{\rho L}{\pi ab} \tag{5.3}$$

where L is the length of the truncated cone and r the cone radius of an individual slab [7].

For $a << b$ and a constant cone angle $\Theta = const.$ the resistance becomes independent of the filament length and is only determined by the inverse of the minimum neck diameter $2a = d$:

$$R = \frac{2\rho_r \cot\theta}{\pi d} \tag{5.4}$$

According to the theory of inviscid fluid breakup, the shape of the fluid cone is self-similar close to the pinch-off region and therefore Θ can assumed to be constant with a universal value of $\sim 18°$.

5.2.3 MATLAB simulations

The theoretical $V - \tau$ curve was modelled based on the inviscid scaling equation. For each time to pinch-off τ the theoretical neck diameter d was calculated (σ_{Hg}= 0.486 mNm^{-1}, ρ_{Hg}= 13.53 gcm^{-3}) and used as input for equation 5.4 which gave the resistance of the mercury filament R_{Hg} at time τ assuming a mercury resistivity of ρ_{Hg}= 9.6 $\times 10^{-7}\Omega$m and a cone angle Θ = 18°. From this resistance the theoretical oscilloscope output voltage V_s was obtained via equation 5.2. For the universal prefactor A we iteratively chose a value that minimized the deviation of the predicted $V - \tau$ curve from the actual data. This simple model, however, could not fully reconstruct our data, so further modifications to the model had to be incorporated. We will discuss these modifications and their implications in the results section. An exemplary MATLAB source code for the simulation of the 1 V measurement curve is provided in appendix A.[1]

5.3 Results

5.3.1 Breakup dynamics of mercury

We studied the breakup dynamics of liquid mercury by the help of rapid imaging and an electrical method based on the change in conductivity of the thinning fluid filament, which was presented in 2004 by Burton and co-workers [6]. The ultrarapid imaging experiments were conducted with two different setups: a syringe pump driven setup ('setup A', c.f. chapter 4) and a conductive copper setup ('setup B', Fig. 5.3), where the imaging data were complemented with synchronized electrical measurements (c.f. 5.2). By using these two different setups, we were able to (i) compare our imaging data with the results from other inviscid liquids obtained in the previous chapter (setup A), (ii) evaluate the potential influence of electrical current on the imaging results (setup A versus setup B) and (iii) compare the results from ultrarapid imaging ($\sim$ µs time scale) with the electrical ($\sim$ ns time scale) measurements (setup B).

---

[1] This MATLAB simulation was primarily conceived and carried out by Tijs van Roon (University of Amsterdam).

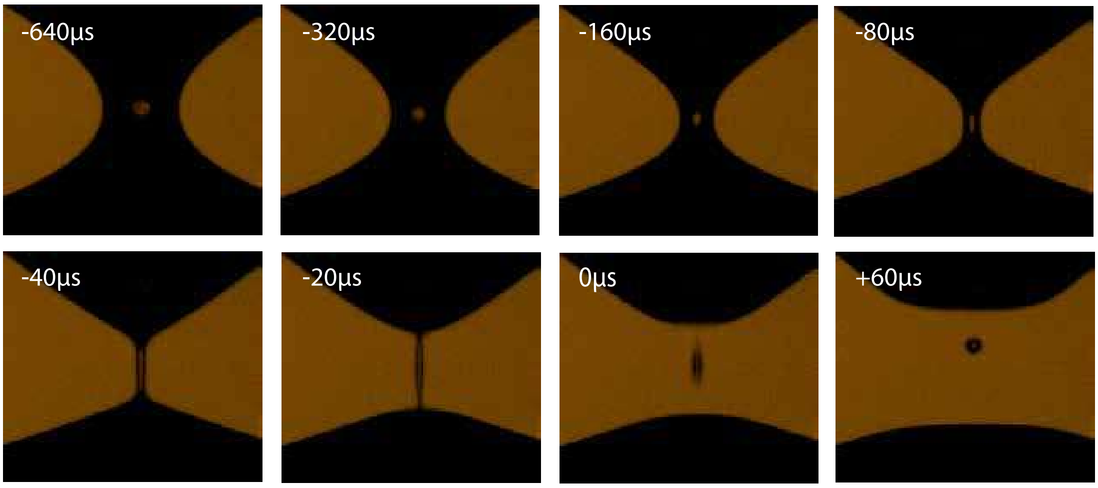

FIGURE 5.5: **Ultrarapid images of mercury obtained at different times to pinch-off τ ('*setup B*', 50.000 fps).**

Ultrarapid imaging

Fig. 5.5 depicts a representative series of movie frames taken at various times to pinch-off τ. There was no optically visible difference between the imaging data recorded with setup A (i.e. without electrical current applied) and the ones recorded with setup B (i.e. in the presence of electrical current). In both cases, the pinch-off behaviour resembled the one observed for the other simple liquids with a satellite drop forming each time after the fluid neck had broken up. The prefactor that we derived from these imaging data was found to be A = 0.90 ± 0.01, which is equally in line with the results of the previous chapter. This, in turn, corroborates our hypothesis presented in the previous chapter that the experimental prefactor of the inviscid scaling equation has a universal value of 0.9 (Fig. 5.6) with the exception of water and aqueous solutions.

Electrical measurements

Following the pinch-off dynamics with the electrical voltage divider circuit (setup B) yielded results that are very similar to Burton's [6]: the recorded $V - \tau$ curves almost overlap (Fig. 5.7) and using equ. 5.4 this leads to the same prefactor of A = 0.45 ± 0.02 for the minimum neck diameter (Fig. 5.8). The apparent qualitative difference between our data and Burton's data in Fig. 5.8 is primarily due to the

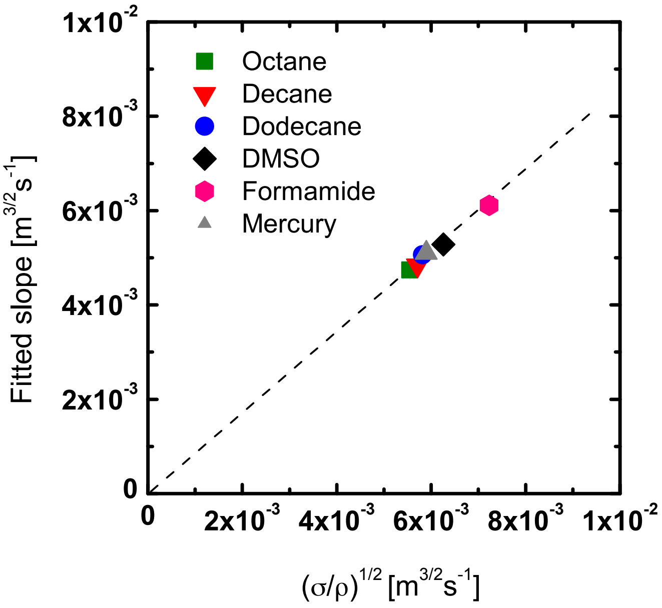

FIGURE 5.6: **Derivation of the universal prefactor from ultrarapid imaging data of simple inviscid liquids.** Mercury is on the same line with the other investigated liquids which corroborates that A has a universal value of 0.9 (c.f. chapter 4).

fact that we did not dispose of Burton's original experimental data and therefore could only retrieve his data from a log-log plot shown in his publication. Plotting our data in the same way as a $d - \tau$ curve on a log-log scale yields again almost identical results with a slope of $2/3$ as expected from the inviscid scaling equation (Fig. 5.9). Interestingly, if the input voltage is increased to 3 V or 5 V, this $2/3-$power law is disturbed for times closer to the break-up point.

Comparison ultrarapid imaging versus electrical measurements

As outlined above, our results obtained from these two different methods are individually consistent with other independent experiments, yet they are not in line with each other: the prefactor for the minimum neck diameter derived from ultrarapid imaging is with a value of $A = 0.90 \pm 0.01$ two times larger than the electrically determined prefactor of $A = 0.45 \pm 0.02$. Given that these two different experimental recording methods were synchronized and therefore should represent the same pinch-off event, there must be some additional factor(s) that

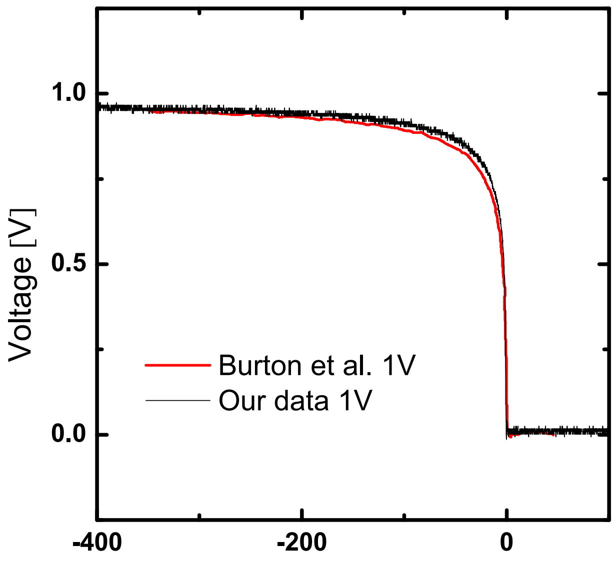

FIGURE 5.7: **Recorded V-τ curves.**

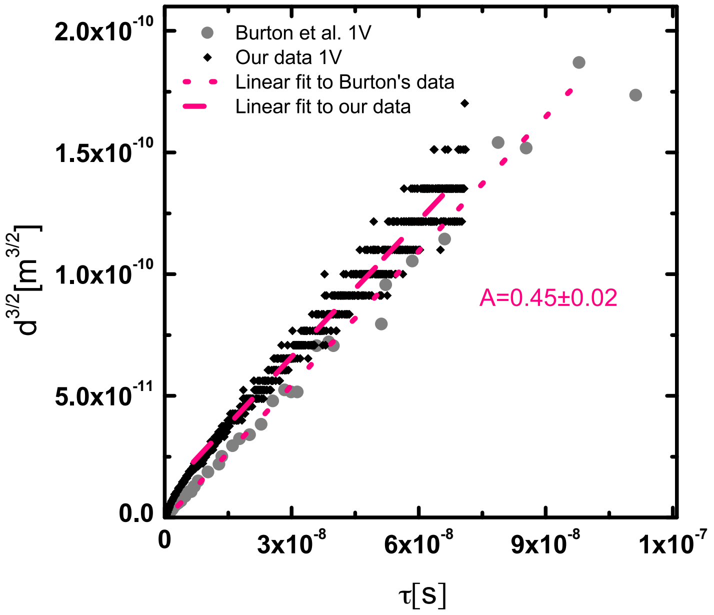

FIGURE 5.8: **Prefactor fits of the electrical measurements.**

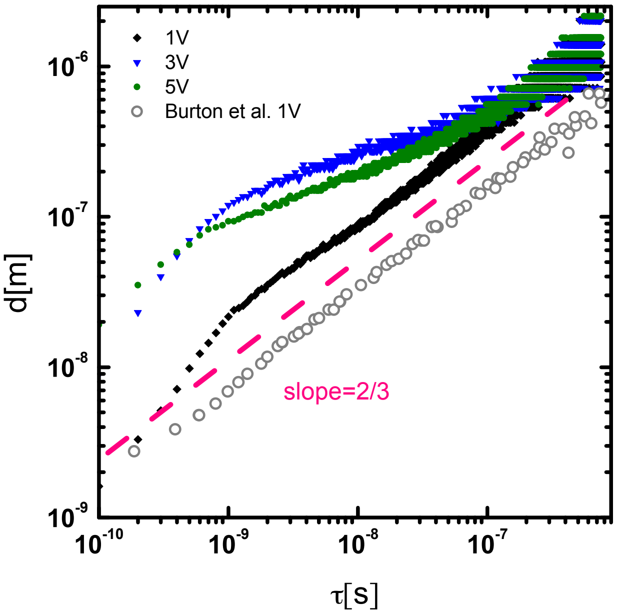

FIGURE 5.9: **Log-log plot of electrical mercury measurements.** The expected inviscid-power law behaviour can only be observed for an input voltage of 1 V.

need(s) to be taken into account. A first approach is to pool the recorded data in a single log-log plot, which, however, does not provide any further insight: in both cases a good fit to the expected $2/3-$power law can be attested with only a slight deviation for very short time scales (Fig. 5.10).

5.3.2 MATLAB simulation of the electrical pinch-off

In order to further elucidate the origin of the discrepancy between the prefactors derived by the two different methods, we modelled the electrical measurements in MATLAB. Both our and Burton's measured electrical signals display a significant ringing around the putative pinch-off point, where $V_s(\tau) = 0$. The associated negative voltage values V_s imply a negative resistance and can therefore not come from the sample itself, but must originate from a signal with high frequency components that exceed the 1 GHz bandwidth of our oscilloscope.

We started from a very simple physical model based on the inviscid scaling law (equ. 5.1) and the truncated cone resistor model (equ. 5.4). As displayed in

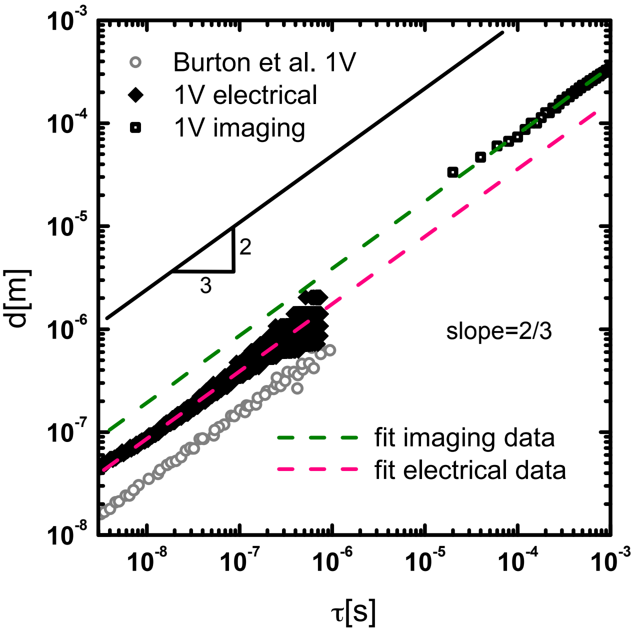

FIGURE 5.10: **Pooled data of mercury pinch-off dynamics.** At early times, the drop break-up was followed by the electrical methods. At longer times neck rupture was captured by ultra-rapid imaging.

Fig. 5.11, our rudimentary simulation revealed a large deviation from the experimental data for times close to the break-up point. The extremely steep slope of the measured voltage signal in this region cannot be accommodated by this basic model, irrespective of the choice of the prefactor A.

Since the fluid diameter in this region has shrunken to several nm, an increasing contribution from evaporation seems very likely. And indeed, plotting the expected current density I_d, defined as current per area $I_d = I/(\pi r_{min}^2)$ with $I = V_{in}/(50\Omega + R_{Hg}d^{-1})$, reveals a sharp exponential increase for the region close to the breakup point (Fig. 5.11A). We therefore extended our model by defining an evaporation point situated in this region. The incorporation of this (very) rudimentary evaporation model already yielded a significantly better overlap with the experimental data (V_{evap}).

Voltage [V]	A_{sim}	$I_{d,max}$ [GAm^{-2}]	d($I_{d,max}$) [nm]
1	0.13	7400	44
3	0.7	4100	120
5	0.63	2500	200

TABLE 5.1: **Simulation results of the electrical mercury pinch-off.**

However, we were still seeking to reproduce the ringing of the electrical signal that we hypothesized to originate from a contribution of the bandwidth limited oscilloscope itself. We therefore multiplied the evaporation model (V_{evap}) by a low-pass filter, which removed all high frequency components above 1 GHz. The resulting curve $V_{evap,low-pass}$ finally shows the observed undershoot following the pinch-off event and hence can be considered a fairly good approximation to the recorded experimental data: due to evaporation, which competes with the surface-tension driven thinning of the mercury filament, the neck rupture occurs a lot earlier than predicted by the inviscid scaling law. The premature, abrupt break-up of the filament ensues too fast for being followed in real-time by the oscilloscope which results in a ringing signal.

For each of the three tested input voltages we fine-tuned the evaporation point in order to obtain a maximum overlap with the experimental data. The corresponding filament diameters at the evaporation point d($I_{d,max}$) are 44 nm, 120 nm and 200 nm for 1 V, 3 V and 5 V respectively (Tab. 5.1). Since the current density increases with increasing input voltage, evaporation is triggered at earlier times and correspondingly longer filament diameters. The prefactor A was optimized with respect to the fit to the experimental data and interestingly, these optimal prefactors vary significantly with the applied input voltage. This in turn further supports our hypothesis that the break-up of the mercury filament in the electric measurements is not driven by capillarity alone.[2]

---

[2] This MATLAB simulation was primarily conceived and carried out by Tijs van Roon (University of Amsterdam).

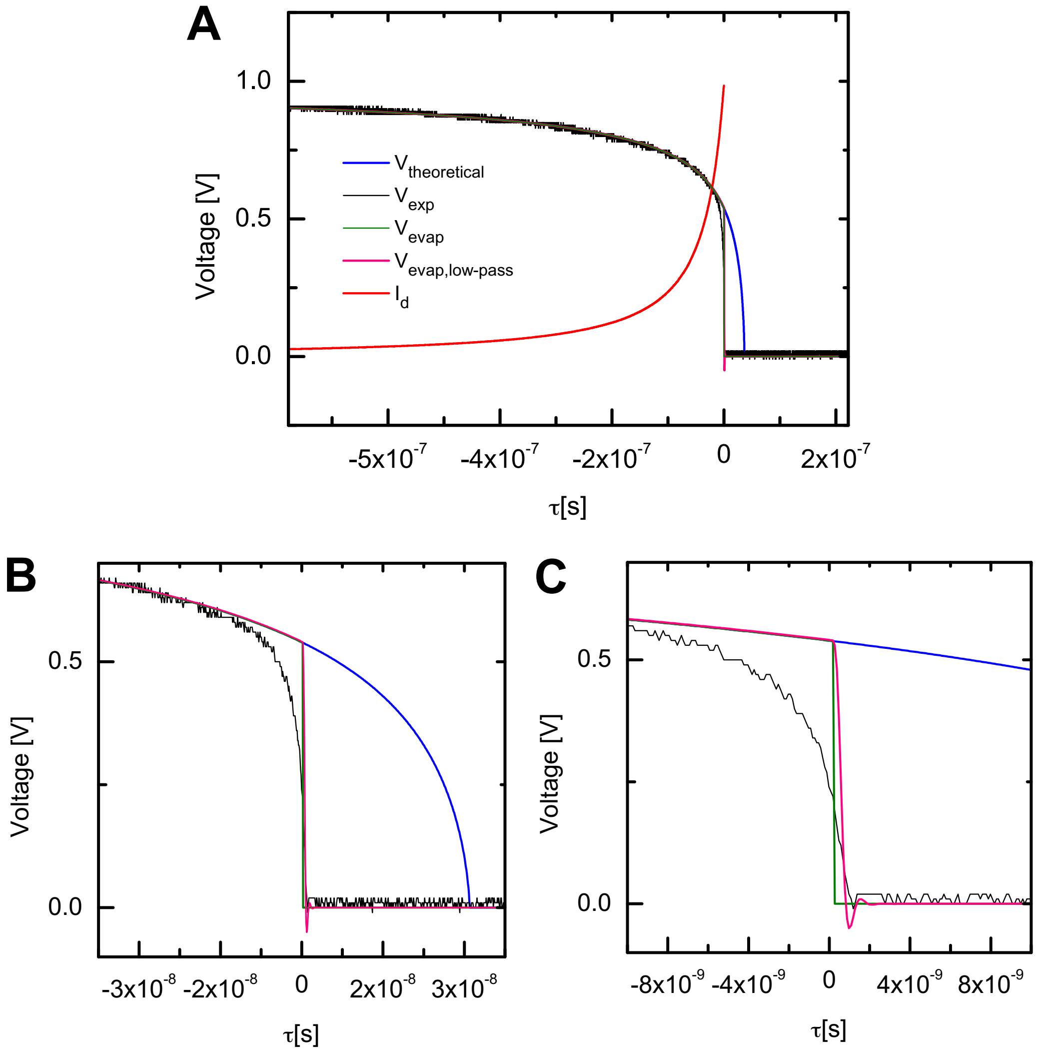

FIGURE 5.11: **Simulation of the electrical mercury pinch-off.** A: Whole experimental time range: the model shows a good agreement for longer times, but significantly deviates for times very close to the pinch-off point. The current density I_d increases exponentially with the thinning neck diameter. B and C: Zoom into the region around the putative breakup point (*simulation realized by Tijs van Roon, University of Amsterdam*)

.

5.3.3 The pinch-off behaviour of liquid gallium

In the previous section we have shown that Burton's electrical method is only to a very limited extent suitable for following the pinch-off dynamics of mercury as evaporation dominates over the surface tension driven thinning of the fluid filament in close proximity to the pinch-off point. Despite of this, the underlying conceptual idea remains very appealing and we considered it therefore compelling to test this method on at least one other inviscid fluid.

Unfortunately, the majority of these fluids, including the simple liquids studied in the preceding chapter, are little or non-conductive and therefore not compatible with the presented electrical setup. At the same time, electrical conductors such as metals are mostly solid under ambient conditions and only melt at very high temperatures. Gallium, however, has a fairly low melting point of ca. 302.91 K and can be easily transformed into a supercooled state yielding liquid Gallium at room temperature. The physical properties of (liquid) Gallium are quite well understood [8, 9] and display some interesting peculiarities: gallium has like mercury a fairly low viscosity of $\eta_{Ga} \approx 1.6$ mPas, so not even about twice the viscosity of water, but at the same time and unlike mercury, it practically does not evaporate due to its quasi-zero vapour pressure of $\mathrm{p}_{Ga}(302\ K) \approx 4.01e^{-38}$ mbar (c.f. vapour pressure of mercury $\mathrm{p}_{Hg}(293\ K) \approx 2e^{-3}$ mbar).

Just as in the case of mercury, the Ohnesorge number of Ga filaments stays smaller than 1 until the neck diameter d reaches dimensions of ~ 1 µm (Tab. 5.2 and 5.3). Therefore the inviscid scaling equation 5.1 should likewise be applicable over the entire experimentally probed diameter range of the thinning neck. All in all, these properties qualified gallium as another interesting simple, non-viscous liquid on which Burton's electrical method could be tested. Thus, in analogy to the mercury experiments, we followed the pinch-off dynamics of gallium by a combined approach of ultrafast imaging and the electrical voltage divider circuit.

Ultrafast imaging

As for mercury we acquired imaging data of the fluid neck rupture using both the syringe pump setup ('setup A') without applied electrical current and the synchronized electrical setup ('setup B', c.f. 5.2). While we observed no difference between setup A and B in the case of mercury, gallium behaved surprisingly

Liquid	ρ (gml^{-1})	σ (mNm^{-1})	η (mPas)
Water	1	72.9	0.89
Formamide	1.13	59	3.36
Mercury	13.63	474	1.53
Gallium	6.1	709	1.196
Glycerol	1.26	76.2	934

TABLE 5.2: **Physical parameters of selected liquids.**

diameter	Oh_{water}	$\mathrm{Oh}_{formamide}$	Oh_{Hg}	Oh_{Ga}	$\mathrm{Oh}_{glyerol}$
10µm	0.03	0.13	0.01	0.01	9.53
1µm	0.10	0.41	0.02	0.01	30.14
100nm	0.33	1.30	0.06	0.06	95.32
10nm	1.04	4.12	0.19	0.18	301.43
1nm	3.30	13.01	0.60	0.58	953.20

TABLE 5.3: **Expected pinch-off regimes for various liquids.** If $Oh < 1$ the dynamics follow the inviscid regime with a $d \propto \tau^{\frac{2}{3}}$ scaling law, if $Oh > 1$ the viscous regime is in place, where $d \propto \tau$.

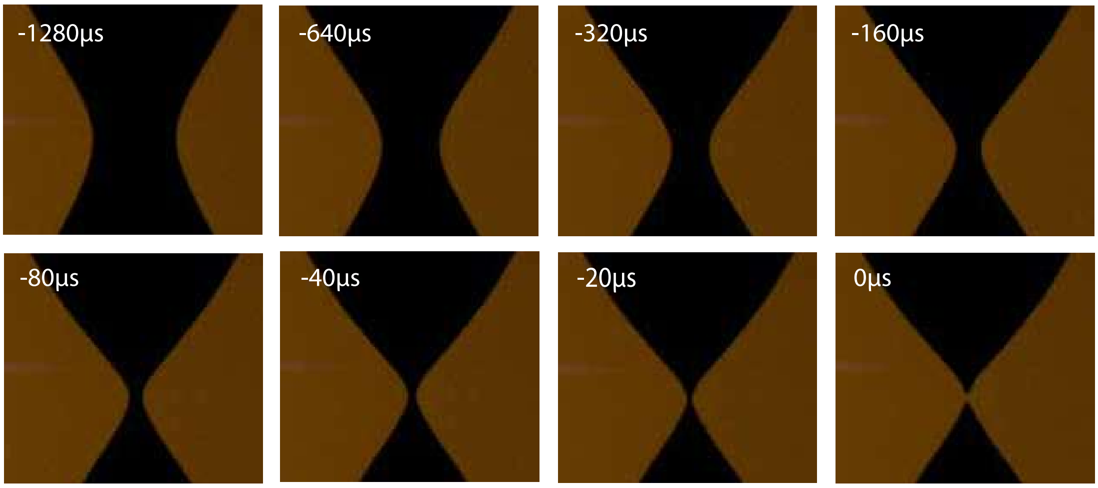

FIGURE 5.12: **Gallium pinch-off at various times to break-up τ.** Imaging setup (*'Setup A'*, 54.000 fps)

very different as soon as voltage was applied. This difference was already qualitatively visible in the recorded movies as shown in Fig. 5.12 and Fig. 5.13. In addition to that, the pinch-off behaviour in both cases is more indicative of a viscous regime where the rupture occurs more or less symmetrically. Nevertheless, the quantitative analysis revealed a $d \propto \tau^{\frac{2}{3}}$ power law obedience for both experimental conditions as expected in the case of an inviscid fluid (Fig. 5.14A+C). The derived prefactors, however, turned out to be quite different from our formerly studied simple fluids. For setup A we derived a prefactor A of approximately 0.7 for the fluid neck diameter (Fig. 5.14B), while setup B yielded even lower prefactors of 0.26, 0.24 and 0.18 for 1 V, 3 V and 5 V respectively (Fig. 5.14D). This apparent dependence of the prefactor on the input voltage suggests that there is a certain interference of the applied electrical current with the actual breakup of the gallium filament.

Electrical measurements

Analogously to the mercury experiments we coupled the ultrarapid imaging measurements in setup B to the oscilloscope output from the voltage divider circuit, which allowed us to record synchronized data on the electrical gallium pinch-off. The recorded $V - \tau$ curve displays a similar signal ringing around the pinch-off region as in the case of mercury (Fig. 5.15), which again indicated that

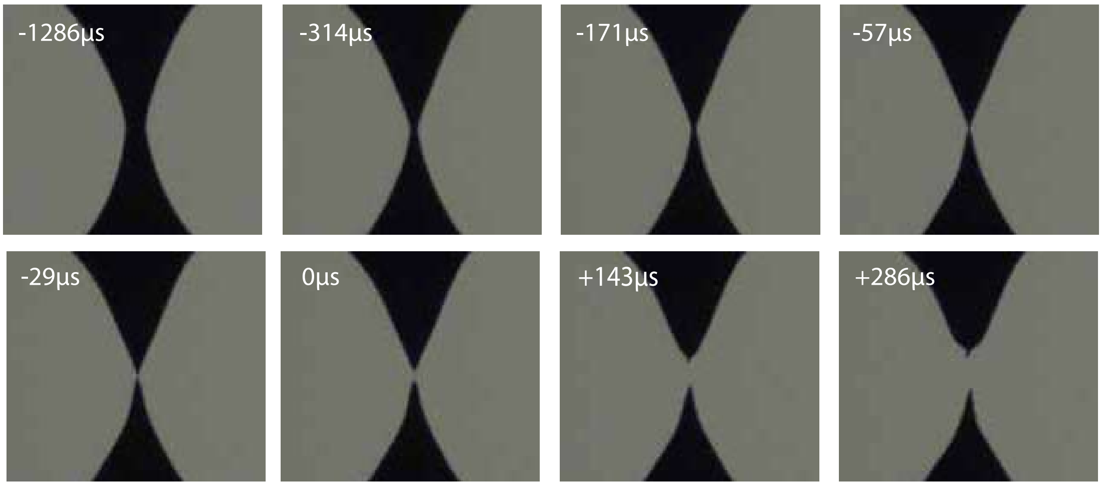

FIGURE 5.13: **Gallium pinch-off at various times to break-up τ.** Electrical setup (*'Setup B'*, 35.000 fps)

the rupture occurred faster than the oscilloscope could follow due to its limited bandwidth.

Since the corresponding movies were more reminiscent of a viscous pinch-off, the cone angle Θ was first verified to be approximately 18° by image analysis. Using equation 5.4 and assuming a resistivity of $\rho_{Ga} = 2.7 \times 10^{-7}\ \Omega\text{m}$ [10, 9] we derived a prefactor A of 0.35 ± 0.02 for the minimum neck diameter irrespective of the applied input voltage (Fig. 5.16B). Since this was not in line with the results from ultrarapid imaging, where the derived prefactor decreased with increasing input voltage, we verified once more the obedience to the $2/3$ inviscid scaling law. As shown in Fig. 5.16A, the corresponding $d - \tau$ loglog-plot has a slope of 0.56, which indicates that in the case of gallium a different or at least more complex physical process must be in place on nanometric time and length scales.

5.4 Discussion

In this chapter we investigated whether we can come closer to the singularity of inviscid drop break-up dynamics by the help of a promising experimental method presented by Burton and co-workers that relies on the decreasing conductivity of a thinning fluid filament [6]. Even though this method is restricted to conductive inviscid fluids, which basically only leaves mercury and supercooled liquid gallium for investigation at ambient conditions, it closes - if valid

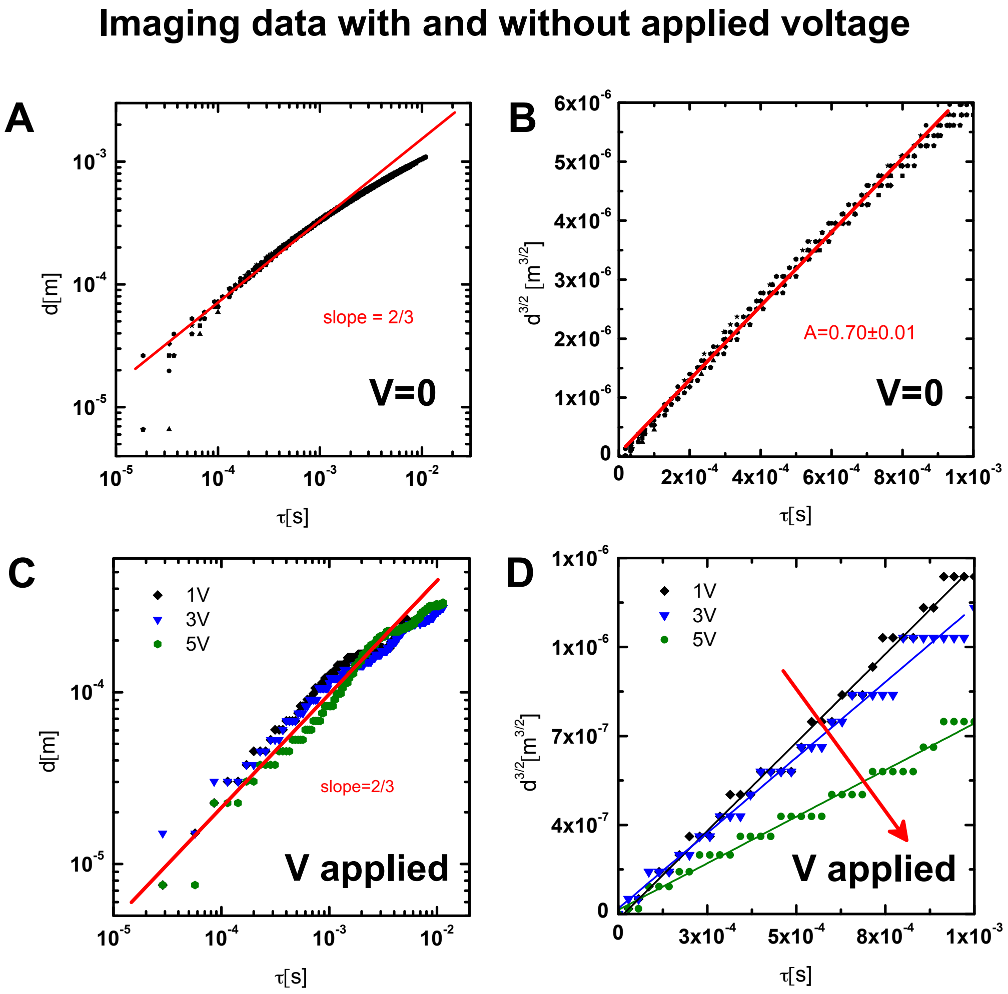

FIGURE 5.14: **Ultrarapid imaging data of the breakup of gallium** A: Derived diameter from ultrarapid imaging with syringe pump setup (*'Setup A'*, no electricity). B: Prefactor fit, *'Setup A'*. C: Derived diameter from ultrarapid imaging with electrical setup (*'Setup B'*). D: Prefactor fit, *'Setup B'*.

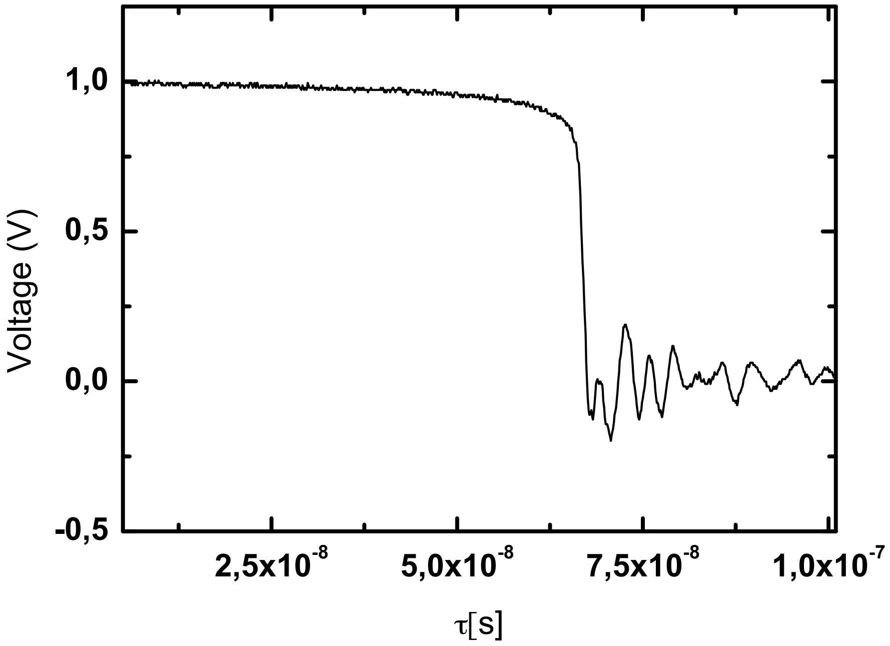

FIGURE 5.15: **Recorded $V-t$ curve for gallium**. A strong ringing occurs around the pinch-off region

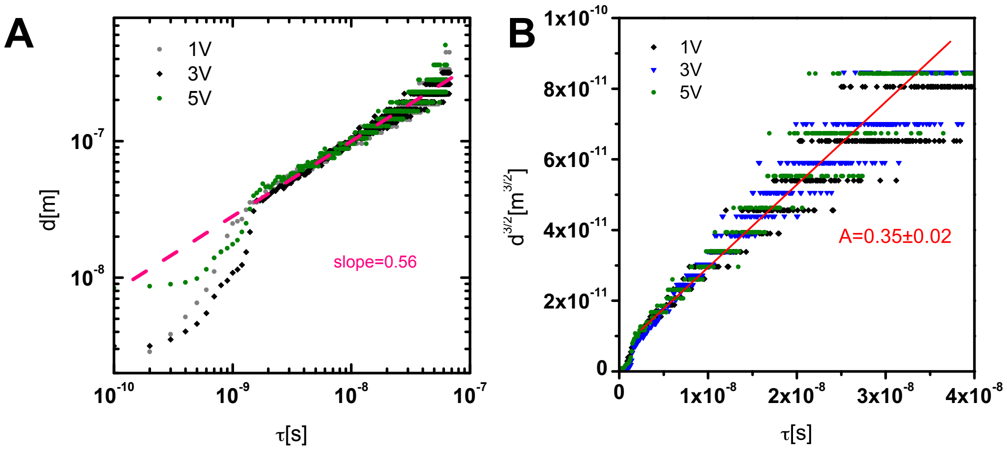

FIGURE 5.16: **Electrical measurements of the breakup of gallium.** A: Derived diameter from electrical measurements (*'Setup B'*). B: Prefactor fit, *'Setup B'*.

- the experimental gap for neck diameters $d_{min} >> l_v$, where a lot of theoretical uncertainty still persists (c.f. 5.1).

We therefore sought to validate Burton's electrical method, which we suspected to suffer from a methodological flaw insinuated by his experimental data that show a remarkable signal ringing around the pinch-off region. Since this cannot be explained by inviscid scaling laws alone, we remained very dubious about whether this really constitutes a suitable methodology for experimentally approaching the singularity on a nanosecond time scale.

Noise from surface evaporation

Essentially, we were able to reproduce the experimental results of Burton et al. on mercury. However, our simulations point at the need to account for evaporation from the surface of the mercury filament: as the latter becomes thinner, current density increases exponentially and causes a premature filament rupture driven by evaporation. This sudden transition happens on a very short time scale and cannot be grasped by the bandwidth limited oscilloscope. The latter only follows with a delay, which, in turn, produces the observed ringing of the electrical signal in the pinch-off region.

Noise from surface oxidation

In the case of gallium a different form of noise has to be accommodated for: surface oxidation and electro-hydrodynamical effects. We observed a significant difference in the pinch-off behaviour as soon as electrical voltage was applied. This was not only optically visible in the ultrarapid imaging movies, but also reflected quantitatively in the prefactors we derived from the acquired data: higher applied voltages lowered the prefactor and for nanometric length scales we were not even able to observe a $2/3$ scaling law any more - unlike in the case of mercury. Clearly, the surface of gallium undergoes a drastic change in the presence of electrical current, which becomes even more pronounced for sub-micrometric neck diameters.

Similar indications for this already exist in recent literature: Khan and coworkers showed that the surface tension of gallium can indeed be tuned by the application of very low electrical voltages [11]. They reversibly switched the interfacial tension of a liquid alloy of gallium from ~ 500 mJ/m^2 to almost zero by electrochemical oxidation or reduction of surface metal atoms, where the presence of surface oxides lowered the surface tension. According to Khan, surface metal oxides can be viewed as 'intrinsic' surfactants that - other than conventional surfactants - allow to control the surface tension of metals and metallic alloys in a reversible manner.

In our mercury and gallium experiments we carefully removed the rapidly forming oxide layer prior to each individual measurement. In the case of mercury, this was sufficient to obtain results that are consistent with previous imaging experiments (c.f. chapter 4: ultrarapid imaging with setup A) and in line with results presented in the literature (electrical measurements with setup B) [6]. For Gallium, in contrast, removing the visible oxide layer was obviously not enough: although the ultrarapid imaging data supported the validity of the inviscid scaling law for the gallium pinch-off, we only derived a prefactor of 0.7 for the minimum neck diameter in the absence of electrical voltages (setup A), which is presumably due to incomplete removal of surface oxides. These lower the surface tension which, if not accounted for, leads to lower apparent prefactors. The surface coverage with gallium oxide increases with increasing applied voltage, which results into even lower prefactors in setup B.

Since the current density increases exponentially with decreasing minimum neck diameter, the concentration of gallium oxides (and hence of 'intrinsic' surfactants) in the pinch-off region can be expected to equally multiply exponentially. This results in a partially solidified filament at the actual instant of breakup and can be seen optically in the ultrarapid movies for frames after $\tau = 0$ (Fig. 5.13). These observations reveal a remarkable difference with respect to the behaviour that has been found for conventional surfactants: Saint Vincent and co-workers have shown that the rupture zone is depleted of surfactants due to the dominance of the extremely high rates of surface stretching over surfactant diffusion [12].

The absence of similar voltage induced surface oxidation effects in the case of mercury is presumably due to its higher standard potential ($E^{\ominus}$ ($Hg^{2+} \mid Hg$)= +0.854 V versus $E^{\ominus}$ ($Ga^{3+} \mid Ga$)= -0.52 V).

Noise from thermal capillary waves and other noise sources

Drop fission is an inherently strongly non-linear process with a broad spectrum of potential noise sources during experimental data acquisition. This noise can originate not only from evaporation or the presence of surfactants (i.e. metal oxides in the case of gallium as outlined above), but also be evoked by air currents, pressure fluctuations of the nozzle or thermal fluctuations. The presence of noise can drastically affect the breakup dynamics of a thinning fluid, especially at very short time and length scales. Therefore in particular the late stages of drop breakup, where $\mathrm{d}_{min} < \mathrm{l}_v$, are very susceptible to perturbations, which in turn affects the shape of the interface close to the singularity.

One of the few experimental accounts on the influence of noise during drop fission has been presented by Shi, Brenner and Nagel [13]. Using ultrarapid imaging they studied the shape of the interface near the singularity and found it to be "rough" with necks growing over other necks. They further showed that the formation of such neck cascades *at infinitum* is robust in simulations as long as a noise source is present. In the absence of noise, in contrast, their simulations produced a smooth interface, which, however, poorly reflects real experimental conditions. Even though their experiments were limited to viscous drops due to the camera resolution limit of ~ 1 µm, their results should in principle equally apply to non-viscous fluids, that eventually (but on much shorter length scales) will also cross over to the generic regime where viscosity becomes relevant.

Although their experiments suggested that neck cascades forms regardless of the source of the noise, they focussed their subsequent discussions regarding experimental noise on thermal capillary waves [14]. The latter become more important as soon as the neck diameter has shrunken to a certain threshold neck diameter d_θ, which can be approximated using the account of Landau and Lifshitz on hydrodynamic fluctuations [15]:

$$d_\theta = 10 l_v \left(\frac{l_t}{l_v}\right)^{0.401} \tag{5.5}$$

where l_v is the viscous length scale and l_t corresponds to the thermal length scale defined as $l_t = \left(\frac{k_B T}{\sigma}\right)^{1/2}$.

The interesting question relevant to our experiments is now whether thermal capillary waves might already play a role at the length scales probed during the electrical measurements: according to equation 5.5 this threshold neck diameter d_θ should lie in the order of picometers for both gallium and mercury, i.e. d_θ(Ga) $\approx$ 3.4 pm with l_t(Ga)= 892 pm and d_θ (Hg) $\approx$ 2 pm with l_t(Hg)= 362 pm respectively. This corresponds in both cases to subatomic dimensions (r(Ga)= 130 pm; r(Hg)= 150 pm), while the experimentally probed range lies between a few nanometers and 1 µm. Nevertheless, equation 5.5 only provides a rough approximation and might therefore under-or overestimate the actual value [16].

On these lines, Case and Nagel performed similar, conductivity-based experiments on the coalescence of inviscid NaCl drops and observed an unexpected regime that becomes visible for $\tau << 10$ µs [17]. Without being able to provide a sound, complete explanation for the unanticipated emergence of this regime, their work suggests that both droplet coalescence and droplet formation dynamics of inviscid fluids are yet incompletely understood for sub-micrometric neck diameters. It can therefore not be excluded that additional noise sources - other than voltage-induced surface evaporation and oxidation - contribute to the electrically observed rupture dynamics of mercury and gallium, which gives rise to lower apparent prefactors and/or a different scaling regime.

5.5 Conclusion

Taken together, we showed that Burton's electrical method is not suitable for experimentally approaching the moment of droplet fission on nanometric time and length scales. In the case of mercury the applied voltage introduces an additional source of noise by promoting evaporation from the surface, which becomes prominent for sub-micron fluid neck diameters. This falsifies the observed hydrodynamics and leads - potentially in conjunction with other noise sources - to the derivation of implausibly low prefactors. On the same lines, electro-hydrodynamical effects were attributed a preponderant role in the case of gallium and constitute therefore another major source of noise that distorts the observation of the pure hydrodynamical filament breakup process. To what extent yet other, additional noise sources play a role on sub-micrometric length scales still remains an open question.

Bibliography

[1] M. P. Brenner, J. Eggers, K. Joseph, S. R. Nagel, and X. D. Shi. Breakdown of scaling in droplet fission at high Reynolds number. *Physics of Fluids*, 9(6):1573–1590, 1997.

[2] A. U. Chen, P. K. Notz, and O. A. Basaran. Computational and Experimental Analysis of Pinch-Off and Scaling. *Physical Review Letters*, 88(17):174501, 2002.

[3] R. F. Day, E. J. Hinch, and J. R. Lister. Self-Similar Capillary Pinchoff of an Inviscid Fluid. *Physical Review Letters*, 80(4):704–707, 1998.

[4] J. R. Castrejón-Pita, A. A. Castrejón-Pita, E. J. Hinch, J. R. Lister, and I. M. Hutchings. Self-similar breakup of near-inviscid liquids. *Physical Review E*, 86(1):015301, 2012.

[5] J. Eggers and T.F. Dupont. Drop formation in a one-dimensional approximation of the Navier Stokes equation. *Journal of Fluid Mechanics*, 262:205–221, 1994.

[6] J. C. Burton, J. E. Rutledge, and P. Taborek. Fluid Pinch-Off Dynamics at Nanometer Length Scales. *Physical Review Letters*, 92(24):244505, 2004.

[7] J. D. Romano and R. H. Price. The conical resistor conundrum: A potential solution. *American Journal of Physics*, 64(9):1150–1153, 1996.

[8] G. J. Abbaschian. Surface tension of liquid gallium. *Journal of the Less Common Metals*, 40(3):329–333, 1975.

[9] M. Pokorny and H. U. Astrom. Temperature dependence of the electrical resistivity of liquid gallium between its freezing point (29.75 degrees C) and 752 degrees C. *Journal of Physics F: Metal Physics*, 6(4):559, 1976.

[10] R. W. Powell. The Electrical Resistivity of Gallium and Some Other Anisotropic Properties of this Metal. *Proceedings of the Royal Society of London. Series A, Mathematical and Physical Sciences*, 209(1099):525–541, 1951.

[11] M. R. Khan, C. B. Eaker, E. F. Bowden, and D. D. Dickey. Giant and switchable surface activity of liquid metal via surface oxidation. *Proceedings of the National Academy of Sciences*, 111(39):14047–14051, 2014.

[12] M. R. D. Saint Vincent, J. Petit, M. Aytouna, J. P. Delville, D. Bonn, and H. Kelly. Dynamic interfacial tension effects in the rupture of liquid necks. *Journal of Fluid Mechanics*, 692:499–510, 2012.

[13] X. D. Shi, M. P. Brenner, and S. R. Nagel. A Cascade of Structure in a Drop Falling from a Faucet. *Science*, 265(5169):219, 1994.

[14] M. P. Brenner, X. D. Shi, and S. R. Nagel. Iterated Instabilities during Droplet Fission. *Physical Review Letters*, 73(25):3391–3394, 1994.

[15] L. D. Landau and E. M. Lifshitz. *Chapter VI - Perturbation Theory*, pages 133–163. Pergamon, 1977.

[16] J. Eggers. Nonlinear dynamics and breakup of free-surface flows. *Reviews of Modern Physics*, 69(3):865–930, 1997.

[17] S. C. Case and S. R. Nagel. Coalescence in Low-Viscosity Liquids. *Physical Review Letters*, 100(8):084503, 2008.

Chapter 6

Oil-water displacement in rough pore microstructures

6.1 Introduction

The relative wettability behaviour of different fluids within a porous network plays an important role in many fields of science and technology and therefore constitutes one of the major themes in current porous media research [1, 2]. A considerable fraction of associated scientific quests are motivated by the petroleum industry in the context of Enhanced Oil Recovery (EOR).
With most renewable energy technologies still in their infancy, oil and gas remain the world's primary energy carriers in the medium-term. On these lines and considering the scarcity of these resources, an optimal exploitation of existing oil fields through the improvement of current recovery methods is of utmost importance. At present, recovery rates lie, at best, in the range of 30−45 % after application of primary and secondary extraction techniques. The achievement of higher recovery fractions could ensure energy production for at least the upcoming decades even under the assumption of fast economic growth scenarios [3, 4]. However, most of these residual oils are 'trapped' in very small micrometric pores of the reservoir rock (cf. Fig. 6.1), which makes efficient recovery difficult despite the advent of promising new enhanced extraction approaches ('tertiary recovery') ranging from the addition of surfactants [5] to the injection of chemicals [6, 7] or CO_2 [8].

That being said, efficient recovery techniques need to accommodate for a wide range of length scales reaching from the micrometric dimensions of the porous reservoir rock to the kilometre-wide extent of the entire extraction site (Fig. 6.1). As a consequence, a profound understanding of the complex physical

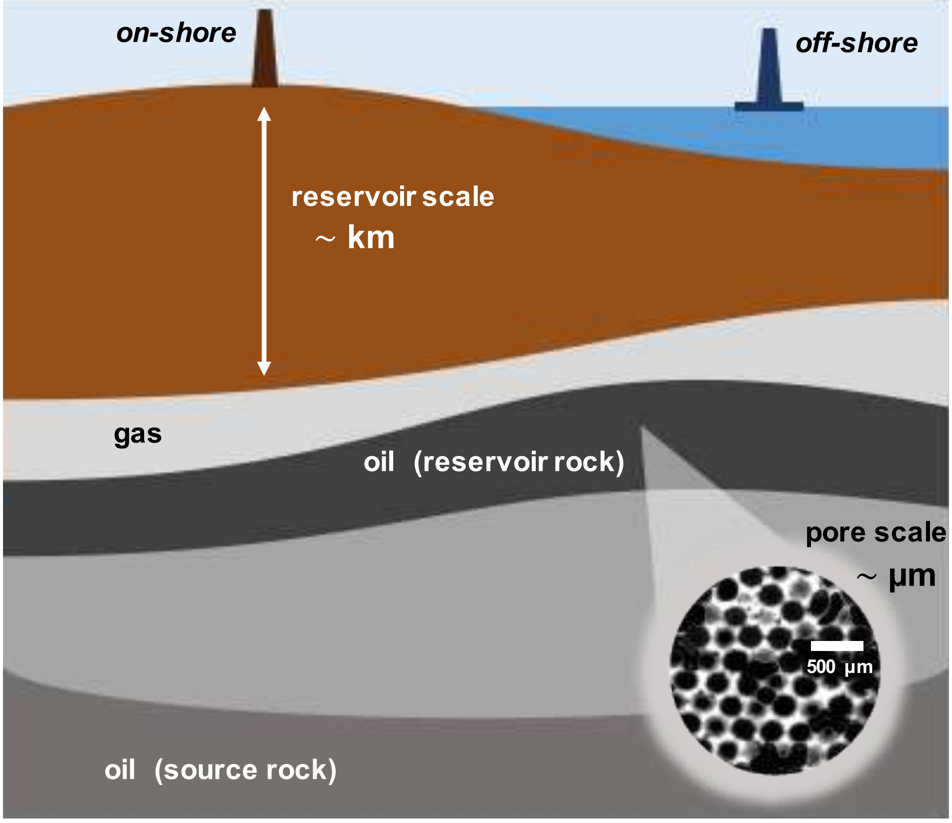

FIGURE 6.1: **Schematic sketch of an oil reservoir.** The length scales encountered in the EOR problem range from micrometric (oil pores in the reservoir rock) to kilometric dimensions (entire reservoir).

processes underlying wettability behaviour and relative oil-water displacements at each of these length scales is crucial for the design of new, economically viable and environmentally sound EOR strategies.

The term 'wettability' itself is a collective term for describing physical processes on different length scales from a three-phase wetting perspective. The enhanced oil recovery problem [9] has primarily been based on this approach: on the nanoscale, wetting behaviour is characterized by the relative distribution of local contact angles as a result of adsorption and other molecular interactions. On the mesoscale (~ µm), this molecular perspective is replaced by a more macroscopic description, where wetting is described in terms of capillarity effects that drive relative fluid movement on the level of individual reservoir pores. These microdisplacements further subsume into the wettability of a network of these pores which, in turn, finally results into the macroscopic wetting and fluid flow behaviour that can be observed on the scale of the entire reservoir ($\sim$ km). Within this framework, additional attention has been attributed to the geometry of the pore network - the particular structures of intertwined pathways that are linked via throat-like constrictions - as another major parameter directing relative fluid displacements. Surface topology, in contrast, which can equally vary considerably between individual porous rocks, and its potential influence on the wettability of the reservoir is usually not accounted for in current EOR literature. Correspondingly, roughness considerations are either entirely omitted or merely introduced within the traditional Wenzel/Cassie-Baxter framework, according to which ideal recovery of an entrapped oil droplet is bound to its transition from a partially wetted Cassie-Baxter to a fully wetted Wenzel state [10, 11, 12]. This, however, merely applies to hydrophobic solid phases. Naturally occurring solid phases are often (more) hydrophilic, particularly rock surfaces encountered in oil reservoirs.

Recently Bertin and co-workers [13, 14] have challenged the existing theoretical frameworks by presenting experimental evidence that strongly points at the crucial role of roughness for oil-water displacements in porous networks. They assessed significant differences in the recovery rates of the same oil from chemically identical, but topologically different porous rocks. These striking macroscopic results provided the grounds for our work that investigates the effect of surface topology on the microscale, which - to the best of our knowledge - has not yet been addressed elsewhere in the literature. Existing accounts on fluid flow in a micrometric roughness have so far been limited to gas-flow experiments [15]) or fluid flow simulations [16, 17, 18, 19], mostly in hydrophobic channels [20] all of which are not suitable for providing the still lacking microscopic counterpart to Bertin's macroscale experiments.

In the following, we present a microfluidics based approach to study oil-water displacement in rough micrometric channel and network structures. The effect of rock roughness as an important physical parameter for oil recovery processes was investigated on the pore scale using a set of generic microfluidic devices with roughness features varying from 1 to 140 µm. The displacement of non-wetting fluid (alcane) by wetting fluid (water) was followed in real time by fluorescent microscopy from which quantitative data on the recovery were derived. In this context, we also investigated the role of viscosity comparing decane (η = 0.92 mPas) versus hexadecane (η = 3.47 mPas) displacement and examined the influence of the flooding flowrate on the size of the retained oil droplets.

6.2 Materials and Methods

6.2.1 Design of rough microdevices

In order to assess the effect of roughness on oil-water microdisplacements we fabricated various microchannels with different feature sizes representing 'roughnesses' between 1 and 140 µm.

Design of rough single pore structures

Channels with a 'microroughness' were realized by powderblasting (Micronit Microfluidics, Enschede, The Netherlands) of borosilicate glass substrates. The resulting microfluidic channels (channel dimensions L = 40 mm W = 280 µm H = 112 µm) dispose of roughness features that are sized between 1 and 3 µm and located on the bottom and on the side walls of the channels (Fig. 6.2A). Larger roughness features were introduced by dry-etching of a repetitive 'zigzag' pattern into the borosilicate glass substrate yielding microchannels with well defined cavities of 10 and 20 µm on their respective side walls (Fig. 6.2B and C, channel dimensions L = 40 mm W = 60 µm H = 20 µm).

Overall and as illustrated in Fig. 6.2, all of these fabricated microfluidic glass channels have very similar channel dimensions, but carry very different roughness features and therefore allow to study the isolated effect of roughness on oil-water displacement.

Design of rough network structures

A larger characteristic roughness size was realized by the preparation of two-dimensional (2D) porous networks in the laboratory which we will in the following refer to as 'unimodal' and 'bimodal' porous media in line with the terminology used by Bertin and co-workers [13, 14].

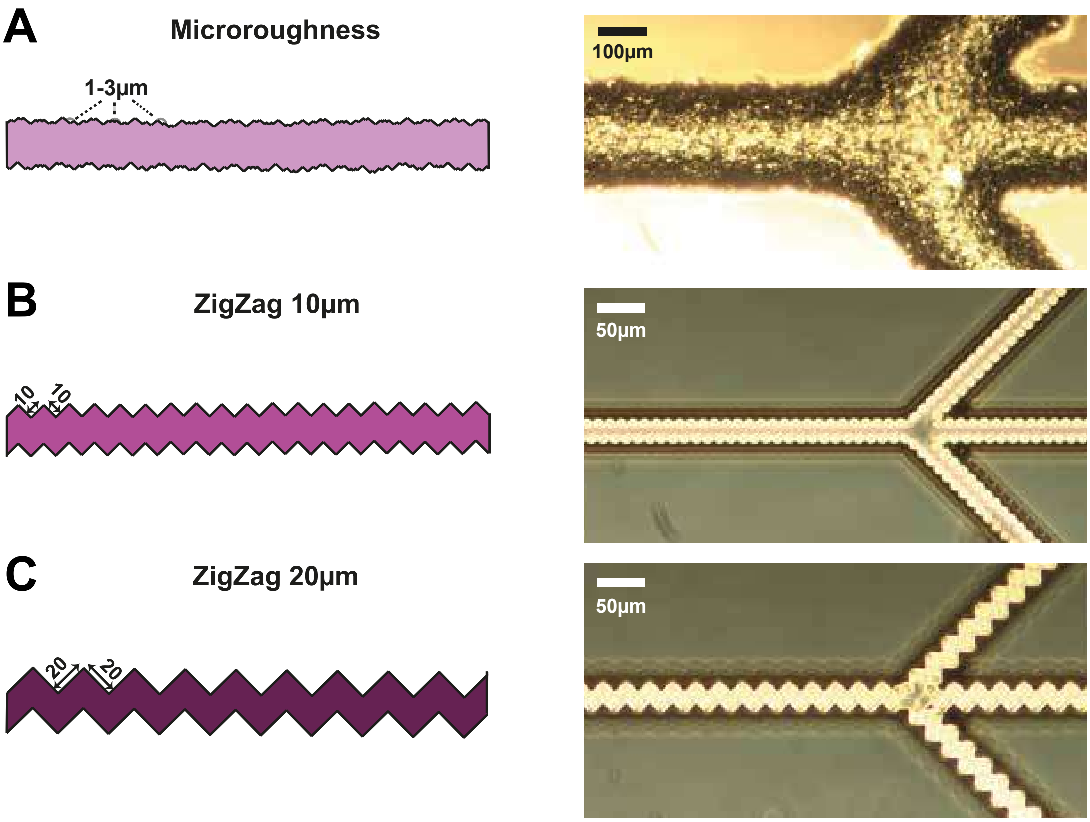

FIGURE 6.2: **Rough microchannels.** *Left:* Schematic top view *Right:* Bright field microscopy top view

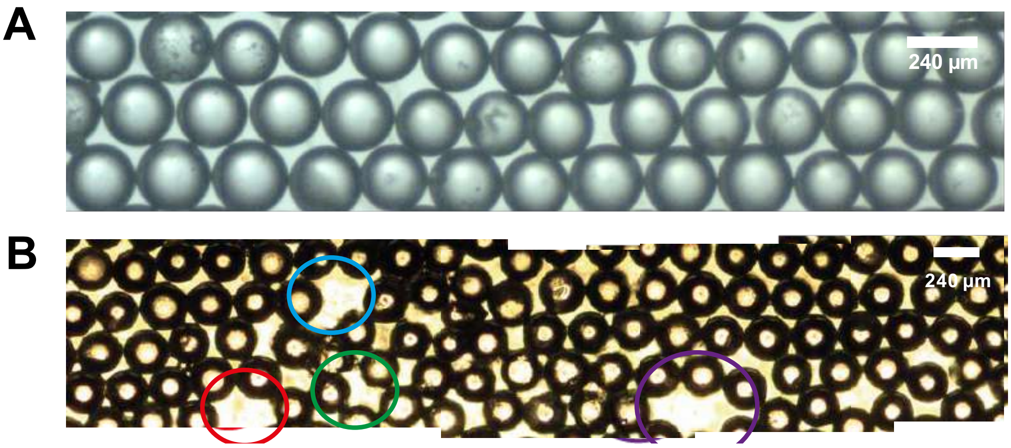

FIGURE 6.3: **2D Porous Media with roughness features (bright field images).** A: Unimodal porous media with pore sizes of 80 µm. B: Bimodal porous media with different pore sizes.

Micro-capillaries (CM scientific, L = 50 mm, W = 3 mm H = 300 µm) that had been sealed on one end were filled with soda lime glass beads (⌀ = 210-250 µm, 710°C) and subsequently equally sealed on the other side. After a centrifugation step of 25 min at 3000 g, a specific heating and cooling protocol was applied to the capillaries using a programmable oven (Rampmaster Evenheat). The proper attachment of the glass beads to the capillary walls was ensured by placing a load upon the capillaries during the entire sintering procedure. The resulting 'unimodal' 2D porous media consists of a monolayer of equally sized homogeneously packed glass beads with a diameter of 240 μm (Fig.6.3A). The corresponding uniform pore size of 80 μm is approximated based on empirical relations from porosity studies (pore size = bead size/3) and can be equated with the roughness of the porous media. The measured porosity of these unimodal networks lies in the range between 32−36 %.

A second type of porous media with different pore sizes was fabricated according to a similar protocol. These 'bimodal' 2D networks were obtained by filling the microcapillaries with a mixture of glass beads and NaCl salt crystals, which, in a later step, were washed off giving rise to a second type of (larger) pores (Fig. 6.3B). After the sintering step, the capillaries were immersed into a warm water bath (∼ 80°C) for 6 hours until the salt crystals were completely dissolved. Prior to usage in our experiments, we dried the produced bimodal porous media in an oven at 80°C for 24 hours. The porosity of these bimodal variants was determined to amount to $40-48$ %.

6.2.2 Water flooding experiments

All water flooding experiments were performed using the microfluidic setup depicted in Fig. 6.4. The rough microdevices are connected to the water and oil reservoirs (microsyringes with a volume of 250 µl, Hamilton) via a three-way valve (Stopcock 4, Cole-Parmer, US) and the flow was controlled by the help of a syringe pump (PhD 2000, Havard Apparatus). At the onset of the experiment, the microdevice is filled with the fluorescently labelled ($\sim$ 1 µM perylene bisimide derivative), non-wetting fluid (*here:* decane or hexane). After 30 min, the valve is switched and the wetting fluid water is injected into the microsystem at various flowrates (c.f. section 6.3). The induced oil-water microdisplacement process is followed by a laser induced confocal fluorescent microscope (Zeiss LSM 5 Pascal, Germany). The recorded fluorescent images allow to derive the areas occupied by the water and the alcane phase respectively: the relative abundance of each phase in the $xy-$plane located in the middle of the channel is calculated through threshold-based image binarization (ImageJ), from which fairly good quantitative estimates of the amount of oil trapped in a given microdevice at a given time can be obtained as an oil recovery rate. For every tested experimental condition an additional control experiment with smooth side walls was performed. Potential hysteresis effects of the wetting behaviour were prevented by using a new, unused device each time.

6.3 Results and Discussion

In the present study we investigated the effect of roughness on water-oil microdisplacement behaviour which has so far been largely omitted in the existing accounts within current EOR literature - despite strong circumstantial evidence that roughness does constitute a crucial determinant of wetting patterns in porous media [13, 14]. To this end we designed and fabricated various microfluidic devices that dispose of roughness features sized between 1 and 140 µm. The designed devices represent either a single pore or a 2D porous network and their micrometric dimensions can be considered representative of the micropores found in real oil reservoirs.

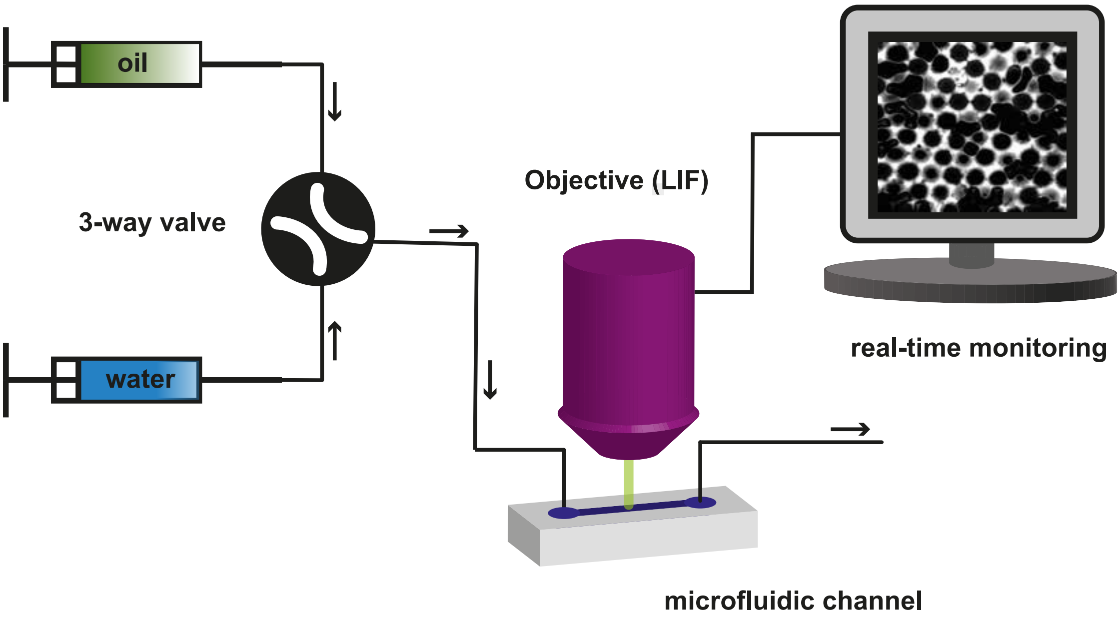

FIGURE 6.4: **Microfluidic waterflooding setup.** The displacement of a non-wetting fluid (hexane or decane) in a microfluidic device by a wetting fluid (water) was realized by the help of a syringe pump operated 3-way valve system, that allows to switch between an oil and a water reservoir. Laser induced confocal fluorescent microscopy was used for real-time monitoring of flooding and displacement processes in the microfluidic channel.

TABLE 6.1: Physical parameters of studied liquids

Property	**Density** ρ/kgm^{-3}	**Viscosity** η/mPas	**Interfacial tension** γ/mNm^{-1}	**Contact angle** Θ
Water	997	0.89	-	23°
Decane	730	0.92	50	$\sim 0°$
Hexadecane	770	3.47	46	$\sim 0°$

6.3.1 Effects of roughness and viscosity on oil recovery

We performed 'waterflooding' experiments as outlined in the experimental section, which consist of a primary imbibition of the microdevice with the wetting phase (*here:* decane or hexadecane, contact angle $\Theta \approx 0°$) followed by a drainage step, where the wetting phase is displaced by a less wetting phase (*here:* water, $\Theta \approx 23°$).

Fig. 6.5 illustrates the overall water-oil displacement behaviour for different roughnesses (microdevices) and viscosities (alcanes). t_0 denotes the initial state where the device is completely filled with the fluorescently labelled wetting fluid (oil). The final state t_{end} corresponds to the time point after flooding from which onwards the fluorescent recording does not show any further visible change. As depicted in this qualitative data matrix, both roughness and viscosity seem to constitute remarkable determinants of the observed fluid displacement patterns.

The inviscid decane (η = 0.92 mPas) is immediately and (almost) completely displaced by the injected water stream irrespective of the size of the channel roughness if the roughness size is unimodal and smaller than 100 µm. For larger roughnesses and a bimodal pore distribution, a small quantity is retained (c.f. Fig. 6.10A). In contrast to that, the trapping behaviour of hexadecane with a roughly four times higher viscosity (η = 3.47 mPas) is already affected by the presence of smaller roughness features: while no visible oil quantity remained trapped in the microroughness devices ($1-3$ µm roughness), increasing amounts of retained oil were observed for larger roughnesses of 10, 20, 80 and 100 µm respectively (Fig. 6.5, *c.f. also* Fig. 6.10C).

Fig. 6.6B shows these findings in more quantitative terms as an oil recovery plot that was derived from the fluorescent recordings through image binarization and analysis. For the 'ZigZag' devices, where the roughness features are only located at the side walls of the microchannel, the analysis was solely based on the area of this zigzag geometry. The exclusion of the straight (middle) part of the channel, where no trapping occurs, ensures that the derived oil recovery rate is strictly associated with the roughness effect and not distorted by any influences from the pressure driven flow in the centre of the channel (Fig. 6.5A). In the case of decane, very high recovery rates of 98 ± 2 % were obtained for roughnesses up to 80 µm, underlining that surface topology does not play a substantial role in this regime. In the presence of larger roughnesses $>$ 80 µm (and a bimodal pore distribution) a diminution of the recovery rates to $\sim$ 80 % was observable. In contrast to that, the recovery rate of hexadecane decreased from $\sim$ 100 % to $\sim$ 65 % as the roughness size increases from 1 to 140 µm (Fig. 6.6B) and hence showed a pronounced roughness dependence on the device topology over the entire studied experimental range.

6.3.2 Effect of the flowrate on trapped droplet sizes

As outlined in section 6.1 capillary forces are traditionally believed to be at the origin of oil trapping. The associated capillary number, given by $Ca = \eta \cdot U \cdot \gamma$ with U denoting the fluid flow speed, reflects the relative dominance of viscous over surface tension forces acting across an interface. We have already affirmed in the previous section that a higher viscosity (hexadecane versus decane) results into a higher degree of oil entrapment which we could visualize by the help of fluorescence microscopy. We therefore deemed it interesting to investigate whether an increase in the intrachannel flowrate U would equally lead to a higher degree of oil entrapment. And, if so, whether the diameter of the trapped oil drop can be related to the capillary number by a 1/3 power law as predicted within the framework of the 'Bretherton problem' [21, 22]:

$$d_{trapped\ drop} \propto Ca^{\frac{1}{3}} \tag{6.1}$$

To this end we repeated the waterflooding experiments described in section 6.2 as 'flow rate ramps', i.e. we subsequently flooded a given microfluidic device ('ZigZag 10' or 'ZigZag 20') filled with either decane or hexadecane with five different flowrates (50, 100, 250, 500 and 1000 nlmin^{-1}) from low to high and calculated the average diameter of the trapped oil droplets for each flowrate.

As illustrated by the recorded fluorescence images of the flooding end state in Fig. 6.7, the water flowrate had a substantial influence on the average size of the trapped oil droplets. Plotting the average diameter of the entrapped oil drops versus the capillary number we obtained indeed a fairly good fit to the anticipated 1/3 power law scaling (Fig. 6.8).

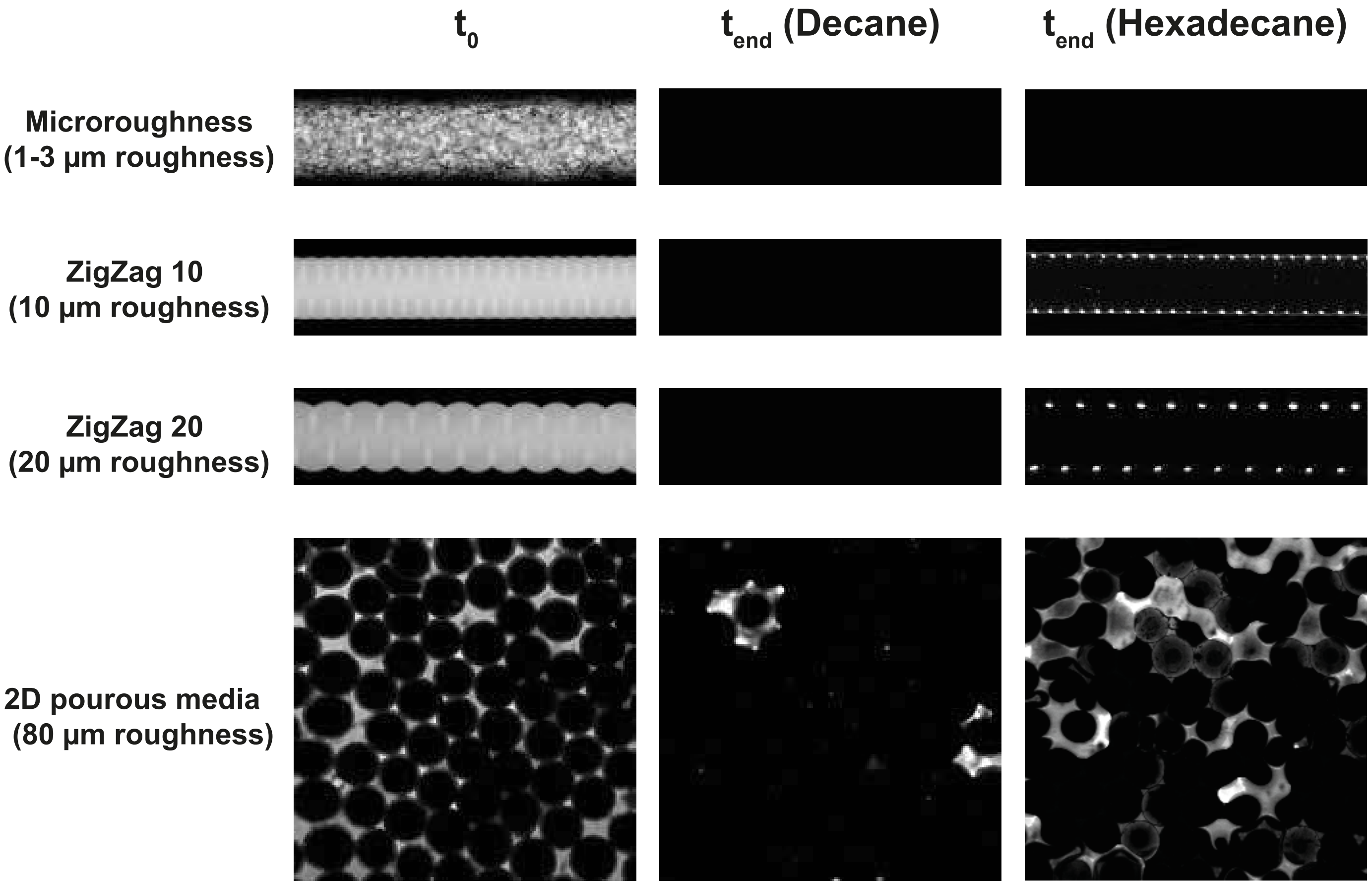

FIGURE 6.5: **Water flooding experiments.** Fluorescent imaging reveals significant differences (flooding flowrate = 250 $\mathrm{nlmin^{-1}}$) between the trapping behaviour of oils with different viscosities in various microchannels with different roughness feature sizes. The inviscid decane (η = 0.92 mPas) was (almost) completely displaced by the water phase for all tested experimental conditions. In contrast, considerable amounts of the more viscous hexadecane (η = 3.47 mPas) remained trapped in roughness features of at least 10 µm size.

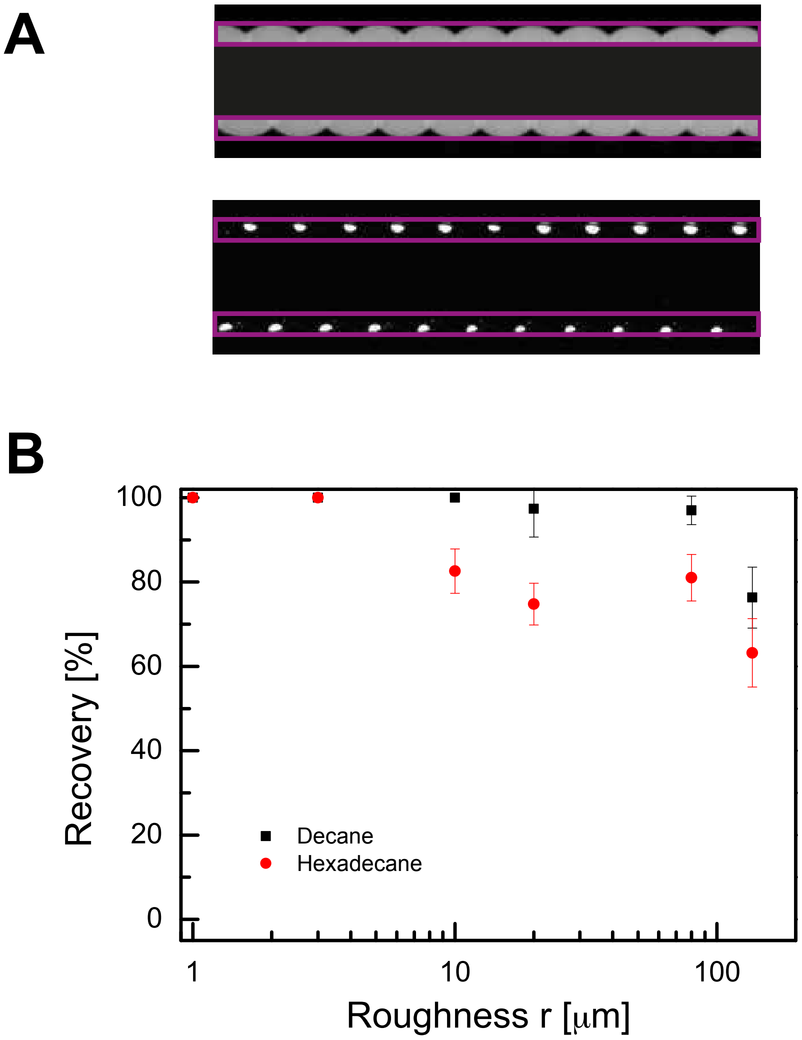

Figure 6.6: **Oil recovery and roughness size.** A: Derivation of the oil recovery rate for 'zigzag' channels B: The fraction of recovered oil was found to depend on both viscosity and roughness size. The inviscid decane (η = 0.92 mPas) was (almost) entirely recovered for roughnesses $\leq$ 80 µm, while increasing amounts of the viscous hexadecane (η = 3.47 mPas) were entrapped with increasing roughness feature sizes. The designated error bars represent the standard deviation of calculated oil recovery rates from five independent experimental runs per data point.

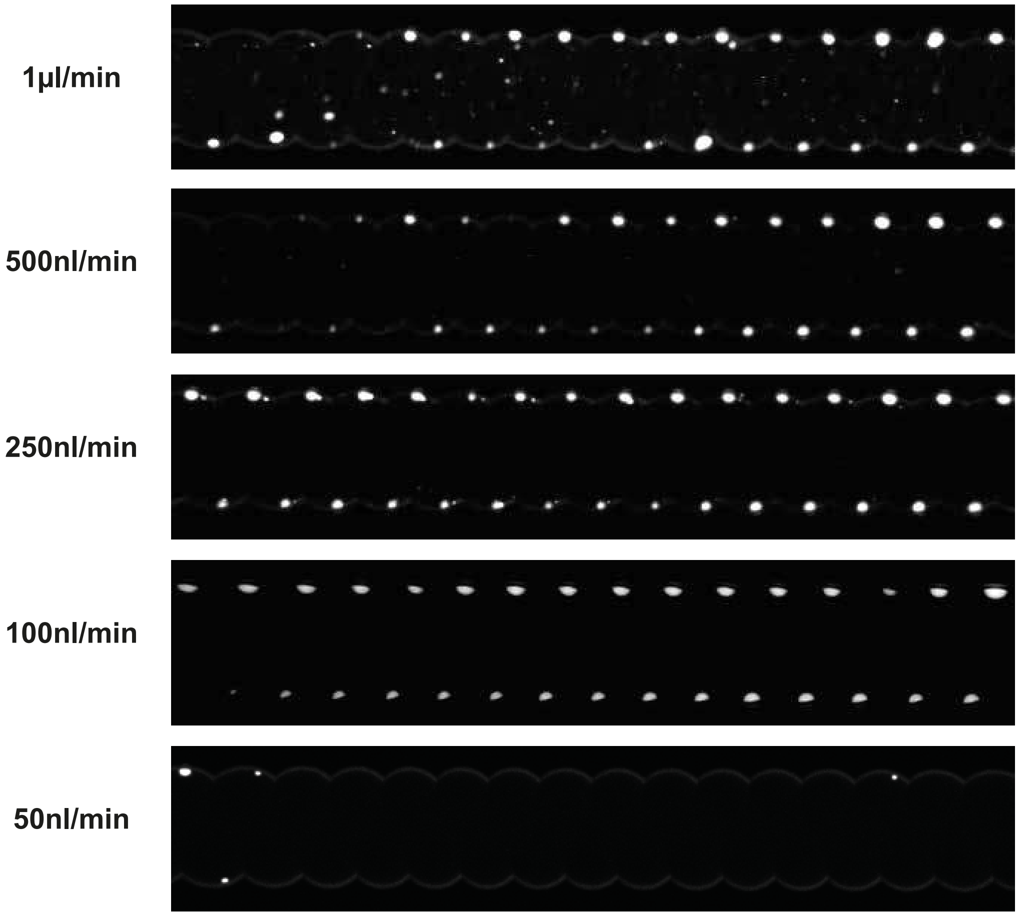

FIGURE 6.7: **Flowrate dependence of oil trapping.** The average size of the trapped oil droplet increases with increasing water flooding flowrate for hexadecane and roughness features sizes of at least 10 µm (here: hexadexane in 'ZigZag 20' channel)

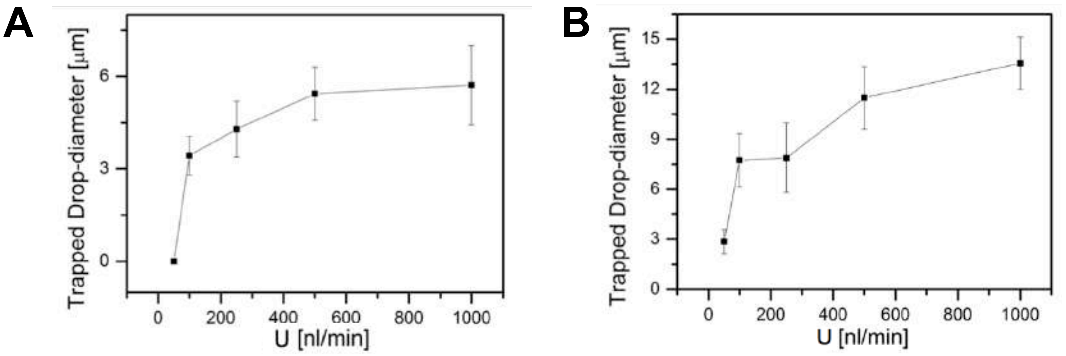

FIGURE 6.8: **Flowrate dependence of trapped oil droplets.** The average diameter d of the trapped oil droplets increases with increasing water flooding flowrate U as $d \propto U^{1/3} (\propto Ca^{1/3})$ A: 10 µm roughness ('ZigZag 10' channel) B: 20 µm roughness ('ZigZag 20' channel).

6.3.3 Towards a generic scaling law incorporating capillarity and roughness effects

So far we have demonstrated that both the surface roughness and the capillary number have an ample impact on the relative displacement behaviour of water and oil in a rough microfluidic device. Clearly, the reconciliation of both arguments within a single generic scaling law, that consequently accounts for all the observed effects, would be a desirable next step to take. We therefore extended Bretherton's model (eq. 6.1) by integrating the size of the characteristic roughness r as a normalization parameter for the quantity of retained oil measured as the image area A that is occupied by the fluorescently labelled oil :

$$\frac{A_{trapped\ oil}}{r^2} \propto Ca^{\frac{2}{3}} \tag{6.2}$$

If this relation holds, the entrapped oil quantities from different microfluidic channels should be collapsible onto a universal 'master' curve. We subsequently normalized our hexadecane data from all microdevices and were indeed able to converge them onto a single curve without having to change the index of the power law exponent as suggested by eq. 6.2 (Fig. 6.9) (n.b.: in the case of the 2D porous media experimental constraints only allowed to test higher flowrates).

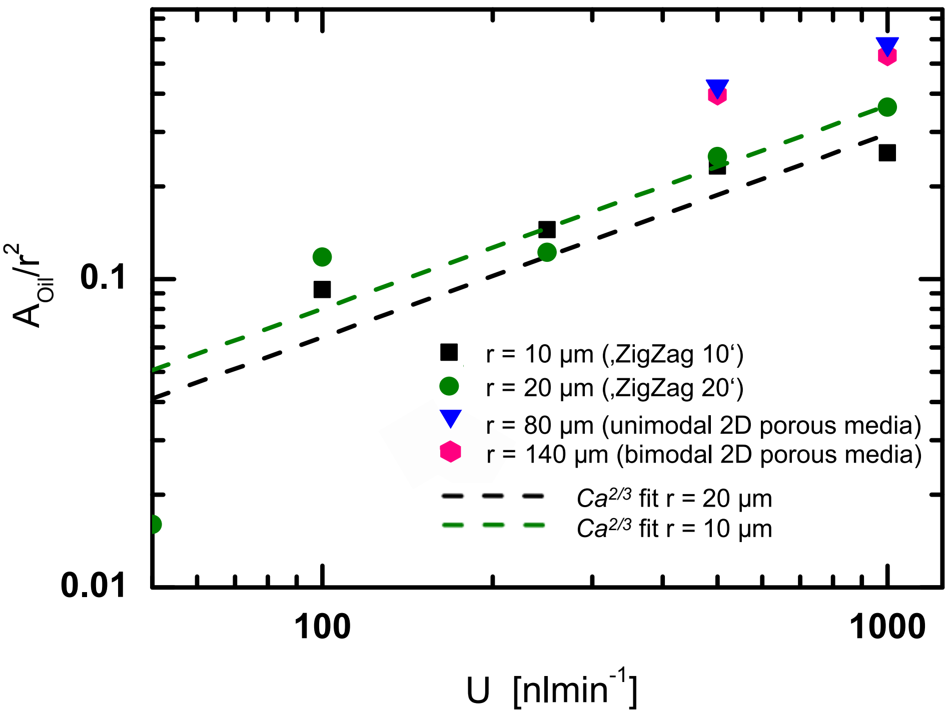

FIGURE 6.9: **Collapse of experimental oil recovery data through universal scaling law.** Normalization of the area A occupied by trapped oil with the a corresponding characteristic roughness size r^2 allows to collapse the data from different experiments onto a single curve following a $A/r^2 \propto Ca^{2/3}$ scaling.

6.3.4 Oil-water displacement patterns in complex porous networks

Our results so far allowed us to conceive a generic scaling law for predicting the amount of retained oil based on the surface tension and the viscosity of the displaced oil in combination with the roughness of the microdevice. Besides the overall recovery, another interesting question that arises in this context is the actual displacement path: the latter can considerably vary with both the surface topology and the physical properties of the displaced fluid. In the case of a single 'straight pore' channel (*here:* the microroughness and 'ZigZag' channels) only one possible displacement path exists, while in the case of a 2D porous media a large number of alternatives can be thought of. For this analysis, we consequently considered a larger microscopic field of view and compared the relative displacement patterns found for decane versus hexadecane in either a unimodal or a bimodal channel. Fig. 6.10 shows the corresponding fluorescent images of the final states after waterflooding at various network locations, whereby x denotes the distance from the inlet of the microdevice.

We have already stated earlier that decane recovery is superior to hexadecane recovery in any of the tested microdevices. Within the 2D porous networks, waterflooding occurs on the same time scale, i.e. the time t that the invading fluid (water) takes to reach a certain location within the network is approximately the same for each of the tested conditions. In such a case the applicability of Washburn's equation of capillary/pore-invasion can be considered, which relates the area L^2 of displaced fluid to the pore diameter D of the porous media and the viscosity η of the displaced fluid itself:

$$L^2 \approx \frac{D}{\eta} \tag{6.3}$$

According to this equation the amount of displaced oil (measured through the area L^2) should be about four times higher for decane versus hexadecane for a constant pore size D. The actually observed difference is, however, a lot smaller, i.e. $\sim$ 98 % versus $\sim$ 80 % in unimodal porous networks (Fig. 6.5) and $\sim$ 80 % versus $\sim$ 65 % in bimodal porous networks (Fig. 6.10A and C) for decane and hexadecane respectively.

This discrepancy from the theoretical prediction can be explained by fundamental differences in the displacement mechanisms as derivable from Fig. 6.10A and C. In the case of multiple pore sizes, decane displacement occurs mainly through the smaller pores, while the majority of residual oil remains trapped in the bigger pores. In contrast to that, hexadecane tends to preferentially displace from the big pores leaving the majority of residual oil trapped in the small pores. The latter is consistent with eq. 6.3, that predicts that within the same porous medium the relative amount of displaced fluid should be higher for bigger pores. Altogether though, our experimental observations suggest that the actual displacement pattern of water and oil is more complex than grasped by Washburn's equation.

The relatively small viscosity of decane apparently facilitates its 'access' into the small pores from which it can readily be displaced by the invading water, which has a very similar viscosity. In this context one might also wonder whether the presence of a bimodal pore distribution is a prerequisite for decane trapping in general or whether the latter is linked to a certain roughness 'threshold' size. While this certainly exceeds the scope of the present work, it would be a worthwhile quest to be addressed in future studies on a wider variety of porous media.

In the case of hexadecane, the high viscosity gives rise to complex fluid effects that constrain hexadecane penetration into the smaller pores. Hexadecane displacement occurs therefore primarily along the big pores that constitute the 'easiest way out' of the porous network. The associated viscous fingering dynamics have been extensively studied in the past [23, 24, 25] and emerge in general when a viscous phase (*here*: hexadecane) is being pushed by a less viscous fluid (*here*: water). This causes an instability of the interface between the two fluid phases which hence no longer constitutes a smooth boundary, but adopts a finger-like shape instead. The width of these 'fingers' is usually determined by the competition of capillary and viscous forces. In addition, for Reynolds numbers larger than unity ($Re >> 1$), inertia can also become relevant as demonstrated by Chevalier and co-workers [26]. In our experiments $Re \sim 100$ and therefore inertial effects might equally add to the complexity of the observed fluid displacement patterns.

That being said, these observations hold only true with an important caveat regarding the uniformity of the bimodal porous media: the fabrication protocol does not yet allow for the precise control of the number and location of the bigger pores and therefore certain properties of an individual device might deviate to a considerable extent from the average value. Consequently, the comparability of individual experiments is only given within the scope of this intrinsic fabrication error.

Taken together, our experiments in unimodal and bimodal 2D porous networks allowed us not only to study the effect of roughness on the relative microdisplacement of water and oil in a structure reminiscent of oil reservoir pores, but also to visualize the preferred displacement paths of decane versus hexadecane which are in line with previous studies on complex fluid/ viscous fingering effects. However, for a more detailed and systematic examination of the various factors involved, a more rigid fabrication protocol has to be conceived in order to minimize uncertainty regarding the experimental error, which will be subject to future investigations.

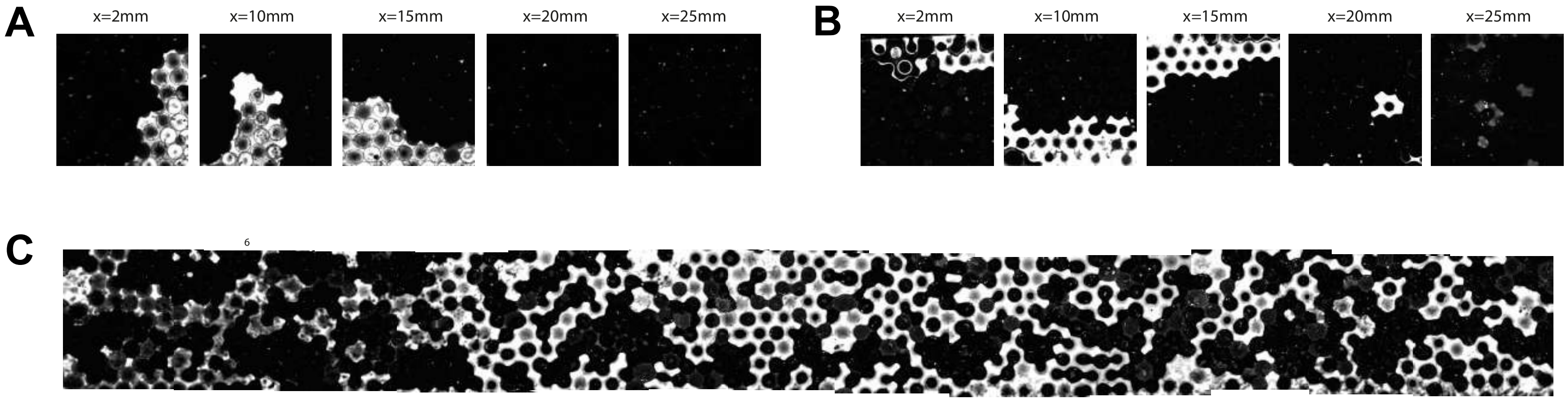

FIGURE 6.10: **Oil-water displacement dynamics in 2D porous media (PM).** Fluorescent images of stable end state (t_{end}) after water flooding at various locations from the injection inlet. A: Decane in bimodal PM. B: Hexadecane in unimodal PM. C: Hexadecane in bimodal PM (stitched image). In a bimodal PM, the inviscid decane stays preferentially trapped in the big pores (A). The viscous hexadecane, in contrast, is exclusively retained in the smaller pores with a lower overall oil recovery (C).

6.4 Conclusion

We have studied oil-water microdisplacements in different microfluidic devices that dispose of roughness features between 1 and 140 µm. Our experiments revealed both roughness and viscosity as key determinants of the wetting behaviour of the involved fluids. Oil entrapment was found to increase with increasing roughness size and increasing oil viscosity. These results are crucial to current porous media and oil recovery research, where fluid entrapment is still primarily attributed to capillarity whilst omitting the role of surface topology. Based on our findings we were able to formulate a generic scaling law to estimate the amount of retained oil based on the joint effects of roughness, viscosity, surface tension and fluid velocity. In the case of porous media, the interplay of pore size (distribution) and viscosity gives rise to more complex displacement patterns involving fingering effects for higher viscosity oils.

Bibliography

[1] M. J. Blunt. Flow in porous media pore-network models and multiphase flow. *Current Opinion in Colloid & Interface Science*, 6(3):197–207, 2001.

[2] M. J. Blunt and H. Scher. Pore-level modeling of wetting. *Physical Review E*, 52(6):6387–6403, 1995.

[3] S. Thomas. Enhanced Oil Recovery - An Overview. *Oil & Gas Science and Technology - Rev. IFP*, 63(1):9–19, 2008.

[4] L.W. Lake. *Enhanced oil recovery*. Society of Petroleum Engineers, 2010.

[5] M. J. Rosen, H. Wang, P. Shen, and Y. Zhu. Ultralow Interfacial Tension for Enhanced Oil Recovery at Very Low Surfactant Concentrations. *Langmuir*, 21(9):3749–3756, 2005.

[6] A. Z. Abidin, T. Puspasari, and W. A. Nugroho. Polymers for Enhanced Oil Recovery Technology. *Procedia Chemistry*, 4:11–16, 2012.

[7] S. Thomas and S. M. Farouq Ali. Status and Assessment of Chemical Oil Recovery Methods. *Energy Sources*, 21(1-2):177–189, 1999.

[8] A. R. Kovscek and M. D. Cakici. Geologic storage of carbon dioxide and enhanced oil recovery. II. Cooptimization of storage and recovery. *Energy Conversion and Management*, 46(11-12):1941–1956, 2005.

[9] D. W. Green and G. P. Willhite. *Enhanced Oil Recovery*. SPE textbook series. Henry L. Doherty Memorial Fund of AIME, Society of Petroleum Engineers, 1998.

[10] D. Bonn, J. Eggers, J. Indekeu, J. Meunier, and E. Rolley. Wetting and spreading. *Reviews of Modern Physics*, 81(2):739–805, 2009.

[11] D. Bonn and D. Ross. Wetting transitions. *Reports on Progress in Physics*, 64(9):1085, 2001.

[12] P. G. de Gennes, F. Brochard-Wyart, and D. Quéré. *Capillarity and Wetting Phenomena: Drops, Bubbles, Pearls, Waves*. Springer New York, 2003.

[13] F. Nono, H. Bertin, and G. Hamon. An Experimental Investigation of the oil Recovery in the Transition Zone of Carbonate Reservoirs Taking Into Account Wettability Change. *Proceedings of International Petroleum Technology Conference*, Doha, Qatar:20–22 January, 2014.

[14] F. Nono, H. Bertin, and G. Hamon. Oil recovery in the transition zone of carbonate reservoirs with wettability change: hysteresis effects of relative permeability versus experimental data. *Proceedings of International Symposium of the Society of Core Analysts*, Avignon, France:8–11 September, 2014.

[15] Z. Deng, Y. Chen, and C. Shao. Gas flow through rough microchannels in the transition flow regime. *Physical Review E*, 93(1):013128, 2016.

[16] B.-Y. Cao, M. Chen, and Z.-Y. Guo. Rarefied Gas Flow in Rough Microchannels by Molecular Dynamics Simulation. *Chinese Physics Letters*, 21(9):1777, 2004.

[17] O. I. Rovenskaya and G. Croce. Numerical simulation of gas flow in rough microchannels: hybrid kinetic continuum approach versus Navier Stokes. *Microfluidics and Nanofluidics*, 20(5):81, 2016.

[18] S. Shen, J. L. Xu, J. J. Zhou, and Y. Chen. Flow and heat transfer in microchannels with rough wall surface. *Energy Conversion and Management*, 47(11-12):1311–1325, 2006.

[19] D. Y. Yang. Numerical Analysis of Micro-Mixing in Rough Microchannels. In *Manufacturing Process Technology*, volume 189 of *Advanced Materials Research*, pages 1452–1455. Trans Tech Publications, 4 2011.

[20] C. Kunert and J. Harting. Simulation of fluid flow in hydrophobic rough microchannels. *International Journal of Computational Fluid Dynamics*, 22(7):475–480, 2008.

[21] A. Huerre, O. Theodoly, A. M. Leshansky, M.-P. Valignat, I. Cantat, and M.-C. Jullien. Droplets in Microchannels: Dynamical Properties of the Lubrication Film. *Phys. Rev. Lett.*, 115:064501, 2015.

[22] J. Seiwert, C. Clanet, and D. Qu´ eré. Coating of a textured solid. *J. Fluid Mech.*, 669:55–63, 2011.

[23] P. G. Saffman and G. Taylor. The Penetration of a Fluid into a Porous Medium or Hele-Shaw Cell Containing a More Viscous Liquid. *Proceedings of the Royal Society of London A: Mathematical, Physical and Engineering Sciences*, 245(1242):312–329, 1958.

[24] D. Bensimon, L. P. Kadanoff, S. Liang, B. I. Shraiman, and C. Tang. Viscous flows in two dimensions. *Rev. Mod. Phys.*, 58:977–999, Oct 1986.

[25] Y. Couder. *Growth patterns: From stable curved fronts to fractal structures (A summary)*, pages 85–88. Springer US, Boston, MA, 1995.

[26] C. Chevalier, M. Ben Amar, D. Bonn, and A. Lindner. Inertial effects on Saffman-Taylor viscous fingering. *Journal of Fluid Mechanics*, 552:83–97, 2006.

[27] N.S.K. Gunda, B. Bera, N. K. Karadimitriou, S. K. Mitra, and S. M. Hassanizadeh. Reservoir-on-a-Chip (ROC): A new paradigm in reservoir engineering. *Lab on a Chip*, 11(22):3785–3792, 2011.

[28] N. Sefrioui, A. Ahmadi, A. Omari, and H. Bertin. Numerical simulation of retention and release of colloids in porous media at the pore scale. *Colloids and Surfaces A: Physicochemical and Engineering Aspects*, 427:33–40, 2013.

Acknowledgements

The whole is greater than the sum of its parts...
Aristotle

Pursuing a 'Doctor of Philosophy' is definitely more than just performing research, publishing papers and writing up these parts to obtain a doctoral thesis as 'end product': most graduates - me included - probably view it more as a 'school of life' in general. I am therefore very grateful for all the enriching experiences that I could make besides my actual scientific work in two 'foreign' countries that quite a few times turned out to differ more from one another than I would have expected. During these past 3.5 years I was also lucky to meet a wide variety of interesting, diverse and inspiring people both at work and beyond, that altogether helped me shaping my endeavours for the future.

On these grounds, I would first of all like to express my deep gratitude to my two supervisors Daniel Bonn and Michael Tatoulian to have given me the opportunity to work in their research facilities in Paris and Amsterdam respectively whilst guiding me all the way along to the day of my defense with both enthusiastic encouragements and useful critical thoughts.

Besides my two supervisors, I would equally like to thank the rest of my thesis committee members for widening my research horizon through their respective perspectives and additional comments. At this point I would like to express my sincere thanks to Sander Woutersen and Gertien Smits for always making time for inspiring, encouraging and thought provoking discussions. My particular thanks also goes to Hamid Kellay who provided me an opportunity to work on droplet pinch-off dynamics in his laboratory facilities in Bordeaux together with his (former) PhD student Antoine Deblais which whom I was able to discover one of the most striking findings of my present thesis.

I started my PhD in October 2013 working in Michael's research group '2pm' (procédés, plasmas et microsystèmes) and was very warmly welcomed by all

group members right from the start. I would like to thank everyone from that group, especially Stéphanie, Mengxue, Alexandre, Olivier, Magda, Bradley, Guillaume, Cédric and Fred, for supporting me whenever needed. Special thanks also goes to a number of people working outside of '2pm' that significantly helped me putting forward my Parisian research projects, especially Nadia Touati (ENSCP), Laurent Binet (ENSCP), Aline Percot (UPMC) and Davide Ferraro (Institut Curie). Many experiments would not have been possible without the support from technical staff at both ENSCP and ESPCI, so I am also very grateful for that. At this point, I would also like to thank the entire administrative staff from both ENSCP and UPMC, especially Nathalie Ouvry, for helping me tackle the fairly complex administrative part of my 'cotutelle de these'.

From the end of my first year onwards, I started my experimental work at the University of Amsterdam and again received a lot of support from all my colleagues: Maureen, Henri, Bart, Tom, Dominik, Moshin, Simon, Sanne, Joep, Emmanuel, Stephan, Laura. Special thanks goes to Bijoy, Thijs, Antoine and Martijn with whom I worked together a lot on numerous experiments and had very fruitful discussions about the interpretation of our results. I would also like to extend my thanks to the people from the electronics department of the UvA for having helped me realizing multiple experimental challenges. Special thanks goes to Gerrit Hardemann who fixed one of my most important microscopy PCs and Tijs van der Roon who helped me a lot with assembling the electrical setup presented in chapter 5 and who ran some very valuable MATLAB simulations on the electrical mercury pinch-off for me. Lastly, I would also like to express my sincere thanks to the administrative staff at the UvA, especially Rita, Anne-Marieke and Nathalie for patiently helping me meeting all the administrative Joint PhD requirements and with finding multiple accommodations on the tight housing market in Amsterdam.

Beyond these academic settings I was very lucky to have been accompanied by several very good friends that I could always count on even in the more difficult and stressful phases and which helped me a lot in shaping my future paths. Last, but decidedly not least, I would like to thank my parents and my brother for both their unconditional support and indefatigable encouragements throughout my thesis. Ohne euch wäre dies alles nicht möglich gewesen - merci beaucoup!

Appendix A

Simulation of mercury pinch-off MATLAB code

```
% Constants
phi = 18;
rho_r = 961e-9; % ohm.meter, mercury electical conductivity, verified
sigma = 485.5e-3; % kg.s^2, mercury surface tension @ 20 degrees C, verified
rho = 13.534e3; % kg/m^3, mercury density , changed
A = 0.9; % 1/m^-1/3, prefactor
Fc = 1000E6;  % cut-off frequency
Fs = 10*1E9; % Samplerate: 10 Gsps
Vin = 1.04; % Actual starting voltage way before pinch-off (NOT the voltage at
    the first sample)
time_shift = 0; % 33e-9; %0.75E-10;  % T-pinchoff minus Scope t_trigger
model_shift = 33e-9; % shift model relative to scope signal
cut_shift = 0.2e-9; % -32.8e-9;

% Derived constant values
Rk = 2*cot(phi*(2*pi/360))*rho_r/pi;  % resistance constant, R = Rk/d

% Scope Waveform data
wfm = load('/users/ineshauner/desktop/PO_Hg/curves/1␣Volt/1ms_10032_points/
    RefCurve_2016-03-29_21_164940.wfm.csv');
wfm = wfm ./ Vin;
XStart = -7.515e-7;            % start at -750 ns
XStop  =  2.517e-7;            % Stop at 250 ns
SignalResolution = 1e-10;      % 10 GSmps
SignalHardwareRecordLength = (XStop - XStart)/SignalResolution;

% Generate time axis
time = linspace(XStart-time_shift, XStop-time_shift, 10032);
tau = ((time-model_shift) < 0) .* (time-model_shift) * -1;  % time remaining
    until pinchoff
hold off;
plot(time, wfm)
hold on;
```

```
% Generate model
d = A*power((sigma*power(tau,2)/rho), 1/3);
plot(time, d .* 1e6);
R = Rk ./ d;
Vmodel = 50 ./ (R+50); % normalized;
plot(time, Vmodel);

% Generate cut model
d_cut = ((time - cut_shift) < 0) .* d;
R_cut = Rk ./ d_cut;
Vmodel_cut = 50 ./ (R_cut+50); % normalized
plot(time, Vmodel_cut);

% Filter this cut model
[b, a] = butter(3, Fc/(Fs/2)); % 3rd order butterworth
Vmodel_filt = filter(b, a, Vmodel_cut);
plot(time, Vmodel_filt);

% Generate current density for this model
I = Vin ./ (50+R);
Area = pi*power(d_cut/2, 2);
Id = I ./ Area;
plot(time, Id*1e-12);
[max_Id, max_Id_idx] = max(Id .* (Id < Inf));
max_Id
max_Id_diam = d(max_Id_idx)
Id_to_diam_ratio = max_Id / max_Id_diam

% Add a legend to the graph
axis([-7e-7 2e-7 -0.5 2.0])
axis([-20e-8 1e-9 -0.5 2.0])
legend( 'measured␣[norm]', 'diam␣[um]', 'model␣[norm]', 'model␣cut␣[norm]', '
    model␣cut,␣1␣GHz␣[norm]', 'Id␣[A/um2]')
xlabel('time␣[s]')
ylabel('units')

% Save variables
time = time';
d = d';
d_cut = d_cut';
Area = Area';
Vmodel = Vmodel';
Vmodel_cut = Vmodel_cut';
Vmodel_filt = Vmodel_filt';
R = R';
R_cut = R_cut';
I = I';
Id = Id';

T = table(time, wfm, d, d_cut, Area, Vmodel, Vmodel_cut, Vmodel_filt, R, R_cut,
    I, Id);
writetable(T, 'PinchOff1v_table.csv', 'Delimiter','␣')
```